COMPUTATIONAL STUDIES OF THE MECHANISMS AND DYNAMICS OF CHEMICAL REACTIONS

By

KOMAL YADAV

CHEM11201704028
National Institute of Science Education and Research Bhubaneshwar

A thesis submitted to the
Board of Studies in Chemical Sciences
in partial fulfillment of requirements for the degree of
DOCTOR OF PHILOSOPHY
of

HOMI BHABHA NATIONAL INSTITUTE

JUNE 2022

Homi Bhabha National Institute

Recommendations of the Viva Voce Committee

As members of the Viva Voce Committee, we certify that we have read the dissertation prepared by **Komal Yadav** entitled **"Computational Studies of the Mechanisms and Dynamics of Chemical Reactions"** and recommend that it may be accepted as fulfilling the thesis requirement for the award of Degree of Doctor of Philosophy.

Chairman - Prof. A. Srinivasan — Date: 29.09.2022

Guide / Convener - Dr. U. Lourderaj — Date: 29.09.2022

Co-Guide - — Date:

Examiner - Prof. Sai G. Ramesh, IISc Bangalore — Date: 29.09.2022

Member 1 - Dr. B. L. Bhargava — Bhargava B.L. Date: 29.09.2022

Member 2 - Dr. Arindam Ghosh — Date: 29.09.2022

Member 3 - Dr. Snehasis Chowdhuri, IIT Bhubaneswar — Date: 29.09.2022

Final approval and acceptance of this thesis is contingent upon the candidate's submission of the final copies of the thesis to HBNI.

We hereby certify that we have read this thesis prepared under my/our direction and recommend that it may be accepted as fulfilling the thesis requirement.

Date: 29.09.2022.

Place: Bhubaneswar

(Co-Guide)

Dr. U. Lourderaj

(Guide)

STATEMENT BY AUTHOR

This dissertation has been submitted in partial fulfillment of requirements for an advanced degree at Homi Bhabha National Institute (HBNI) and is deposited in the Library to be made available to borrowers under rules of the HBNI.

Brief quotations from this dissertation are allowable without special permission, provided that accurate acknowledgement of source is made. Requests for permission for extended quotation from or reproduction of this manuscript in whole or in part may be granted by the Competent Authority of HBNI when in his or her judgment the proposed use of the material is in the interests of scholarship. In all other instances, however, permission must be obtained from the author.

[redacted]

Signature of the Student
Komal Yadav

DECLARATION

I, hereby declare that the investigation presented in the thesis has been carried out by me. The work is original and has not been submitted earlier as a whole or in part for a degree / diploma at this or any other Institution / University.

[redacted]

Signature of the Student
Komal Yadav

LIST OF PUBLICATIONS ARISING FROM THE THESIS

Journal

1. Raghunathan, S.†; Yadav, K.†; Rojisha, V. C.; Jaganade, T.; Prathyusha, V.; Bikkina, S.; Lourderaj, U.; Priyakumar, U. D. Transition between [*R*]- and [*S*]-stereoisomers without bond breaking. *Phys. Chem. Chem. Phys.*, **2020**, *22*, 14983 (†equal contribution).
2. Yadav, K.; Lourderaj, U.; Priyakumar, U. D. Stereomutation in tetracoordinate centers via stabilization of planar tetracoordinated systems. *Atoms*, **2021**, *9*, 79.
3. Yadav, K.; Pradhan, R.; Lourderaj, U. Influence of second-order saddles on reaction mechanisms. *Faraday Discuss.*, **2022**.

Manuscripts under preparation

1. Yadav, K.; Lourderaj, U.; Priyakumar, U. D. Stereomutation in tetrahedral tetracoordinated systems.
2. Yadav, K.; Lourderaj, U. Mechanisms and dynamics of the thermal deazetization of 2,3-diazabicyclo[2.2.1]hept-2-ene.

[redacted]

Signature of the Student
Komal Yadav

CONFERENCES AND WORKSHOPS ATTENDED

1. Introduction to Gaussian 16: Theory and Practice, Kolkata **2019**.
2. DAE Computational Chemistry Symposium, BARC, Mumbai, **2019**.
3. Spectroscopy and Dynamics of Molecules and Clusters, BITS Pilani, Pilani campus, and IIT Jodhpur, Rajasthan, **2020**.
4. Theoretical Chemistry Symposium, IISER Kolkata, **2021** (online).
5. Sakura Science Workshop at Ibaraki University, Mito, Japan, **2021** (online).

[redacted]

Signature of the Student
Komal Yadav

ACKNOWLEDGEMENT

I would like to express my sincere gratitude to my PhD supervisor Dr. Upakarasamy Lourderaj, for his continuous support throughout my PhD work. He has always been very helpful, supportive, and understanding during these years. He is always available for his students not only for academics, but also as a friend and advisor, whenever they are in need. I would like to thank him and ma'am, Mrs Nisha Lourderaj for the homely environment they have provided me during this time. Special thanks to Dr. U. Deva Priyakumar for collaborating with us in different projects, introducing me to the exciting topic of planar tetracoordinate carbon systems, and providing me different opportunities to excel.

I would like to thank the members of my thesis monitoring committee Dr. A. Srinivasan, Dr. Arindam Ghosh, Dr. B. L. Bhargava, and Dr. Snehasis Chowdhuri for their constant support and suggestions in my PhD work. Special thanks to DAE and NISER for financial and academic support. I would also thank Dr. Manikandan Paranjothy and Dr. P. C. Ravikumar for collaborating with us in the exciting field of second-order saddle dynamics and organometallic reactions. Thanks to my collaborators Dr. Shampa Raghunathan, Dr. Renuka Pradhan, and Richa Rashmi for working with me in different projects and always being up for discussions. I would thank Dr. Kousik Giri for introducing me to the field of computational chemistry and always being there for me. Thanks to A. Ananda Raman for helping me with the HPC.

This journey would have not been possible without the support of my family and friends. Words are not enough to explain my gratitude for my mother Sunita Yadav, grandmother Suma Devi, and grandfather Late Shankar Prasad Yadav and I will always be grateful to them. Good friends are truly a gem, and I could not ask more from Pradeep, Kautilya, and Vishal. Thank you guys for always being there and motivating me in all the difficult times. Thanks to Anwesha, Preeyanka, Kiran, and Sumela for all the support and fun and making my PhD journey memorable. I would also like to thank Dr. Jayanth and Dr. Nishant for being the supportive seniors cum friend. Thanks to Dr. Pankaj, and Soumya for helping me with the corrections in thesis, and my labmates Siddharth, Dipanshu, Aniruddha, Tanaya, Uday, Anshika, Swati, Rupayan, Shrishti, Rudra, Jishnu, Abhishek for all the fun we had.

ABSTRACT

Understanding the atomic-level mechanisms can help us control chemical reactions and hence the product selectivity. However, the experimentally measured rate constant often fails to capture the atomic-level mechanisms followed during a chemical reaction. In this context, various state-of-the-art experiments as well as computational studies have been designed to understand the mechanisms of chemical reactions. Computationally, the atomic-level mechanisms followed in chemical reactions are investigated by mapping the potential energy profile for the reactions that describe the variation of potential energy of a system along the reaction coordinate. However, the progress of chemical reactions is accurately described by the dynamics of the system. Hence, it is of fundamental interest to study the time evolution of the system to understand the detailed mechanisms, in particular when the dynamical effects are important. In the present thesis, we investigate the atomic-level mechanisms of certain chemical reactions by mapping their potential energy profiles using *ab initio* and density functional theoretical (DFT) methods and by studying the dynamics of the systems using *ab initio* classical trajectory simulations, where the necessary are computed on-the-fly at a specific level of theory.

In chapter 1, a brief introduction of various quantum mechanical methodologies and *ab initio* classical dynamics simulation techniques used to study the reaction mechanisms is discussed.

Chapter 2 deals with stereomutation in tetracoordinated centers via stabilization of planar tetracoordinated systems. The stabilization of planar forms of tetracoordinate carbon is an active area of research from a fundamental point of view. However, the presence of a lone pair of electrons on the central carbon atom and electron-deficient bonds inhibits the stabilization of the planar tetracoordinated center (**ptc**). Thus, the stabilization of the **ptc** can be achieved by (i) removal of the lone pair of electrons on the central atom, (ii) addition of σ-donor or π-acceptor substituents, and (iii) addition of small rings to the system. In the present study, we have proposed different model systems to stabilize the **ptc**, where the central carbon atom is replaced by valence isoelectronic atoms from group 13, 14, and 15. We also found that, in some of the proposed systems, possible isomerization between two tetrahedral isomers can be achieved via a **ptc** and vice-versa.

In Chapter 3, we investigated model systems where the transition between [*R*]- and [*S*]- stereoisomers without bond breaking is possible. Traditionally, the transition between two enantiomers (*R* and *S*) is possible via a bond breaking pathway e.g., the S_N2 reaction. In contrast, the transition between the enantiomers via a planar structure involves a high energy barrier and hence this pathway is generally not considered. Here, using *ab initio* methods, we have designed model systems [XC_4H_4], (the central atom X was substituted with various valence isoelectronic species from group 13, 14, and 15) where the planar structure acts as a transition state or a stable intermediate for the interconversion between two tetrahedral isomers. The barriers for interconversion between two tetrahedral isomers for these systems were found to be $\leq$ 5 kcal mol^{-1}. In addition, the ring opening pathways for the isomerization were also mapped using *ab initio* methods. We have also proposed a chiral model system [$SiCH_2C(CH_3)_2BN$], where the barriers for transition between *R*- and *S*-isomers were found to be lower than via the bond breaking pathways. *Ab initio* classical dynamics simulations performed on these systems reveal that the isomerization between two tetrahedral isomers occurs via a planar structure.

In Chapter 4, the influence of second-order saddles on reaction mechanisms is investigated. The thermal denitrogenation of 1-pyrazolines has been studied both experimentally and theoretically due to their unusual stereochemical preference during the formation of the cyclopropane products with a major single inversion of configuration. Recent studies revealed that in the thermal denitrogenation of 1-pyrazoline, a fraction of trajectories accesses the higher energy second-order saddle (SOS), avoiding the traditional transition state during the reaction. In this study, we investigated the denitrogenation of 1-pyrazoline at higher available energies to the system to understand the influence of the second-order saddle on the reaction mechanisms. The dynamics of the system was found to be non-statistical. We also found that for halo-substituted 1-pyrazolines, the energy difference between the transition state and the SOS decreases, emphasizing the role of SOS in the reaction dynamics.

Chapter 5 reports the mechanisms and dynamics of the thermal deazetization of 2,3-diazabicyclo[2.2.1]hept-2-ene (**dbh**). Experimentally, the thermal denitrogenation of **dbh** shows an unusual preference for forming the bicyclopentane product with a major double inversion of configuration. In this context, computational studies carried out to understand the mechanism for the denitrogenation of **dbh** were found to be sensitive to the level of theory, and the energy profile for the asynchronous pathway could not be mapped completely. In the present study, we performed detailed quantum chemical calculations and *ab initio* classical dynamics simulations to investigate the mechanisms and dynamics of the denitrogenation of **dbh**. It was found that DFT methods were inadequate to describe the reaction pathways. Using multireference wavefunction methods, we successfully mapped the complete energy profile for the synchronous and the asynchronous pathways. The barriers for the synchronous and asynchronous denitrogenation pathways were similar ($\sim$ 37 kcal mol^{-1} at the CASSCF(4,4)/6-31+G* level) and indicate that the reaction can follow both the pathways. *Ab initio* classical dynamics simulations revealed the reaction followed both the synchronous and asynchronous pathways and resulted in the formation of the bicyclopentane with a major double inversion of configuration consistent with the experimental observation.

TABLE OF CONTENTS

Page

List of Figures **xi**

List of Tables **xvii**

1 Introduction **1**
- 1.1 Energetics 2
- 1.2 Dynamics 11
- 1.3 Rate Theories 13

2 Stereomutation in tetracoordinated centers via stabilization of ptx **17**
- 2.1 Introduction 17
- 2.2 Methodology 19
- 2.3 Results and Discussion 20
  - 2.3.1 Stabilization of **ptC** 20
  - 2.3.2 Stabilization of Planar Tetracoordinated Centers with Heteroatom (X) Substitution 23
  - 2.3.3 Stereomutation in Model Systems with Heteroatom Substitution . . . 29
- 2.4 Summary and Conclusions 31

3 Transition between [*R*]- and [*S*]- stereoisomers without bond breaking **33**
- 3.1 Introduction 33
- 3.2 Methodology 37
  - 3.2.1 Quantum Mechanical Calculations 37
  - 3.2.2 *Ab initio* Classical Trajectory Simulations 37
- 3.3 Results and Discussions 38
  - 3.3.1 Structure and Energetics 38
  - 3.3.2 Isomerization Reaction Pathways 40

3.3.3 Dynamics of the Isomerization 49
3.3.4 A Chiral System: $SiBNCH_2C(CH_3)_2$ 53
3.4 Summary and Conclusions 56

4 Influence of second-order saddles on reaction mechanisms 58
4.1 Introduction 58
4.2 Methodology 61
4.2.1 Stationary Points 61
4.2.2 Trajectories Initiated from the Reactant Region for 1-pyrazoline . . . 62
4.2.3 Trajectories Initiated from the SOS Region for 1-pyrazoline 63
4.2.4 Trajectories Initiated from the SOS Region for 3,3,5,5-tetrachloro-1-pyrazoline 63
4.3 Results and Discussions 64
4.3.1 Potential Energy Profile 64
4.3.2 *Ab initio* Classical Dynamics Simulations: 1-pyrazoline 70
4.3.3 *Ab initio* Classical Dynamics: 3,3,5,5-tetrachloro-1-pyrazoline 81
4.4 Summary and Conclusions 83

5 Mechanisms and Dynamics of the Thermal Denitrogenation of dbh 85
5.1 Introduction 85
5.2 Methodology 88
5.3 Results and Discussions 91
5.3.1 Potential Energy Profile 91
5.3.2 *Ab initio* Classical Dynamics Simulations 103
5.4 Summary and Conclusions 110

Bibliography 113

LIST OF FIGURES

FIGURE Page

1.1 Characterization of orbitals into inactive, active, and virtual spaces in a CASSCF calculation. 6

2.1 Walsh diagram of the valence occupied molecular orbitals for the transformation of tetrahedral to planar CH_4. The molecular orbitals are calculated at HF/STO-3G level of theory. 18
2.2 Two different skeleton models used in this study (i) three membered cyclic analogues, (ii) spiro[2,2]-type analogues. The central atom X is substituted with various valence isoelectronic species of carbon from group 13, 14, and 15. 20
2.3 (a) MO transformation on going from **ttC** to **ptC** for C_3H_4 and $[C_3H_4]^{2+}$, and (b) Atomic electron population obtained using natural population analysis. The MOs and the atomic populations are calculated at HF/cc-pVTZ level of theory. 22
2.4 Potential energy profile for stereomutation in XC_2H_4 analogues. The energies are reported in kcal mol^{-1}. 29
2.5 Potential energy profile for stereomutation in $[XC_2H_6]^{2+}$ analogues. The energies are reported in kcal mol^{-1}. 30
2.6 Potential energy profile for stereomutation in (a) $[XC_4H_4]$ analogues and (b) $[XC_4H_8]$ where X = Al^-. The energies are reported in kcal mol^{-1}. 30

3.1 Inversion of configuration at the chiral center during a S_N2 reaction. 34
3.2 Stereomutation via a planar structure. 35
3.3 Stereomutation via a pyramidal structure. 35
3.4 (a) Schematic representation of the **ttc** and **ptc** structures for the model systems used in this study, (b) Different valence isoelectronic elements used to replace the central spiro carbon atom in the model skeleton $X(C)_2(CH_2)_2$ 39
3.5 Schematic representation of various pathways for the interconversion between two tetrahedral isomers. 40

3.6 Potential energy profile for stereomutation of spiroconjugated compound for $X(C)_2(CH_2)_2$, where X = Al^-, Si, and P^+. 41
3.7 Potential energy profile for the ring-opening pathway of spiroconjugated compound $X(C)_2(CH_2)_2$, where X = Al^- and Si. 42
3.8 Potential energy profile for the ring-opening pathway of spiroconjugated compound $X(C)_2(CH_2)_2$, where X = P^+. 43
3.9 (a) Different stationary points obtained, (b) Schematic potential energy surface for $X(C)_2(CH_2)_2$, PES for X = (c) Si, (d) Al^-, and (e) P^+. The radial axis represents the variation of $\angle$XC1C2, θ and the polar axis represents the variation of the angle between the two planes formed by the two three-membered rings i.e. ϕ. A $10(\phi)\times 22(\theta)$ grid was used (for each quadrant) to make the scan surface. 44
3.10 Potential energy profile for stereoemutation of model $X(C)_2(CH_2)_2$ systems (X = Ga^-, Ge, and As^+). The relative energies and the imaginary frequencies are given in kcal mol^{-1} and cm^{-1} respectively. 46
3.11 Ring-opening pathway for the interconversion between **ttAs** and **ttAs′** via the planar intermediate, **int1**. The relative energies for different stationary points are given in kcal mol^{-1}. 47
3.12 (a) Ring-opening pathway for the interconversion between **ttAs** and **ttAs′**. The relative energies for different stationary points are given in kcal mol^{-1} and (b) PES scan obtained for X = As^+ by performing a relaxed scan as a function of ϕ and θ. 48
3.13 (a) Ring-opening pathway for the isomerization of **ttGe** to **ttGe′** and (b) potential energy surface scan for $[GeC_4H_4]$. The relative energies for different stationary points are given in kcal mol^{-1}. 48
3.14 (a) Ring-opening pathway for the isomerization of **ttGa** to **ttGa′** and (b) potential energy surface scan for $[GaC_4H_4]^-$. The relative energies for different stationary points are given in kcal mol^{-1}. 49
3.15 Representative trajectories showing stereomutation for systems with X = Al^-, Si, and P^+ respectively. The trajectories are plotted on the relaxed PES computed at MP2/cc-pVTZ level of theory. The radial axis represents $\angle$XC1C2 (θ) and the polar axis represents the variation of ϕ. The color coding represents the time evolution of the system. 51
3.16 Sample trajectories showing (a) stereomutation via **ptGe** and (b) ring-opening pathway for **ttAs**. The colorbar shows the evolution of the trajectory with time. . 52

3.17 Schematic representation of the tetrahedral tetracoordinated *R*, *S* and planar tetracoordinated *E* and *Z* isomers. 54

3.18 Potential energy profile for the *R*-*S* isomerization via clockwise and anti-clockwise rotation. 54

3.19 (a) Schematic representation of various pathways for the *R*-*S* isomerization, (b) Potential energy surface scan as a function of $\angle$SiNB versus ϕ. Sample trajectories showing *R*-*S* isomerization via (c) *E*-isomer and (d) *Z*-isomer. 55

4.1 Schematic diagrams of a PES showing (a) minima in two-directions, (b) maximum in one-direction, and (c) maxima in two-directions. 59

4.2 General representation of the molecular structures used in the present study. The atom numbers and important geometrical parameters are labelled. 64

4.3 (a) Potential energy profile for the synchronous denitrogenation of 1-pyrazoline and (b) PES obtained by performing a relaxed scan along the coordinates d_s and ϕ_s. The MEPs are plotted on the PES with solid black lines. The energies are obtained at the CASSCF(4,4)/6-31+G* level of theory and are reported in kcal mol^{-1}. 66

4.4 The asynchronous denitrogenation pathways for 1-pyrazoline at CASSCF(4,4)/6-31+G* level of theory via (a) planar like and (b) perpendicular like diazenyl diradicals. The **TS5** represents the transition state for a concerted denitrogenation pathway. This figure is adapted from Pradhan and Lourderaj, *Phys. Chem. Chem. Phys.*, **2017**, *19*, 27468-27477. 67

4.5 Potential energy profiles for the synchronous denitrogenation of 3,3,5,5-tetrachloro-1-pyrazoline mapped at the CASSCF(4,4)/6-31+G* level of theory. The energies are reported in kcal mol^{-1}. 69

4.6 Potential energy profiles for the synchronous denitrogenation of 3,3,5,5-tetrafluoro-1-pyrazoline mapped at the CASSCF(4,4)/6-31+G* level of theory. The energies are reported in kcal mol^{-1}. 69

4.7 Reactive trajectories following (a) synchronous, and (b) asynchronous denitrogenation pathways for E_{total} = 130, 140, and 150 kcal mol^{-1}. The trajectories are plotted on a relaxed PES scan of both the C-N bond distances (Å) calculated at the CASSCF(4,4)/6-31+G* level of theory. 71

4.8 Variation of ∠C5C4C3H8 and ∠C3C4C5H6 as a function of d_s showing (a) SI, (b) DI, and (c) Retention of configuration. The colorbar represents the electron density in the LUMO. The molecule is said to have a diradical character when the electron density in the LUMO is $>$ 0.45. The snapshots of the representative trajectories are shown below the plots. The two H-atoms are shown in different colors (yellow and green) to show the inversion/retention of configuration taking place during the product formation. 75
4.9 Trajectories traversing the SOS pathway for E_{total} = (a) 130, (b) 140, and (c) 150 kcal mol^{-1}. 76
4.10 Sample trajectories showing recrossing events via the **sos** for E_{total} = 150 kcal mol^{-1}. 77
4.11 Trajectories initiated from **sos** region following different reaction pathways during the thermal denitrogenation of 1-pyrazoline: (a) **py/py′**→ **sos** → **cyp**, (b) **py/py′** → **sos** → **tmd/tmd′**, and (c) **py′**→ **ts0** → **sos** → **cyp** (d) Representative trajectory showing the denitrogenation via the **sos** pathway. 78
4.12 Distribution of relative translational energy between the **cyp** and N_2 fragments for trajectories following synchronous, asynchronous, and SOS pathways for the three total energies. 80
4.13 PES obtained by performing a relaxed scan of ϕ_s and d_s at the CASSCF(4,4)/6-31+G* level of theory. The MEPs are plotted on the PES with solid black lines. . 81
4.14 Different mechanistic pathways followed by the trajectories initiated from **Cl_sos**. The trajectories are plotted on a relaxed PES scan of ϕ_s versus d_s of 3,3,5,5-tetrachloro-1-pyrazoline. 82

5.1 Different conformers of cyclopentane obtained due to the ring-puckering motion (a) envelope conformers (E_1 and ^1E isomer), (b) twisted conformers ($^3T_2$ and $^2T_3$ isomer). 88
5.2 Active orbitals used in the CASSCF calculations. The box indicates the orbitals used in the (4,4) active space. 89
5.3 Atom labels and important geometrical parameters of **dbh** used in further analysis. 91
5.4 Potential energy profile for the synchronous denitrogenation of **dbh** at the CASSCF(4,4)/6-31+G* level of theory 94
5.5 Potential energy profile for the formation of **bcp_di** and **bcp_ret** from **cpdr** mapped at the CASSCF(4,4)/6-31+G* level of theory. The energies are reported with respect to **dbh**. 95
5.6 IRC plot connecting **dbh** and **int2a** via transition state **ts1a**. 95

5.7 Potential energy profile for the asynchronous denitrogenation of **dbh** at the CASSCF(4,4)/6-31+G* level of theory. The structure **int2c** was obtained from the last point of the IRC performed from **ts1c**. 96

5.8 Schematic representation of the pseudorotation cycle for characterization of different envelope and twisted isomers formed due to the ring-puckering motion of a five-membered cyclic ring. 97

5.9 Two classes of diradicals obtained for the asynchronous denitrogenation of **dbh**, plotted on the pseudorotation cycle (a) the envelope $\mathbf{^1E}$ isomers and (b) the twisted $\mathbf{^1T_2}$ isomers. 98

5.10 Variation of energy as a function of ∠HC3C4H (color coded as blue) by performing a relaxed scan at the CASSCF(12,12)/6-31+G* level of theory. The ∠HC3C4H was fixed and the energy was minimized by relaxing the $3N$-7 degrees of freedom. 98

5.11 Potential energy profile for the asynchronous denitrogenation of **dbh** for $\mathbf{^1T_2}$ isomers at the CASSCF(4,4)/6-31+G* level of theory. 99

5.12 Potential energy profile for the formation of **bcp_di** at the CASSCF(4,4)/6-31+G* level of theory 100

5.13 Schematic representation of potential energy profile for the denitrogenation of **dbh** using UB3LYP and M06-2X methods and 6-31+G* basis set. The relative energies at the two level of theories are given in Table 5.5. 101

5.14 Potential energy profile for the formation of cyclopentene, **cpn** from **cpdr** and **bcp** via H-atom shift. The energies (kcal mol^{-1}) are reported with respect to **dbh**. 102

5.15 The initial coordinates r_1 and r_2 (in Å) for the 50 trajectories sampled at **ts1** for E_{total} calculated at 453.15 K. 104

5.16 Representative trajectories: **TrajA**, **TrajB**, and **TrajC**, showing (a) the evolution of the two C-N bond distances r_1 and r_2 with time. **TrajA** and **TrajC** follow the synchronous denitrogenation pathway, whereas **TrajB** follows the asynchronous pathway, (b) the evolution of $v_d = (v_1 - v_2)/2$ with time. The color bar represents the electron density (ρ) of LUMO. As the trajectory progresses with time, a diradical ($\rho > 0.45$, depicted by blue color) is formed and then C-C bond formation between the bridged C-atoms leads to the formation of **bcp**. **TrajA** and **TrajB** show the formation of **bcp** with retention and double inversion of configuration respectively. **TrajC** shows isomerization between **bcp_di** and **bcp_ret**, (c) the formation of different envelope and twisted isomers during the reactions. 105

5.17 Plot of coordinates r_1 versus r_2 for trajectories following (a) synchronous, and (b) asynchronous denitrogenation pathways. The distances r_1 and r_2 are in Å. 106

5.18 Two sample trajectories (a) and (b) showing formation of diradicals during the integration time of 3 ps. The olive and pink colors represent the variation of electron densities in the LUMO and HOMO respectively as a function of time. 107
5.19 Initial geometries of 50 trajectories initiated from the **ts1** region. 109
5.20 Initial geometries of 50 trajectories initiated from the **ts1a** region. 110

LIST OF TABLES

TABLE **Page**

2.1 Summary of the relative energies (ΔE in kcal/mol), number of imaginary frequencies (n_{im}), geometric parameters (C-X bond lengths in Å) of neutral and dicationic species of skeletally substituted cyclopropene, cyclopropane, spiropentadiene, and spiropentane. The parameters are computed at MP2/cc-pVTZ level of theory. The relative energies are reported in kcal mol^{-1} and do not include zero-point energy corrections 24
2.2 Wiberg bond indices for cyclopropene analogues calculated at the MP2/cc-pVTZ level of theory. The hyphen, '-' implies that the structures could not be optimized at the current level of theory 26
2.3 Wiberg bond indices for cyclopropane analogues calculated at at MP2/cc-pVTZ level of theory. The hyphen, '-' implies that the structures could not be optimized at the current level of theory 26
2.4 Wiberg bond indices for spiropentadiene derivatives (X with four valence electrons) at the MP2/cc-pVTZ level of theory 27
2.5 Wiberg bond indices for spiropentadiene analogues (X having two valence electrons) at the MP2/cc-pVTZ level of theory. The hyphen, '-' implies that the structures could not be optimized at the current level of theory 27
2.6 Wiberg bond indices for spiropentane analogues (X with four valence electrons) at th MP2/cc-pVTZ level of theory 28
2.7 Wiberg bond index for spiropentane analogues (X with two valence electrons) at the MP2/cc-pVTZ level of theory. The hyphen, '-' implies that the structures could not be optimized at the current level of theory 28

3.1 Charaterization of **ttX** and **ptX** geometries for X = group 13, 14, and 15 elements. The n_{imag} represents the number of imaginary frequencies for the corresponding stationary point. Energies of **ptX** relative to **ttX** with and without zero point energy corrections i.e. ΔE_{ZPE}, ΔE respectively are given in kcal mol^{-1}, q (X) represents the natural population analysis (NPA) charges on the central atom, X 39
3.2 Relative energies of different stationary points for X = Si at MP2, CASSCF(n,m), and CASPT2 level of theories with cc-pVTZ basis set 43
3.3 Relative energies and important geometrical parameters of different stationary points for X = Al$^-$, Si, and P$^+$ using MP2 and CCSD(T) methods. The energies, angles and distances are reported in kcal mol^{-1}, °, and Å respectively. **ts**† refers to the transition state leading to the formation of **ptX** from **ttX** 45
3.4 Relative energies and important geometrical parameters of different stationary points for X = Ga$^-$, Ge, and As$^+$ using MP2 and CCSD(T) methods. The energies, angles and distances are reported in kcal mol^{-1}, °, and Å respectively. The transition state **ts**† leads to the formation of **ptX** from **ttX**. 50

4.1 Summary of the total energy and number of trajectories initiated for each system. 64
4.2 Important parameters and normal mode frequencies for the stationary points on the PES for the synchronous denitrogenation of 1-pyrazoline, 3,3,5,5-tetrafluoro-1-pyrazoline, and 3,3,5,5-tetrachloro-1-pyrazoline 68
4.3 Number of trajectories following synchronous (Sync), asynchronous (Async), and SOS pathways and showing single inversion (SI), retention (Ret), and double inversion (DI) of configuration during the formation of **cyp** for different E_{total}. The number of trajectories remaining as diradical (DR) during the integration time of 2 ps are also tabulated^a 72
4.4 The 95% confidence interval (CI) for the trajectories following the synchronous, asynchronous, and **sos** pathways for different E_{total}. 73
4.5 Boundary conditions used for d_s and ϕ_s to define the transition state (**ts1/ts1′**) and the second-order saddle region. 75
4.6 Pathways followed by various trajectories dissociating via the **sos** region for an E_{total} of 130, 140, and 150 kcal mol^{-1} 77
4.7 Pathways followed by the trajectories initiated from the **Cl_sos** region for 3,3,5,5-tetrachloro-1-pyrazoline 82

5.1 Active space used for CASSCF (n,m) calculations 89

5.2 Summary of the initial conditions for the trajectory simulations from different regions. 90
5.3 Energetics of the reaction at CASSCF(4,4)/6-31+G* and CASSCF(12,12)/6-31+G* level of theory. The CASPT2(*n*,*m*) calculations were performed by doing a single point calculation on the CASSCF(*n*,*m*) optimized geometries. The energies are reported with respect to **dbh** in kcal mol^{-1} 92
5.4 Effect of basis sets on the energetics of stationary points at the CASSCF(4,4) level 93
5.5 Energetics at the UB3LYP, M06-2X and UMP2 level of theory for different denitrogenation pathways of **dbh** 101
5.6 Statistics of the products (with stereochemistry) and diradicals obtained during the integration time for trajectories initiated from **ts1** 109

CHAPTER 1

INTRODUCTION

Chemical reactions are ubiquitous in nature. In general, a minimum amount of energy known as the activation energy (E_a) is required for a reaction to happen. This energy can be provided to the system thermally, photochemically, or by applying external force to the system. Thermal reactions require the supply of energy to the system in the form of heat, whereas photochemical reactions can take place via electronic or vibrational mode excitation of the system depending upon the light source used i.e. ultraviolet (UV) or infrared light source respectively. Since, the reactions in laboratory are usually carried out under conditions of thermal equilibrium, the experimentally measured rate constants often fails to capture the atomic-level mechanisms. In this regard, various experimental and computational techniques have been developed to study the reaction mechanisms.

Using computational methods to understand reaction mechanisms can help us know the possible pathways before hand and hence allow us to tune the reaction parameters to obtain the desired products. Over a period of time, different computational methodologies using quantum, classical, and semi-classical approaches have been used to study reactions, depending upon the nature and size of the system. In general, chemical reactions can be studied computationally by considering the energetics, and dynamics of the reactions.

1.1 Energetics

The time-independent Schrödinger equation (TIDSE) for a given molecular system of M electrons and N nuclei is given as[1],

$$\hat{H}\Psi(\vec{r},\vec{R}) = E\Psi(\vec{r},\vec{R}) \tag{1.1}$$

where $\hat{H}$ is the Hamiltonian operator for the system, Ψ is the total wave function, and E is the energy of the system. The total wave function of the system, Ψ is a function of both electronic ($\vec{r}$) and nuclear ($\vec{R}$) coordinates. The Hamiltonian operator can be expanded as,

$$\begin{aligned}\hat{H} = &-\frac{\hbar^2}{2m_\mathrm{e}}\sum_i^M \nabla_i^2 - \frac{\hbar^2}{2}\sum_\alpha^N \frac{\nabla_\alpha^2}{M_\alpha} - \frac{e^2}{4\pi\varepsilon_0}\sum_i^M\sum_\alpha^N \frac{Z_\alpha}{r_{i\alpha}} \\ &+\frac{e^2}{4\pi\varepsilon_0}\sum_i^M\sum_{j>i}^M \frac{1}{r_{ij}} + \frac{e^2}{4\pi\varepsilon_0}\sum_\alpha^N\sum_{\beta>\alpha}^N \frac{Z_\alpha Z_\beta}{R_{\alpha\beta}}\end{aligned} \tag{1.2}$$

Here $\hbar$ is $\frac{h}{2\pi}$, where h is the Planck's constant, m_e and M_α are the masses of electrons and nucleus α respectively, and ε_0 is the permitivity of free space. $r_{i\alpha}$ is the distance between electron i and nucleus α, r_{ij} is the distance between electrons i and j, and $R_{\alpha\beta}$ is the distance between nuclei α and β. The terms $-\frac{\hbar^2}{2m_e}\sum_i^M \nabla_i^2$ and $-\frac{\hbar^2}{2}\sum_\alpha^N \frac{\nabla_\alpha^2}{M_\alpha}$ represent the kinetic energy of electrons and nuclei respectively. $-\frac{e^2}{4\pi\varepsilon_0}\sum_i^M\sum_\alpha^N \frac{Z_\alpha}{r_{i\alpha}}$ represents the electron-nucleus attraction, whereas $\frac{e^2}{4\pi\varepsilon_0}\sum_i^M\sum_{j>i}^M \frac{1}{r_{ij}}$ and $\frac{e^2}{4\pi\varepsilon_0}\sum_\alpha^N\sum_{\beta>\alpha}^N \frac{Z_\alpha Z_\beta}{R_{\alpha\beta}}$ are the electron-electron and nuclear-nuclear repulsion terms respectively. As the nuclei are much heavier than the electrons, they move slowly compared to the electrons. Hence, the electrons can be considered as moving in the field of fixed nuclei, and the electronic and nuclear motions can be assumed to be separated. This is known as the Born-Oppenheimer approximation. The total wave function of the system, $\Psi(\vec{r},\vec{R})$ can then be written as,

$$\Psi(\vec{r},\vec{R}) = \psi_\mathrm{elec}(\vec{r};\vec{R})\Phi_\mathrm{nucl}(\vec{R}) \tag{1.3}$$

where $\psi_{\text{elec}}(\vec{r};\vec{R})$ is the electronic wave function that parametrically depends on the nuclear coordinates ($\vec{R}$), and $\Phi_{\text{nucl}}(\vec{R})$ is the nuclear wave function. For a fixed nuclear geometry, the kinetic energy of the nuclei can be neglected and the last term of Eq. 1.2 becomes a constant. Then, the electronic Hamiltonian $\hat{H}_{\text{elec}}$ for the system can be written as,

$$\hat{H}_{\text{elec}} = -\frac{\hbar^2}{2m_e}\sum_{i}^{M}\nabla_i^2 - \frac{e^2}{4\pi\varepsilon_0}\sum_{i}^{M}\sum_{\alpha}^{N}\frac{Z_\alpha}{r_{i\alpha}} + \frac{e^2}{4\pi\varepsilon_0}\sum_{i}^{M}\sum_{j>i}^{M}\frac{1}{r_{ij}} \tag{1.4}$$

and, the nuclear-nuclear repulsion term as,

$$V_{\text{nucl-nucl}} = \frac{e^2}{4\pi\varepsilon_0}\sum_{\alpha}^{N}\sum_{\beta>\alpha}^{N}\frac{Z_\alpha Z_\beta}{R_{\alpha\beta}} \tag{1.5}$$

The electronic Schrödinger equation can now be written as,

$$\hat{H}_{\text{elec}}\psi_{\text{elec}}(\vec{r};\vec{R}) = E_{\text{elec}}\psi_{\text{elec}}(\vec{r};\vec{R}) \tag{1.6}$$

where, E_{elec} is the electronic energy of the system. Therefore, the total energy of the system for a fixed nuclear position can be written as,

$$U(\vec{R}) = E_{\text{elec}}(\vec{r};\vec{R}) + \frac{e^2}{4\pi\varepsilon_0}\sum_{\alpha}^{N}\sum_{\beta>\alpha}^{N}\frac{Z_\alpha Z_\beta}{R_{\alpha\beta}} \tag{1.7}$$

For a fixed nuclear position, the total energy U as a function of $\vec{R}$ constitutes the potential energy surface (PES) for a system.

However, it should be noted that Eq. 1.6 cannot be solved exactly for multi-electron systems and hence different approximations are used. A brief description of some of the approaches used in this thesis are given below.

(i) Hartree-Fock Theory:

In the Hartree-Fock (HF) approximation, the electron-electron repulsion is treated in an average way i.e. an electron experiences the average field due to the presence of all other electrons. The ground state wave function of an M-electron system, is written in the form of a Slater determinant.[1]

$$|\Psi_0\rangle = |\chi_1\chi_2 \cdots \chi_M\rangle \tag{1.8}$$

Here, χ_i represents the spin-orbital of i^{th} electron. The HF equation for a spin-orbital can then be written as,

$$f(i)\chi(x_i) = E\chi(x_i) \tag{1.9}$$

Here, $f(i)$ is the Fock operator and in the atomic-units, it can be written as,

$$f(i) = -\frac{1}{2}\nabla_i^2 - \sum_{\alpha}^{N}\frac{Z_\alpha}{r_{i\alpha}} + v^{\text{HF}}(i) \tag{1.10}$$

where, $v^{\text{HF}}(i)$ is the average potential that the i^{th} electron experiences due to the presence of other electrons. From the variational principle, the best wave function will be the one which gives the lowest ground state energy for the system. The HF equations are solved iteratively until self-consistency is reached.

It should be noted that, in reality the motion of the electrons are correlated. Therefore, the energy obtained using the HF method is always greater than the exact non-relativistic energy ($\mathscr{E}_0$) of the system. Assuming that the HF energy is obtained in a complete basis, the difference in energy between $\mathscr{E}_0$ and the HF energy is defined as the correlation energy of the system.

$$E_{\text{corr}} = \mathscr{E}_0 - E_0 \tag{1.11}$$

Since the HF energy E_0 is always greater than the $\mathscr{E}_0$, the correlation energy is negative. The electron correlation can further be understood in terms of static and dynamic correlations. The instantaneous correlation between the motion of electrons accounts for the dynamic correlation of the system. On the other hand, in cases when a single Slater determinant can no longer represent the system (for instance, when we have degenerate states), the correlation is termed as static. This can be well understood by considering the example of H_2 molecule. The correlation between the electrons is purely dynamic at the equilibrium geometry of H_2, whereas the static correlation gradually increases on increasing the distance between the two H-atoms. Different methods to account for the static and dynamic correlation have been reported in the literature.

(ii) Configuration Interaction:

The Configuration Interaction (CI) method can be used to overcome the deficiencies of the HF wave function. In the CI method, all possible excitations arising due to the promotion of one or more electrons from the occupied to unoccupied molecular orbitals is taken in account. The full CI wave function can be written as[1],

$$|\Phi_{\text{CI}}\rangle = c_0\,|\Psi_0\rangle + \sum_{ar} c_a^r\,|\Psi_a^r\rangle + \sum_{\substack{a<b\\ r<s}} c_{ab}^{rs}\,|\Psi_{ab}^{rs}\rangle + \sum_{\substack{a<b<c\\ r<s<t}} c_{abc}^{rst}\,|\Psi_{abc}^{rst}\rangle + \ldots \tag{1.12}$$

where $|\Psi_0\rangle$ is the ground state HF determinant, and $|\Psi_a^r\rangle$, $|\Psi_{ab}^{rs}\rangle$, $|\Psi_{abc}^{rst}\rangle$... account for the single, double, triple... excitation of electrons respectively. The CI wave function can also be written as a linear combination of the HF wave function and all possible excited-state configuration state functions, CSFs (which are eigen functions of both $\hat{S}_z$ and $\hat{S}^2$ operators),

$$\Phi_{\text{CI}} = c_0\Psi_0 + \sum_k c_k\Psi_k \tag{1.13}$$

Given the trial wave function Φ_{CI} in the complete basis, the energy calculated using the CI method will be same as that obtained by solving the many electron Schrödinger equation. However, it should be noted that the number of CSFs increases considerably with the number of electrons and the number of basis functions for the system. Hence, it becomes practically impossible to perform a full CI calculation even for a small system. To overcome this problem, different methods which include truncation of the excited configurations have been proposed in literature. For eg. CI with singles (CIS) means only the single excitations are included, whereas CI with singles and doubles (CISD) includes both singly and doubly excited configurations.

(iii) Multi-configuration Self-Consistent Field Method:

In the Multi-configuration Self-Consistent Field (MCSCF) approach, the molecular wave function is written as a linear combination of CSFs.[2] In this method, both the expansion coefficients of the CSFs and the coefficients in the molecular orbitals are varied simultaneously to minimize the variational integral. Since both the CSF and orbital coefficients are varied, the amount of calculation for MCSCF methods is large. However, advances in different methods for computing MCSCF wave functions have led to its wide usage.

The most commonly used MCSCF method is the Complete Active-Space Self-Consistent Field (CASSCF) method. In this method, the orbitals are divided into a set of active, inactive, and virtual orbitals (Figure 1.1). The electrons that are not present in the inactive orbitals are referred as active electrons. The inactive orbitals are doubly occupied and the virtual orbitals remain unoccupied in all the CSFs. In the CASSCF method, all possible excitations (which give the same spin and symmetry as the state under consideration) of the active electrons in the active orbitals are taken into consideration to generate the CSFs. The CASSCF wave function is written as a linear combination of all the CSFs (Φ_i) that are formed by exciting the active electrons to the active orbitals.

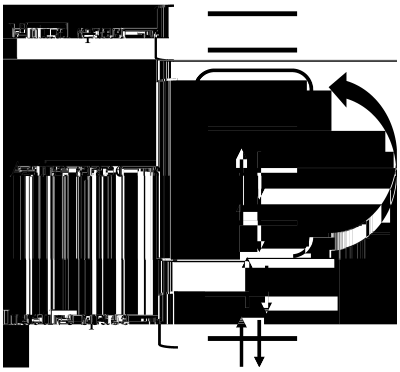

Figure 1.1: Characterization of orbitals into inactive, active, and virtual spaces in a CASSCF calculation.

$$\psi_{\text{CASSCF}} = \sum_i b_i \Phi_i \tag{1.14}$$

The MCSCF calculation is then performed to get the optimum orbital and expansion coefficients. The CASSCF method takes care of the static correlation of electrons, but fails to account for the dynamic correlation of the system.

One way to account for the dynamic correlation of electrons is the Complete Active-Space Perturbation Theory (CASPT2). In the CASPT2 method, the Hamiltonian is written as,

$$\hat{H} = \hat{H}_0 + \lambda \hat{H}' \tag{1.15}$$

where, $\hat{H}_0$ is the zeroth-order Hamiltonian and $\hat{H}'$ is the perturbation with a small perturbation parameter λ. Here, the CASSCF wave function is used as the zeroth-order wave function and the dynamic correlation is treated in a perturbative manner.

(iv) Møller-Plesset Perturbation Theory:

Another way of incorporating the electron correlation is the Møller-Plesset Perturbation (MPn, n represents n^{th}-order) technique.[3] The Hamiltonian operator is given as,

$$\hat{H} = \hat{H}_0 + \lambda \hat{H}' \tag{1.16}$$

where $\hat{H}_0$ is the reference Hamiltonian, $\hat{H}'$ and λ are the perturbation and the parameter defining the strength of the perturbation. Let us consider that $\hat{H}'$ is time independent. The perturbed Schrödinger equation can be written as,

$$\hat{H}\Psi = E\Psi \tag{1.17}$$

For λ = 0, $\hat{H}$ = $\hat{H}_0$. As the perturbation increases, the wave function and energy change continuously and can be expanded using the Taylor series as,

$$\begin{aligned} E &= \lambda^0 E_0 + \lambda^1 E_1 + \lambda^2 E_2 + ... \\ \Psi &= \lambda^0 \Psi_0 + \lambda^1 \Psi_1 + \lambda^2 \Psi_2 + ... \end{aligned} \tag{1.18}$$

λ = 0, gives the unperturbed or zeroth-order wave function (Ψ_0) and energy, which is the ground state HF wave function and energy of the system. Ψ_1, Ψ_2,... and E_1, E_2,... represent the first-order, second-order,... corrections to the wave function and energy respectively. Substituting Eq. 1.16 and 1.18 in the Schrödinger equation and separating the terms with like powers of λ, we get the zero-, first-, second-,..., n^{th}-order perturbation equations. It can be shown that, the first-order correction to the ground state energy of the system using the above method yields the HF energy.

$$E_{\text{MP1}} = E_0 + E_1 = E_{\text{HF}} \tag{1.19}$$

The second-order correction can be written as,

$$E_2 = \sum_{a<b}^{\text{occupied}} \sum_{r<s}^{\text{virtual}} \frac{\langle \Psi_0 | \hat{H}' | \Psi_{ab}^{rs} \rangle \langle \Psi_{ab}^{rs} | \hat{H}' | \Psi_0 \rangle}{E_0 - E_{ab}^{rs}} \tag{1.20}$$

Therefore,

$$E_{\text{MP2}} = E_{\text{HF}} + \sum_{a<b}^{\text{occupied}} \sum_{r<s}^{\text{virtual}} \frac{\langle \Psi_0 | \hat{H}' | \Psi_{ab}^{rs} \rangle \langle \Psi_{ab}^{rs} | \hat{H}' | \Psi_0 \rangle}{E_0 - E_{ab}^{rs}} \tag{1.21}$$

where, E_{MP2} gives the MP2 energy with the energy corrections up to second-order. It has been observed that MP2 accounts for $\sim$ 80-90% of the electron correlation energy, and hence is widely used.

(v) Density Functional Theory:

An alternative way of computing the electronic energies of a system is by using the Density Functional Theory (DFT).[2,3] According to Hohenberg and Kohn theorem[4], the ground state electronic energy, wave function and all other electronic molecular properties can be uniquely determined by the electron density, $\rho(r)$ of the system. The energy components depend on the electron density, which in turn depends on the coordinates (r). Kohn and Sham considered a fictitious system of n non-interacting particles such that the probability density $\rho(r)$ of the fictitious system is same as the real system under consideration.[5] Thus, the correction to the kinetic energy of electrons,

$$\Delta T = T[\rho(r)] - T_{\text{elec}}[\rho(r)] \tag{1.22}$$

where, $T[\rho(r)]$ is the kinetic energy of the electrons in the real system and $T_{\text{elec}}[\rho(r)]$ represents the kinectic energy of the electrons in the fictitious system with non-interacting particles.

The total energy can then be represented as,

$$E[\rho(r)] = T_{\text{elec}}[\rho(r)] + J[\rho(r)] + V_{\text{nucl-elec}}[\rho(r)] + E_{\text{xc}}[\rho(r)] \tag{1.23}$$

Here, $V_{\text{nucl-elec}}[\rho(r)]$ represents the attraction between the nucleus and electron, $J[\rho(r)]$ and $E_{\text{xc}}[\rho(r)]$ define the Coulomb repulsion and the exchange-correlation parts. Also,

$$E_{\text{xc}}[\rho(r)] = \Delta T + (V_{\text{elec-elec}}[\rho(r)] - J[\rho(r)]) \tag{1.24}$$

where, $V_{\text{elec-elec}}[\rho(r)]$ is the electron-electron repulsion term. The E_{xc} is the only unknown parameter and different approximate models have been developed to model this part.

(vi) Basis Sets:

The trail wave function of a system can be written as a linear combination of basis functions.[1–3] This is referred as the basis set. Two different types of basis functions namely the Slater Type Orbitals (STOs), and the Gaussian Type Orbitals (GTOs) are commonly used. The STO can be written as,

$$\Phi(r,\theta,\phi) = N_c Y_{l,m}(\theta,\phi) r^{n-1} e^{-\zeta r/a_0} \tag{1.25}$$

where, N_c and ζ are the normalization constant and the Slater orbital exponent respectively and $Y_{l,m}$ is the spherical harmonics function. The STO do not have any radial node but these can be obtained by taking a linear combination of STOs. Also, the analytical calculation of three- or four-centered two-electron integrals are computationally difficult.

Hence, another type of basis function, GTOs was developed by Boys and coworkers in 1950. The GTO can be written as,

$$\chi_{ijk} = N_c x_a^i y_a^j z_a^k e^{-\zeta \alpha r^2} \tag{1.26}$$

where i, j, and k are non-negative exponents and α is the orbital exponent. x, y, z are the Cartesian coordinates of the nucleus centered at a, and r represents the distance to nucleus a. Multiple such GTOs are combined to mimic the shape of a STO. GTOs are computationally less expensive and hence are widely used. The minimum number of functions used to represent all the electrons of the system constitutes a minimal basis set. A double zeta (DZ) type basis refers to doubling of all the basis functions, whereas a valence double zeta (VDZ) represents doubling of only the valence basis functions. Similarly, a triple zeta (TZ) contains three times the number of basis functions present in the minimal basis set. Polarization, diffusion, and correlation functions can also be added in the basis sets for required systems.

(vii) Potential Energy Surface:

The PES is a $3N$-6 dimensional surface that describes the variation of U, (Eq. 1.7) as a function of the $3N$-6 nuclear coordinates, $\vec{R}$. Stationary points on the PES are as those which have the first derivative of U with respect to R_i equal to zero[3] i.e.,

$$\frac{\partial U}{\partial R_i} = 0 \qquad \text{where, } i = 1,2,...,3N-6 \tag{1.27}$$

The different stationary points on the PES can then be classified as minima or n^{th}-order saddle points depending on the curvature of the PES. Here, it is convenient to work with orthogonal normal mode coordinates $Q_1, Q_2 ... Q_{3N-6}$. For a minimum, the curvature along all the $3N$-6 orthogonal directions ($\vec{Q}$) are positive i.e.,

$$\frac{\partial^2 U}{\partial Q_i^2} > 0 \qquad \text{where, } i = 1,2,...,3N-6 \tag{1.28}$$

On the contrary, for a n^{th}-order saddle point, the curvature is negative along n-directions and positive along the remaining $3N$-6-n directions, i.e.

$$\begin{aligned} \frac{\partial^2 U}{\partial Q_j^2} &< 0 \qquad \text{where, } j = 1,2,...,n \\ \frac{\partial^2 U}{\partial Q_i^2} &> 0 \qquad \text{where, } i = n+1, n+2, ..., 3N-6-n \end{aligned} \tag{1.29}$$

Therefore, a transition state has one imaginary frequency, a second-order saddle has two imaginary frequencies and so on.

1.2 Dynamics

The potential energy profiles describe the different pathways possible for a reaction to proceed. However, a real system is dynamical in nature, and hence it is important to study the time evolution of the system to understand the atomic-level mechanisms. The dynamics of a system can be studied by solving the time dependent Schrödinger equation (TDSE).[1]

$$i\hbar\frac{\partial}{\partial t}\Psi(\vec{R},t) = \hat{H}\psi(\vec{R},t) \tag{1.30}$$

Here, $\Psi(\vec{R},\, t)$ represents the wave function of the system. However, it should be noted that quantum dynamics is very expensive and hence is computationally not feasible for large systems.

Another way to study the dynamical nature of a system is by solving the classical equations of motion (EOM). For example, the Newton's EOM can be used to understand the dynamics in the Cartesian coordinate system $(\mathbf{x_1}, \mathbf{x_2}, \mathbf{x_3}, ...\mathbf{x_N})$, where $\mathbf{x_i} \equiv (x_i, y_i, z_i)$.

$$\begin{aligned} \mathbf{F_i} &= m\mathbf{a_i} = m_i\frac{\partial^2\mathbf{x_i}}{\partial t^2} \\ -\frac{\partial V}{\partial \mathbf{x_i}} &= m_i\frac{\partial^2\mathbf{x_i}}{\partial t^2} \end{aligned} \tag{1.31}$$

$-\frac{\partial V}{\partial \mathbf{x}_i}$ represents the force acting on i^{th} particle of mass m_i corresponding to the coordinate R_i. Eq. 1.31 is solved numerically for each time step to get the positions and conjugate momenta, hence giving a trajectory.

In the present thesis, the forces on the system are computed on-the-fly at a given level-of-theory and the time evolution of the system is studied by solving the Newton's equation.[6] This procedure is known as *ab initio* classical dynamics simulation and has been used to understand the atomic-level mechanisms of chemical reactions involving several atoms.[7–13] The initial conditions of the trajectories are sampled using microcanonical normal mode or Boltzmann sampling techniques at a particular temperature.[14]

(i) Microcanonical Normal Mode Sampling:

In the microcanonical normal mode sampling technique[14], a total energy E is added to the n normal modes present in a molecule. The probability that E_1 amount of energy is given to normal mode 1 is proportional to the number of ways in which the remaining energy (E-E_1) can be distributed in (n-1) oscillators, which is given by the classical density of states of the oscillators. The energy for i^{th} mode can be written as,

$$E_i = (E - \sum_{j=1}^{i-1} E_j)(1 - R_i^{1/(n-1)}) \tag{1.32}$$

where R_i is a freshly generated random number. The normal mode coordinates and momenta for the i^{th} mode are then chosen as,

$$\begin{aligned} Q_i &= A_i \cos(2\pi R_i) \\ P_i &= -\omega_i A_i \sin(2\pi R_i) \end{aligned} \tag{1.33}$$

where, ω_i = $2\pi\nu_i$ (ν_i is the vibrational frequency), and A_i is the normal mode amplitude and is given as $(2E_i)^{1/2}/\omega_i$. The Q_i and P_i are then transformed to the Cartesian coordinates and momenta as,

$$\begin{aligned} \mathbf{q} &= \mathbf{q_0} + \mathbf{M}^{(-1/2)}\mathbf{LQ} \\ \mathbf{p} &= \mathbf{M}^{(-1/2)}\mathbf{LP} \end{aligned} \tag{1.34}$$

where, **L** is the normal mode eigen vector matrix, **M** is the diagonal matrix with atomic masses and $\mathbf{q_0}$ corresponds to the vector with equilibrium coordinates. Any spurious angular momentum ($\mathbf{j_s}$) generated during this transformation is calculated and the desired angular momentum, $\mathbf{j_0}$ is added to the molecule by forming a vector,

$$\mathbf{j} = \mathbf{j_0} - \mathbf{j_s} \tag{1.35}$$

and by adding the rotational velocity, $\omega \times \mathbf{r_i}$ (where ω = $\mathbf{I^{-1}j}$ and **I** is the inertia tensor) to each of the atoms. The internal energy is then calculated and compared to the desired energy.

If these two energies do not agree within the acceptance criteria of 0.1%, the Cartesian coordinates and momenta are rescaled. Any spurious center-of-mass translation energy is subtracted and the steps from Eq. 1.35 are performed again.

(i) Boltzmann Sampling:

In this technique, the normal modes are sampled using a Boltzmann distribution at a particular temperature, T_{vib}. The quantum number m_i (i represents the i^{th} mode) is sampled using the following probability distribution.[14]

$$P(m_i) = \exp(-m_i h\nu_i/k_{\text{B}}T_{\text{vib}})[1-\exp(h\nu_i/k_{\text{B}}T_{\text{vib}})] \tag{1.36}$$

Here ν_i corresponds to the vibrational frequency for the i^{th} mode.

1.3 Rate Theories

(i) Transition state theory:

The Transition state theory (TST) provides a description to calculate the rate of chemical reactions.[15] It is assumed that the reactants and transition states are in thermal equilibrium with each other. Also, the reaction coordinate can be separated from other motions and can be simply treated as a translation. Moreover, no recrossing is allowed i.e. if a molecule crosses the transition state, it forms the product. Based on these assumptions, the TST rate constant expression can be written as,

$$k_{\text{TST}} = \sigma \frac{k_{\text{B}}T}{h} \frac{Q^{\dagger}}{Q_{\text{A}}Q_{\text{B}}} \exp(-E_a/k_{\text{B}}T) \tag{1.37}$$

Here, σ, k_{B}, h, E_a, and T are the statistical factor, Boltzmann constant, Planck's constant, barrier for the reaction, and temperature respectively. $Q^{\dagger}$ is the partition functions for the transition state, and Q_{A}, Q_{B} are partition functions for the reactants. The ratio $\frac{k_{\text{B}}T}{h}$ is defined as the frequency factor, and is used to describe the magnitude of encounter between molecules.

However it should be noted that in general, a transition state is defined as a 6N-1 dimensional surface in the phase space (N is the number of atoms in the system).[16] Hence, in general many recrossing events are observed in chemical reactions leading to a lower rate constant for the reaction as compared to k_{TST}.

(ii) Rice-Ramsperger-Kassel-Marcus theory:

The Rice-Ramsperger-Kassel-Marcus (RRKM) theory is based on the RRK theory and considers the rotational and vibrational energies explicitly and includes the zero-point energy of the system. The RRKM theory provides the connection between the transition state theory and the statistical unimolecular rate theory.[15] The molecule is assumed to be a collection of coupled harmonic oscillators and the rate of the intramolecular vibrational energy redistribution in the system is assumed to be much higher as compared to the rate of the reaction. A general mechanism of an energized molecule A^* to form products can be written as,

$$\mathrm{A}^* \longrightarrow \mathrm{A}^\dagger \longrightarrow \text{Product}$$

Here A^* and $\mathrm{A}^\dagger$ are the energized molecule and the critical configuration of the molecule respectively. The internal degrees of freedom for A^* and $\mathrm{A}^\dagger$ are then classified as active (energy exchange can happen freely) and adiabatic (remains in the same quantum state throughout the reaction) modes. In general, the internal rotations and vibrations are treated as the active modes, whereas the external rotation is treated adiabatically. Using these approximations, the RRKM rate constant expression can be written as,

$$k(E) = \frac{G^\dagger(E-E_0)}{hN(E)} \tag{1.38}$$

where h is the Planck's constant, $G^\dagger(E-E_0)$ and $N(E)$ are the sum of states at the transition state and density of states at the reactant respectively. Here E is the total energy available to the system from the reactant and E_0 is the energy of the transition state with respect to the reactant.

The present thesis involves investigating reaction mechanisms using *ab initio* and DFT methods. The potential energy profiles for the different reactions pathways were mapped at a given level of theory. The dynamics of the systems were also studied using *ab initio* classical dynamics simulation technique. In the *ab initio* classical trajectory method the forces necessary for the integration of the EOM are calculated on-the-fly at a given level of theory.

CHAPTER 2

STEREOMUTATION IN TETRACOORDINATED CENTERS VIA STABILIZATION OF PLANAR TETRACOORDINATED SYSTEMS

2.1 Introduction

Van't Hoff[17] and Le Bel's[18] independent discovery of the preference of a tetrahedral geometry by a tetracoordinated carbon has been a cornerstone in chemistry. A linear combination of $2s$ and three $2p$ ($2p_x$, $2p_y$, and $2p_z$) atomic orbitals of carbon leads to the formation of a set of four sp^3 hybridized orbitals. The orbitals interfere in a constructive or destructive manner to generate the four sp^3 hybridized orbitals, which are oriented at the four corners of a tetrahedron. The preference of a tetrahedral geometry was so profound that it took almost 100 years for the planar tetracoordinated centre (**ptc**) to be considered as an alternative possibility for carbon compounds. The first model of a planar methane was formulated by Hoffmann in 1970.[19] However, the stabilization of planar tetracoordinated carbon (**ptC**) has been a challenging task for chemists and different ways have been proposed to stabilize **ptC**.

The transformation of a tetrahedral tetracoordinated carbon (**ttC**) to **ptC** can be best understood by looking at the Walsh diagram of the valence occupied molecular orbitals (MOs), Figure 2.1. On going from **ttC** to **ptC**, the totally symmetric $1a_1$ MO gets transformed to $1a_{1g}$.

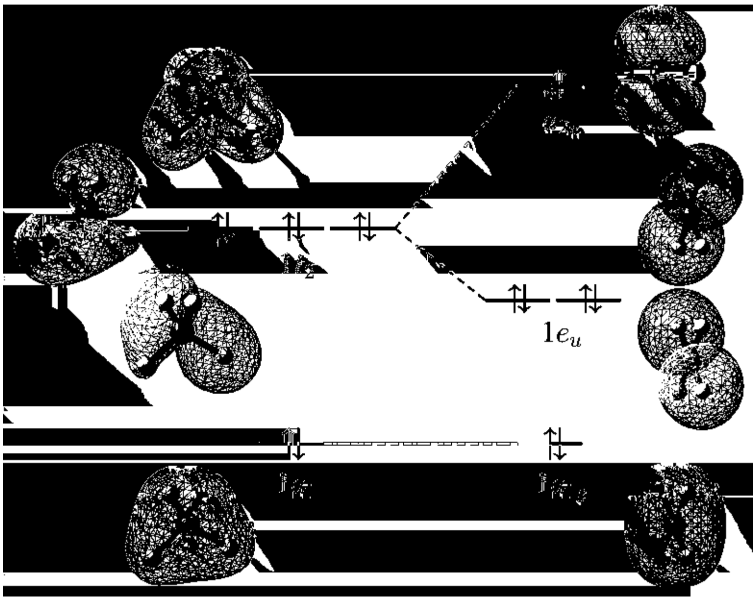

Figure 2.1: Walsh diagram of the valence occupied molecular orbitals for the transformation of tetrahedral to planar CH_4. The molecular orbitals are calculated at HF/STO-3G level of theory.

Interestingly, the triply degenerate set of orbitals $1t_2$ gets transformed to a set of doubly degenerate orbital ($1e_u$), and a non-bonding orbital, a_{2u} in **ptC**. For **ptC** to have four σ bonds (i.e. four C-H bonds in case of CH_4), eight bonding electrons are needed. However, the presence of six bonding electrons in **ptC** leads to the formation of electron deficient bonds. Thus, two 2-centered-2-electron and one 3-centered-2-electron bonds are expected to form using the six bonding electrons in **ptC**.[19] The presence of electron deficient bonds and a lone pair of electron on the central carbon atom, leads to the destabilization of **ptC**. Tuning these parameters chemists have been trying to stabilize the **ptc** and several molecules with **ptC** have been reported.[20–29]

Hoffmann, Alder, and Wilcox were the first to address the problem of stabilization of (**ptC**) and suggested different strategies for the same.[23] Utilizing σ donor and π acceptor ligands leads to the stabilization of **ptC** by providing σ-electron density to the electron deficient bonds and accepting the π-electron density from the lone pair of electrons present. Another viable strategy for the stabilization of **ptC** is removal of the lone pair of electrons present on the central carbon, hence leading to the formation of a dicationic species. Addition of small rings has also been proven to stabilize the **ptC** by making the system sterically rigid and hence decreasing the repulsion between the bond pair of electrons.[30–32]

Utilizing these concepts, the first ever **ptC**s were reported by Scheleyer and coworkers in 1976. They identified that the di-lithium substituted **ptC**s of cyclopropane and cyclopropane analogues are minimum on the PES.[33] Followed by this, Cotton and Miller synthesized the first compound with a **ptC** center in 1977.[34] Since then, various **ptC** compounds have been identified both experimentally[21,35–45] as well as theoretically[20,22–29,46–64] by exploiting the factors explained above. Efforts have also been made to stabilize **ptC** so that it can act as a transition state for the interconversion between two tetrahedral isomers. However, very less triumph has been achieved in this area, because for systems with stable **ptC**, the **ttC** is a higher order saddle point and vice versa.

In this chapter, we exploit the electronic and steric factors discussed above to identify systems with stable **ptc**. We have used different valence isoelectronic species of carbon, from group 13, 14, and 15 to stabilize heteroatom substituted planar tetracoordinated systems, **ptXs**.

2.2 Methodology

We have used two different classes of systems to investigate the stability of **ptX**s. The first class of compounds belong to cyclic three-membered analogues and the second class belongs to spiro[2,2]-type analogues. It should be noted that the model systems C_3H_4 and C_5H_4 were previously studied by Schleyer and coworkers in 1988.[65] In this study we have investigated different saturated and unsaturated analogues of C_3H_4 and C_5H_4 with the central atom being substituted with various valence isoelectronic species of carbon, from group 13, 14, and 15 elements. The tetrahedral and planar tetracoordinate systems, **ttX** and **ptX** respectively were

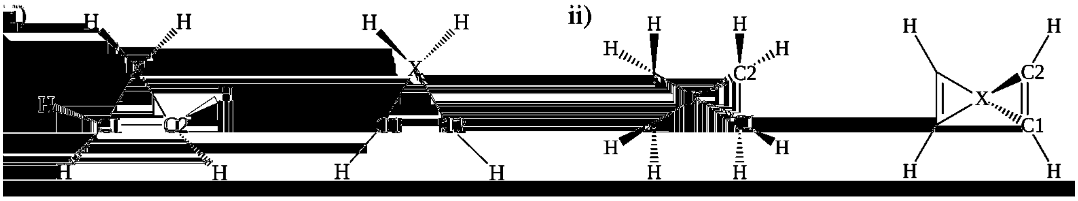

Figure 2.2: Two different skeleton models used in this study (i) three membered cyclic analogues, (ii) spiro[2,2]-type analogues. The central atom X is substituted with various valence isoelectronic species of carbon from group 13, 14, and 15.

optimized at MP2/cc-pVTZ[66,67] level of theory. The stationary points on the PES were characterized by performing the normal mode analysis. The transition states were connected to the respective intermediates by performing the intrinsic reaction coordinate (IRC) calculations.[68] All the results discussed here are obtained at MP2/cc-pVTZ level of theory unless stated otherwise. The role of aromaticity in stabilization of **ptC** were examined by performing Nuclear Independent Chemical Shift (NICS) calculations[69] at the same level of theory. A ghost atom was placed at the center of the rings to calculate the isotropic magnetic shielding values. A negative and positive NICS value indicates that the system is aromatic and anti-aromatic respectively. All the calculations were performed using Gaussian16 software package.[70] The relative energies are calculated with respect to the respective **ttX** geometries in kcal mol^{-1}.

2.3 Results and Discussion

2.3.1 Stabilization of ptC

The tetrahedral form of methane, CH_4 is undoubtedly a minimum on the PES, whereas its planar conformation is a third-order saddle point.[71] However the methane dication, CH_4^{2+} observed experimentally in gas phase, was said to have a planar structure by comparing the C-H bond distances with those obtained theoretically.[72] Similarly, the tetrahedral form of cyclopropane, C_3H_6 is a minimum whereas its corresponding planar form is a second-order saddle point and is 111 kcal mol^{-1} higher in energy with respect to the former. One would expect that the removal of the lone pair of electrons present on the central carbon atom will lead to stabilization of the **ptC** in case of $[C_3H_6]^{2+}$. However, we could not obtain the **ptC** at the current level of theory and the **ttC** was found to be a second-order saddle point on the PES.

In order to stabilize the **ptC**, we then incorporated π electron clouds to the system i.e. cyclopropene. The tetrahedral form of C_3H_4 is a minimum whereas the corresponding **ptC** was found to be a third-order saddle with an energy of $\sim$ 117 kcal mol^{-1} higher than the corresponding **ttC**. Interestingly, removal of the lone pair of elctrons from the central carbon atom leads to stabilization of the **ptC** in case of C_3H_4. The **ptC** for $[C_3H_4]^{2+}$ was found to be a minimum[65] on the PES whereas the corresponding **ttC** was unstable and could not be optimized. This can be understood by looking at the transformation of molecular orbitals from **ttC** to **ptC** for C_3H_4 and $[C_3H_4]^{2+}$. Figure 2.3 clearly shows that on going from **ttC** to **ptC** of C_3H_4, one of the σ_{CC} MOs is transformed to a lone pair of electrons, hence making the four C-H bonds electron deficient which leads to the destabilization of the **ptC**. On the contrary, removal of two electrons from C_3H_4, makes the **ptC** stable for the dicationic C_3H_4 by reducing the electronic charge from the central carbon (Figure 2.3 (b)).

Formation of cage-like structures, that introduce mechanical strain has also been proven effective for the stabilization of **ptC**.[23,73–76] Hence, we have considered spiropentane, C_5H_8 and its unsaturated analogue C_5H_4 in the present study. As expected, the **ttC** spiropentadiene, C_5H_4 is a minimum on the PES whereas, the **ptC** was found to be a fourth-order saddle point. However, the energy difference between the **ttC** and **ptC** has now been reduced to 92.7 kcal mol^{-1} as compared to 117.4 kcal mol^{-1} in case of cyclopropene. In addition, the removal of two electrons from spiropentadiene i.e. $[C_5H_4]^{2+}$ leads to stabilization of **ptC**, hence making it a minimum on the PES. The **ttC** now becomes a higher order saddle point with a barrier of

20 kcal mol^{-1}. Similar to cyclopropane, the **ttC** of spiropentane was found to be a minimum whereas the **ptC** as higher order saddle point. On the contrary, removal of two electrons leads to stabilization of **ptC**, hence making it a minima on the PES.

Summarizing, the above results indicate that the reduction of the electronic charge on the central atom facilitated by electronic delocalization in the ring leads to stabilization of **ptC**. Moreover, cyclopropene and spiropentadiene dications can be considered aromatic as they are cyclic compounds with $(4n+2)$ π electrons ($n = 0$). The HOMO of **ptC** of the dicationic cyclopropene closely resembles that of classic cyclopropyl cation and maybe responsible for the possible aromatic stabilization. Similar effect is also observed in the **ptC** of dicationic spiropentadiene molecule. This was further examined by calculating the NICS values at the geometric centers of the rings. The computed NICS values changes from 11.28 to −41.76 for the **ptC** of C_5H_4 to $[C_5H_4]^{2+}$ respectively. This clearly indicates that the stabilization gained

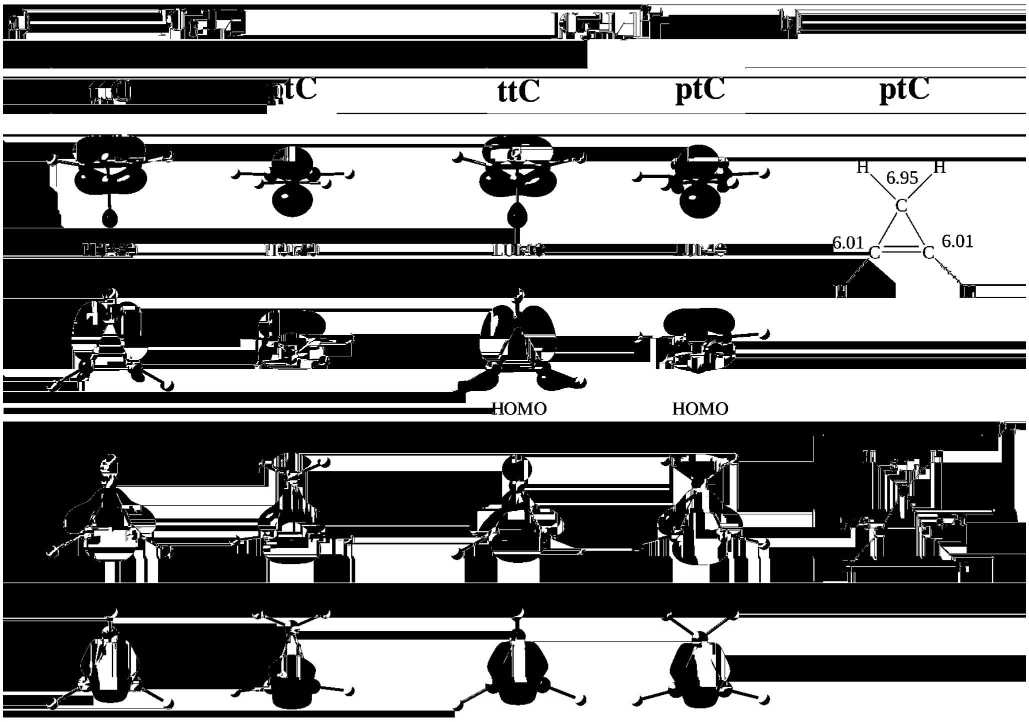

Figure 2.3: (a) MO transformation on going from **ttC** to **ptC** for C_3H_4 and $[C_3H_4]^{2+}$, and (b) Atomic electron population obtained using natural population analysis. The MOs and the atomic populations are calculated at HF/cc-pVTZ level of theory.

due to the aromatic nature of the latter system. The aromatic nature of planar tetracoordinated systems has also been explained using the negative NICS values in literature.[51,57,77] For planar $[C_3H_4]^{2+}$, the NICS value was found to be -45.96 whereas the same could not be computed for planar neutral C_3H_4, because the stationary point could not be identified at the current level of theory.

2.3.2 Stabilization of Planar Tetracoordinated Centers with Heteroatom (X) Substitution

To identify systems with stable planar tetracoordinated centers, we now substituted the central carbon atom in the skeletal systems discussed above with various valence isoelectronic species from group 13, 14, and 15 (i.e. X = B^-, N^+, Al^-, Si, P^+, Ga^-, Ge, and As^+). For example, the model cyclopropene systems with the central heteroatom X can be expressed as, $[XC_2H_4]^-$ (X = B, Al, and Ga), $[XC_2H_4]$ (X = C, Si, and Ge), and $[XC_2H_4]^+$ (X = N, P, and As). As seen in the carbon systems, here also the **ttX**s were found to be minimum on the PES for the cyclopropane and spiropentane analogues. In contrast, the **ptX**s were found to be either transition states or higher order saddle points. It was also observed that, the relative barriers of **ptX**s, decrease on going from X = second to third period elements ($B^- \rightarrow Al^-$, $C \rightarrow Si$, $N^+ \rightarrow P^+$) and then increase on going to X = fourth period elements, following a trend similar to their electronegativities. Also, the X-C bond lengths increase on going down the group and decrease on moving along the period (see Table 2.1 for details).

As discussed above, the removal of lone pair of electrons helps in the stabilization of **ptX**s. To this end, we also investigated the electronic structures of saturated and unsaturated analogues of the cyclopropane and spiropentane systems with two valence electrons. Interestingly, the **ptX**s for $[XC_2H_6]^{2+}$ (X = B^-, Al^-, and Ga^-) were minimum on the PES, whereas the corresponding **ttX**s were transition states corresponding to the interconversion between two **ptX**s. In contrast, for $[XC_2H_6]^{2+}$, X = N^+, P^+, and As^+, the **ptX**s were found to be tran-

Table 2.1: Summary of the relative energies (ΔE in kcal/mol), number of imaginary frequencies (n_{im}), geometric parameters (C-X bond lengths in Å) of neutral and dicationic species of skeletally substituted cyclopropene, cyclopropane, spiropentadiene, and spiropentane. The parameters are computed at MP2/cc-pVTZ level of theory. The relative energies are reported in kcal mol^{-1} and do not include zero-point energy corrections

		Four valence electrons				Two valence electrons			
		ttX		**ptX**		**ttX**		**ptX**	
X		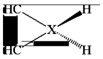	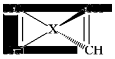	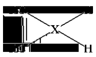	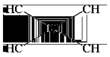	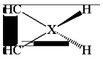	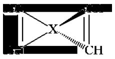	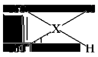	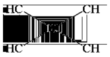
B^-	ΔE, n_{im}	0.0, 0	0.0, 0	81.5, 3	46.5, 3	0.0,- [a]	0.0, 1	−29.1, 0	−27.2, 0
	X-C1	1.61	1.58	1.66	1.62	1.43	1.84	1.68	1.55
Al^-	ΔE, n_{im}	0.0, 0	0.0, 0	29.0, 1	13.3, 1	0.0, 2	0.0, 1	−149.7, 0	-7.5, 1
	X-C1	1.95	1.93	1.96	1.94	1.97	2.29	2.32	1.97
Ga^-	ΔE, n_{im}	0.0, 0	0.0, 0	40.5, 2	19.3, 2	0.0,2	0.0,- [a]	−152.9,0	−69.4,0
	X-C1	1.99	1.96	2.01	1.98	1.99	1.97	2.31	1.95
C	ΔE, n_{im}	0.0, 0	0.0, 0	117.4, 3	92.7, 4	0.0,- [a]	0.0, 2	−62.6,0	−19.3, 0
	X-C1	1.53	1.48	1.83	1.53	1.46	1.76	1.50	1.48
Si	ΔE, n_{im}	0.0, 0	0.0, 0	49.5, 1	23.5, 1	0.0, 2	0.0, 1	−9.5, 0	−6.4, 1
	X-C1	1.82	1.80	1.81	1.80	2.20	2.15	2.06	1.88
Ge	ΔE, n_{im}	0.0, 0	0.0, 0	59.6, 1	28.9, 1	0.0, 2	0.0, 1	−9.5, 0	−12.7, 1
	X-C1	1.91	1.89	1.91	1.90	2.30	2.22	2.13	1.93
N^+	ΔE, n_{im}	0.0, 0	0.0, 0	77.0, 3	97.0, 4	0.0, 0	0.0, 2	−4.5, 1	−0.8, 1
	X-C1	1.50	1.46	1.72	1.56	1.40	1.89	1.48	1.50
P^+	ΔE, n_{im}	0.0, 0	0.0, 0	75.2, 1	36.1, 1	0.0, 2	0.0, 2	−64.9, 1	−3.6, 1
	X-C1	1.75	1.72	1.73	1.72	1.85	2.12	2.01	1.83
As^+	ΔE, n_{im}	0.0, 0	0.0, 0	80.6, 1	39.8, 1	0.0, 1	0.0, 2	−79.9, 1	−5.7, 2
	X-C1	1.88	1.85	1.86	1.84	1.97	2.25	2.13	1.94
		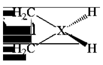	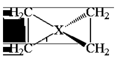	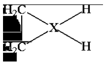	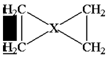	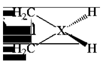	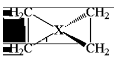	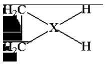	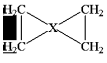
B^-	ΔE, n_{im}	0.0, 0	0.0, 0	140.5, 3	105.1, 3	0.0, 1	0.0,- [a]	−9.2, 0	−129.5, 0
	X-C1	1.61	1.58	1.60	1.68	2.02	1.37	1.82	1.61
Al^-	ΔE, n_{im}	0.0, 0	0.0, 0	43.0, 1	30.9, 1	0.0,1	0.0, 1	−0.6, 0	−13.8, 1
	X-C1	1.99	1.97	2.0	1.99	2.42	2.38	2.39	2.03
Ga^-	ΔE, n_{im}	0.0, 0	0.0, 0	58.6, 2	51.8, 3	0.0, 1	0.0, 1	−1.7, 0	−24.2, 1
	X-C1	2.0	1.98	2.06	2.03	2.42	2.33	2.35	2.0
C	ΔE, n_{im}	0.0, 0	0.0, 0	110.9, 2	102.4, 3	0.0, 2	0.0, 3	29.4, - [a]	−20.0, 0
	X-C1	1.50	1.48	1.66	1.53	1.90	1.91	1.54	1.55
Si	ΔE, n_{im}	0.0, 0	0.0, 0	77.7, 1	60.5, 1	0.0, 2	0.0, 2	−0.9, 1	−10.4, 1
	X-C1	1.86	1.84	1.86	1.85	2.42	2.28	2.22	1.94
Ge	ΔE, n_{im}	0.0, 0	0.0, 0	83.4, 2	70.9, 1	0.0, 2	0.0, 2	−1.9, 1	−16.9, 1
	X-C1	1.93	1.91	2.36	1.95	2.31	2.34	2.27	2.00
N^+	ΔE, n_{im}	0.0, 0	0.0, 0	71.6, 2	65.5, 2	0.0, - [a]	0.0, - [a]	−6.1, 3	−9.8, 3
	X-C1	1.49	1.46	1.66	1.52	1.68	1.59	1.68	1.58
P^+	ΔE, n_{im}	0.0, 0	0.0, 0	74.5, 2	105.5, 1	0.0, 2	0.0, 3	−1.2, 1	−4.1, 2
	X-C1	1.80	1.78	2.14	1.77	2.42	2.43	2.36	1.97
As^+	ΔE, n_{im}	0.0, 0	0.0, 0	64.6, 2	109.7, 2	0.0, 2	0.0, 3	−1.5, 1	−9.7, 1
	X-C1	1.91	1.90	2.42	1.91	2.46	2.50	2.40	2.08

[a] Single point energies, since energy minimization failed to result in stationary points having these geometries at the current level of theory.

sition states with the eigenvectors corresponding to the imaginary frequency representing the X-C bond stretching motion. For X belonging to group 14, and 15 elements, both the **ttX** and **ptX** structures were unstable. On the other hand, for the unsaturated analogues with two valence electrons i.e. $[XC_2H_4]^{2+}$ (X = B^-, Al^-, B^-, Si, and Ge i.e. group 13, and 14 elements), the **ptX**s were minima and their corresponding **ttX**s were higher-order saddle points on the PES. It should be noted that, for X = B^- and Al^-, the corresponding **ttX** structures could not be stabilized.

Similarly, for the spiro-analogues $[XC_4H_4]^{2+}$, the **ttX**s are either transition states or higher-order saddle points on the PES. The **ptX**s for X belonging to group 13 elements i.e. B^- and Ga^- were minimum whereas for Al^-, it was found to be a transition state. For the other analogues of $[XC_4H_4]^{2+}$ (X belonging to group 14 and 15), the **ptX**s were either transition states or higher-order saddle points. On the contrary, for the saturated spirosystems $[XC_4H_8]^{2+}$, both the **ttX**s and **ptX**s were found to be either transition states or higher or saddle points on the PES. The Wiberg bond indices (WBI) were also calculated for the different skeletally substituted systems. The WBI is defined as the amount of electron population overlap between two atoms, and indicates the presence of single, double, or triple bonds. The WBI calculated for most of these systems indicate the presence of stable X-C bonds (see Table 2.2-2.7). However, for some of these systems, the WBI were found to be low, indicating weaker bonding interactions between the groups.

Table 2.2: Wiberg bond indices for cyclopropene analogues calculated at the MP2/cc-pVTZ level of theory. The hyphen, '-' implies that the structures could not be optimized at the current level of theory

	Four valence electrons				Two valence electrons			
	ttX		**ptX**		**ttX**		**ptX**	
X	X-C1	C1-C2	X-C1	C1-C2	X-C1	C1-C2	X-C1	C1-C2
B^-	0.88	1.99	0.80	1.85	-	-	0.61	2.30
Al^-	0.62	2.04	0.54	1.97	0.48	1.03	0.18	2.80
Ga^-	0.68	2.06	0.56	1.97	0.62	1.03	0.20	2.77
C	0.99	1.97	0.44	2.45	-	-	1.03	1.74
Si	0.86	1.98	0.82	1.81	0.33	2.60	0.48	2.51
Ge	0.87	2.02	0.81	1.82	0.32	2.61	0.45	2.52
N^+	0.85	2.00	0.54	1.23	1.09	1.00	1.13	1.27
P^+	1.02	1.93	1.12	1.54	0.94	1.00	0.73	2.11
As^+	0.98	1.99	1.07	1.58	0.89	1.00	0.65	2.20

Table 2.3: Wiberg bond indices for cyclopropane analogues calculated at at MP2/cc-pVTZ level of theory. The hyphen, '-' implies that the structures could not be optimized at the current level of theory

	Four valence electrons				Two valence electrons			
	ttX		**ptX**		**ttX**		**ptX**	
X	X-C1	C1-C2	X-C1	C1-C2	X-C1	C1-C2	X-C1	C1-C2
B^-	0.88	1.00	0.86	1.12	0.37	1.64	0.45	1.59
Al^-	0.63	1.05	0.44	1.08	0.17	1.85	0.19	1.83
Ga^-	0.71	1.05	0.46	1.10	0.18	1.84	0.21	1.80
C	1.00	1.00	0.60	1.33	0.51	1.27	-	-
Si	0.85	1.04	0.63	1.06	0.37	1.58	0.39	1.55
Ge	0.89	1.05	0.26	1.76	0.37	1.58	0.39	1.55
N^+	0.87	1.03	0.57	1.19	-	-	0.59	1.00
P^+	0.98	1.04	0.44	1.48	0.43	1.15	0.45	1.16
As^+	0.96	1.06	0.43	1.51	0.45	1.20	0.47	1.20

Table 2.4: Wiberg bond indices for spiropentadiene derivatives (X with four valence electrons) at the MP2/cc-pVTZ level of theory

	Four valence electrons							
	ttX				**ptX**			
X	X-C1	X-C3	C1-C2	C3-C4	X-C1	X-C3	C1-C2	C3-C4
B^-	0.86	0.86	1.93	1.93	0.81	0.81	1.87	1.87
Al^-	0.60	0.60	2.00	2.00	0.57	0.57	1.98	1.98
Ga^-	0.65	0.65	2.03	2.03	0.59	0.59	2.00	2.00
C	0.98	0.98	1.89	1.89	0.98	0.98	1.69	1.69
Si	0.83	0.83	1.92	1.92	0.80	0.80	1.86	1.86
Ge	0.84	0.84	1.97	1.97	0.79	0.79	1.90	1.90
N^+	0.87	0.87	1.92	1.92	0.69	0.69	2.07	2.07
P^+	0.99	0.99	1.84	1.84	0.99	0.99	1.71	1.71
As^+	0.97	0.97	1.91	1.91	0.95	0.95	1.77	1.77

Table 2.5: Wiberg bond indices for spiropentadiene analogues (X having two valence electrons) at the MP2/cc-pVTZ level of theory. The hyphen, '-' implies that the structures could not be optimized at the current level of theory

	Two valence electrons							
	ttX				**ptX**			
X	X-C1	X-C3	C1-C2	C3-C4	X-C1	X-C3	C1-C2	C3-C4
B^-	0.41	1.29	1.50	2.51	0.84	0.84	2.00	2.00
Al^-	0.60	0.86	0.22	1.86	0.60	0.60	2.25	2.25
Ga^-	-	-	-	-	0.65	0.65	2.21	2.21
C	0.52	1.46	2.23	1.23	0.96	0.96	1.77	1.77
Si	0.40	1.19	2.52	1.63	0.80	0.80	2.08	2.08
Ge	0.40	1.19	2.50	1.67	0.80	0.80	2.08	2.08
N^+	0.37	1.36	2.05	1.09	0.87	0.87	1.57	1.57
P^+	0.51	1.43	2.22	1.33	0.93	0.93	1.88	1.88
As^+	0.48	1.38	2.23	1.44	0.88	0.88	1.93	1.93

Table 2.6: Wiberg bond indices for spiropentane analogues (X with four valence electrons) at th MP2/cc-pVTZ level of theory

	Four valence electrons							
	ttX				**ptX**			
X	X-C1	X-C3	C1-C2	C3-C4	X-C1	X-C3	C1-C2	C3-C4
B^-	0.89	0.89	0.98	0.98	0.66	0.66	1.05	1.05
Al^-	0.60	0.60	1.04	1.04	0.50	0.50	1.06	1.06
Ga^-	0.69	0.69	1.04	1.04	0.50	0.50	1.05	1.05
C	0.99	0.99	0.98	0.98	0.78	0.78	1.12	1.12
Si	0.84	0.84	1.01	1.01	0.65	0.65	1.04	1.04
Ge	0.88	0.88	1.02	1.02	0.66	0.66	1.06	1.06
N^+	0.88	0.88	1.00	1.00	0.71	0.71	1.06	1.06
P^+	0.99	0.99	0.99	0.99	0.80	0.80	1.03	1.03
As^+	0.98	0.98	1.01	1.01	0.76	0.76	1.05	1.05

Table 2.7: Wiberg bond index for spiropentane analogues (X with two valence electrons) at the MP2/cc-pVTZ level of theory. The hyphen, '-' implies that the structures could not be optimized at the current level of theory

	Two valence electrons							
	ttX				**ptX**			
X	X-C1	X-C3	C1-C2	C3-C4	X-C1	X-C3	C1-C2	C3-C4
B^-	-	-	-	-	0.71	0.71	1.20	1.20
Al^-	0.21	0.78	1.80	1.01	0.56	0.56	1.30	1.30
Ga^-	0.24	0.85	1.76	1.11	0.60	0.60	1.26	1.26
C	0.47	1.17	1.29	0.91	0.81	0.81	1.12	1.12
Si	0.36	0.97	1.55	0.96	0.70	0.70	1.21	1.21
Ge	0.37	0.97	1.52	0.98	0.71	0.71	1.19	1.19
N^+	-	-	-	-	0.69	0.69	1.04	1.04
P^+	0.39	1.06	1.21	0.92	0.71	0.71	1.12	1.12
As^+	0.40	0.97	1.21	0.97	0.68	0.68	1.12	1.12

In addition, we found multiple systems where either the **ptX** is a transition state that lead to interconversion between two **ttX** isomers or vice-versa via rotation of the two planes about the central atom, without any X-C bond breaking. This phenomenon is termed as stereomutation and the systems showing such events are discussed below.

2.3.3 Stereomutation in Model Systems with Heteroatom Substitution

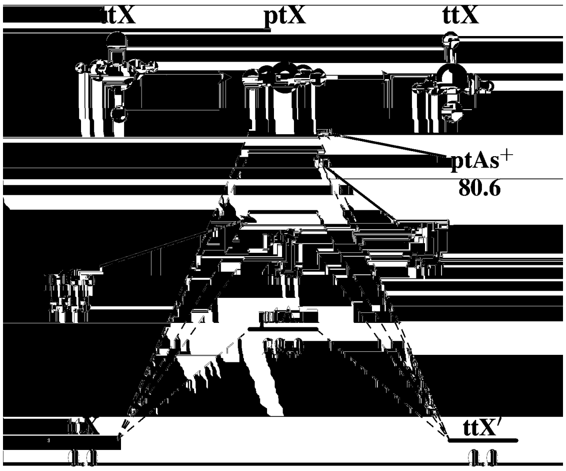

Figure 2.4: Potential energy profile for stereomutation in XC_2H_4 analogues. The energies are reported in kcal mol^{-1}.

Several systems showing stereomutation were identified from the above model systems studied. The possible stereomutation pathways in these systems were investigated by performing the IRC calculations. The IRC was done on either sides of the **ptX** or **ttX** transition states to connect to the respective minima by following the normal mode eigenvector corresponding to the imaginary frequency. The angle (ϕ) between the two planes formed by the two three-membered rings around the central atom (X) changes from 90° to 0° on going from the tetrahedral to the planar isomer respectively. The potential energy profiles for XC_2H_4 systems showing stereomutation is given in Figure 2.4. The stereomutation barriers for X = Al$^-$, Si, Ge, P$^+$, and As$^+$ were found to be 29.0, 49.5, 59.6, 75.2, and 80.6 kcal mol^{-1} respectively.

Interestingly, for the saturated analogues of cyclopropene with two valence electrons i.e. $[XC_2H_6]^{2+}$, the stereomutation occurs via **ttX** being the transition state i.e. **ptX** $\rightarrow$ **ttX** $\rightarrow$ **ptX**. Here, the stereomutation events were found only for systems where X belonged to group 13 elements i.e. X = B$^-$, Al$^-$, and Ga$^-$ (Figure 2.5).

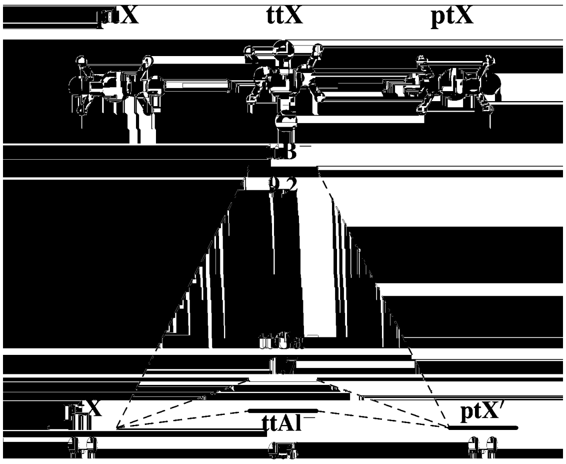

Figure 2.5: Potential energy profile for stereomutation in $[XC_2H_6]^{2+}$ analogues. The energies are reported in kcal mol^{-1}.

The spiropentadiene and spiropentane derivatives showed similar features. The **ptX** for these systems were found to be transition states corresponding to stereomutation and the **ttX** were minimum on the PES (Figure 2.6). We also found that the stereomutation barriers increase on moving along the period and down the group for the model systems.

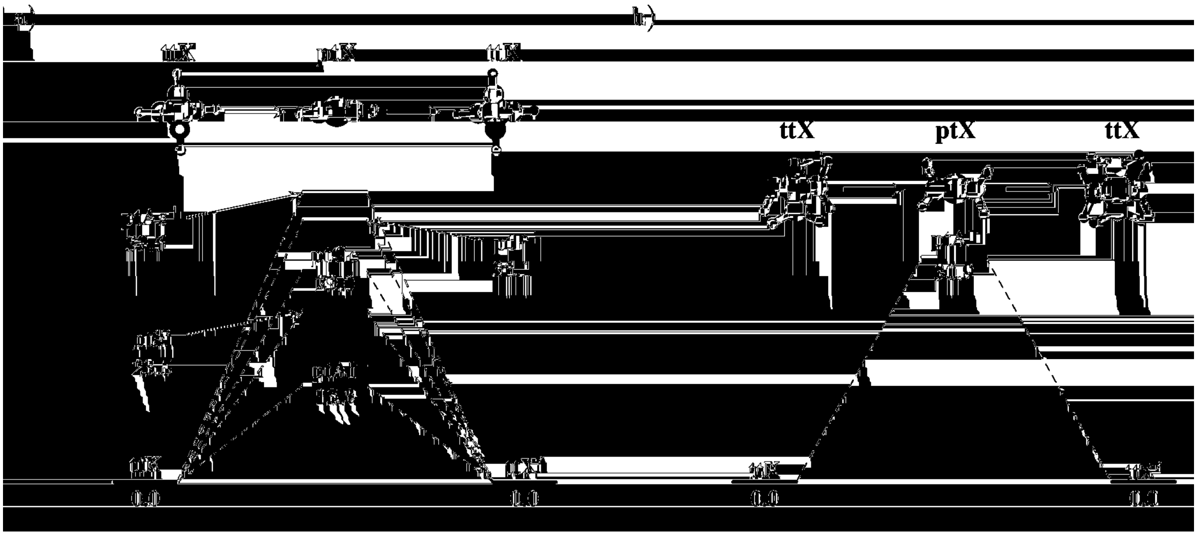

Figure 2.6: Potential energy profile for stereomutation in (a) $[XC_4H_4]$ analogues and (b) $[XC_4H_8]$ where X = Al$^-$. The energies are reported in kcal mol^{-1}.

2.4 Summary and Conclusions

In the present study, we have used different electronic and steric factors, proposed in literature to stabilize model planar tetracoordinated systems. We find that introducing a combination of three-membered rings, heteroatom substitution, removal of the lone pair of electrons and π electron clouds to the system helps in the stabilization of **ptX**. We have identified stable planar tetracoordinated systems by substituting the central atom with various valence isoelectronic species (with respect to carbon) from group 13, 14, and 15 elements. We have also demonstrated systems where stereomutation between two tetrahedral systems is possible via a **ptX** and vice-versa.

CHAPTER 3

TRANSITION BETWEEN [*R*]- AND [*S*]- STEREOISOMERS WITHOUT BOND BREAKING

3.1 Introduction

The independent discovery of the tetrahedral geometry of a carbon by van't Hoff[17] and Le Bel[18] has been a cornerstone in chemistry. This paved a way for understanding the structural properties of organic molecules long before any techniques to characterize molecules were discovered e.g. X-ray analysis. The four groups attached to the tetrahedral carbon are aligned towards the corner of a regular tetrahedron. Thus, a molecule having a chiral center (i.e. four different groups attached to the central atom) leads to the generation of two non-superimposable mirror images. These non-superimposable mirror images of a molecule are termed as enantiomers. To determine the proper descriptor of a chiral center, the Cahn, Ingold, and Prelog (CIP) rules are applied and the configurational descriptors *R* (in Latin *rectus* means right) and *S* (in Latin *sinister* means left) are assigned to the enantiomers.[78]

The interconversion between two enantiomers is always thought to be possible via a C-X bond breaking, where X is any group attached to the chiral center. The classic S_N2 reaction serves as a perfect example for the inversion of configuration at a chiral center. For simplicity, let us consider the incoming nucleophile and the leaving group for the reaction to be same i.e. X^- (Figure 3.1). If the priority sequence of the groups attached to the central carbon atom are in the order D>E>F>X, then according to the CIP rules, the reaction leads to the inversion of configuration at the chiral center from *S* to *R*. This inversion of configuration is termed as the Walden inversion and it occurs via a trigonal bipyramidal transition state.[79]

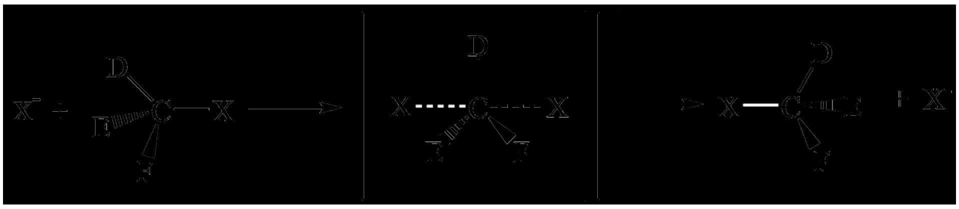

Figure 3.1: Inversion of configuration at the chiral center during a S_N2 reaction.

An interesting question to ask here: is it possible to have an interconversion between two enantiomers without any C-X bond breaking? This question takes us back in 1965 when Wynberg and coworkers experimentally observed that butylethylhexylpropylmethane, a molecule having a chiral center, is optically inactive. However, they ruled out the possible interconversion between the two stereoisomers without any bond breaking (termed as stereomutation).[80] Followed by this experimental observation, in 1968 Monkhorst proposed two different pathways for the isomerization between enantiomers without any bond breaking.[71] To explain these pathways, let us consider the molecule with chiral center bonded to four different groups D, E, F, and X as discussed above. This molecule can hence exist in two enantiomeric forms namely the *R* and *S* isomers.

1. The first pathway involves the interconversion between the two tetrahedral isomers via a planar tetracoordinated center (**ptc**). This planar geometry can be achieved by a clockwise (/anticlockwise) rotation about the axis passing through the central atom (for the *R* isomer). In the planar structure, the four atoms attached to the chiral center occupy

the four corners of the diagonal of a cube. This configuration has a plane of symmetry. Further rotation about the axis leads to the formation of the other enantiomer, *S* (Figure 3.2).

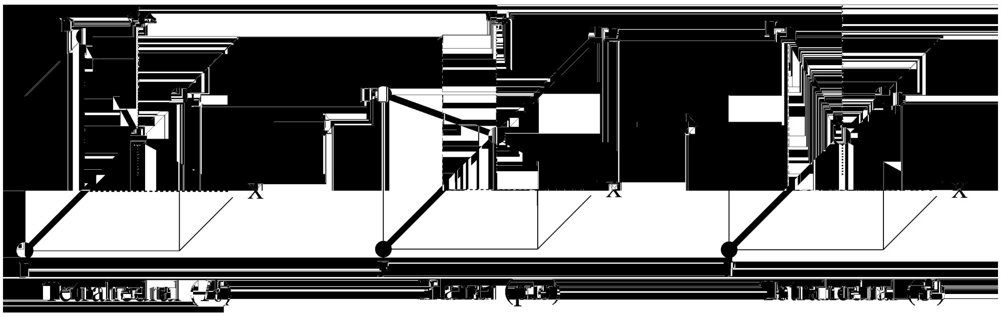

Figure 3.2: Stereomutation via a planar structure.

2. The second pathway involves the formation of a pyramidal configuration, with the central atom on top of it. This configuration can be achieved by placing the four atoms attached to the central carbon at the four corners of the face of a cube, with the central atom being at the top, hence forming a pyramidal structure. Further movement of the other two groups (C and D) on the opposite face of the cube, leads to the formation of the enantiomer, *S* (Figure 3.3).

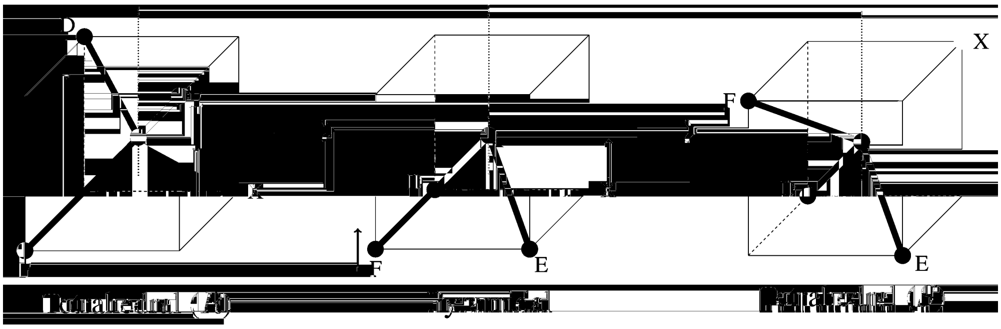

Figure 3.3: Stereomutation via a pyramidal structure.

Monkhorst performed LCAO-SCF calculations and suggested that the planar configuration for methane is about 250 kcal mol^{-1} higher in energy as compared to its tetrahedral structure.

Moreover, he found that the **ptc** is a higher-order saddle point on the potential energy surface and concluded that, "racemization via a **ptc** is impossible and that it would require $\sim$ 2.5 times higher energy as compared to the C-C bond breaking".[71] Since then, studies are being carried out to make the racemization process via a **ptc**, thermally accessible.

Hoffmann and coworkers[19] investigated the electronic structure of planar methane to explore means by which the **ptc** could be stabilized and hence can act as a transition state for viable stereomutation. They could not identify any stable molecule, but proposed various strategies by which the **ptc** could be stabilized. By using these techniques, over the years various experimental realizations as well as theoretical modellings have shown the existence of planar tetracoordinated carbon and planar tetracoordinated structures with various valence isoelectronic species such as B^-, N^+, Si, Al^-, P^+.[41,42,58,81–85] However, the racemization via a **ptc** was always found to be impossible due to high energy barriers for racemization or the tetrahedral tetracoordinated centres could not be stabilized for a particular system. In 2021, Cao and coworkers computationally designed a series of stable aromatic **ptSi** compounds, in which the central Si atom is surrounded by four conjugated rings. They also performed Born Oppenheimer Molecular Dynamics (BOMD) simulations for a range of temperature and found that the molecule is quite stable even at higher temperatures.[86]

In this chapter, we propose model system [XC_4H_4] (with the central atom X substituted with various valence isoelectronic species of carbon, from group 13, 14, and 15 elements) in which the planar tetracoordinated structure acts as a transition state/intermediate for the viable interconversion between two tetrahedral isomers. *Ab initio* classical dynamics simulations further reveal that the interconversion between the two tetrahedral structures is possible via a planar tetracoordinated center and bond-breaking pathways.

3.2 Methodology

3.2.1 Quantum Mechanical Calculations

The stationary points on the PES were identified and the normal mode frequency calculations were performed at the MP2/cc-pVTZ[67,87] level of theory. The number of imaginary frequencies obtained from the normal mode analysis were used to characterize the stationary points as minima, transition state, or other higher order saddle point on the PES. The intrinsic reaction coordinate[68], was followed on either side of the transition state to connect to the respective intermediates. The calculations were performed using Gaussian16[70], NWChem[88], and Molpro[89] software. Single point energies were calculated at the CCSD(T)/cc-pVTZ//MP2/cc-pVTZ level of theory.[90] The MP2/cc-pVTZ values were in close agreement with that obtained from CCSD(T)/cc-pVTZ level of theory. Hence, the data presented here are obtained at MP2/cc-pVTZ level of theory unless stated otherwise. The potential energy surfaces were generated by performing partial optimization and scanning the important geometrical parameters as discussed in the next section.

To account for the static correlation in the isomerization pathways, CASSCF(n,m)/cc-pVTZ//MP2/cc-pVTZ calculations were performed using two active spaces (8,8) and (14,14). The (8,8) active space consists of the four X-C σ and σ^* orbitals and the corresponding eight electrons in the X-C σ bonding orbitals. The (14,14) active space consists of the four X-C σ bonds, two C(sp)-C(sp) π-bonds and one C(sp)-C(sp) σ-bond and their corresponding anti bonding orbitals. In addition, CASPT2(8,8)/cc-pVTZ//MP2/cc-pVTZ calculations were also performed to account for the dynamic correlation of the systems.

3.2.2 *Ab initio* Classical Trajectory Simulations

The *ab initio* classical trajectory simulations were performed using VENUS/NWChem programs[91,92] at the MP2/cc-pVTZ level of theory. For X = Al^-, Si, and P^+, 50 trajectories each were initiated from the classical minima of the reactants with a fixed E_{total} of 40.92, 40.79, and 42.95 kcal mol^{-1} respectively, using microcanonical normal mode sampling technique.[14] The E_{total} approximately corresponds to the sum of average vibrational, rotational, and translational energies of the molecule by assuming a Boltzman distribution of states at 300 K. The trajectories were integrated for a total of 2 ps using the velocity-Verlet algorithm[93] with the necessary forces computed on-the-fly at the MP2/cc-pVTZ level of theory.

For the heavier congeners i.e. X = Ga$^-$, Ge, and As$^+$, a set of 30 trajectories each were initiated from the classical minimum using Boltzmann sampling at 300 K. The trajectories were integrated for a total time of 1 ps each at the MP2/cc-pVTZ level of theory.

3.3 Results and Discussions

3.3.1 Structure and Energetics

Motivated by the design of a stable planar tetracoordinated carbon center in a spiroconjugated compound $C(C)_2(CH_2)_2$ by Priyakumar *et. al.*[57], we have devised model systems by replacing the central atom with various valence isoelectronic species from the second, third, and fourth row of the periodic table i.e. X = B$^-$, N$^+$, Al$^-$, Si, P$^+$, Ga$^-$, Ge, and As$^+$. The schematic representation of the model system is given in Figure 3.4. When the central spiro carbon atom is replaced with valence isoelectronic elements from the second period, X = B$^-$, and N$^+$, the **ptc** is found to be mimimum on the PES and more stable as compared to the tetrahedral isomers.

For X = B$^-$, the tetrahedral tetracoordinated center (**ttc**) is a second-order saddle point and is 5.3 kcal mol^{-1} higher in energy as compared to the **ptc**. The eigen vectors representing the two imaginary frequencies correspond to the B-C(*sp*) bond stretching and the rotation about the planes containing the two three membered rings. For X = C, the **ttc** is a transition state and the eigen vector in this case corresponds to the C-C(*sp*) bond stretching motion. Interestingly, a)

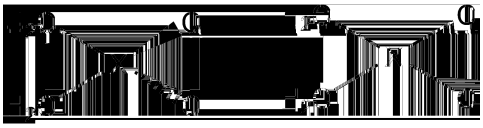

b)

B^-	C	N^+
Al^-	Si	P^+
Ga^-	Ge	As^+

Figure 3.4: (a) Schematic representation of the **ttc** and **ptc** structures for the model systems used in this study, (b) Different valence isoelectronic elements used to replace the central spiro carbon atom in the model skeleton $X(C)_2(CH_2)_2$

Table 3.1: Charaterization of **ttX** and **ptX** geometries for X = group 13, 14, and 15 elements. The n_{imag} represents the number of imaginary frequencies for the corresponding stationary point. Energies of **ptX** relative to **ttX** with and without zero point energy corrections i.e. ΔE_{ZPE}, ΔE respectively are given in kcal mol^{-1}, q (X) represents the natural population analysis (NPA) charges on the central atom, X

	ttX				**ptX**			
X	n_{imag}	ΔE	ΔE_{ZPE}	q (X)	n_{imag}	ΔE	ΔE_{ZPE}	q (X)
B^-	2	0.0	0.0	0.71	0	−5.25	−4.48	0.49
Al^-	0	0.0	0.0	1.67	1	3.66	3.30	1.62
Ga^-	0	0.0	0.0	1.50	1	0.37	0.42	1.43
C	1	0.0	0.0	0.29	0	−16.32	−16.90	−0.10
Si	0	0.0	0.0	1.87	1	4.75	4.18	1.74
Ge	0	0.0	0.0	1.75	0	−0.42	−0.43	1.60
N^+	0	0.0	0.0	−0.13	0	−25.45	−32.96	−0.62
P^+	0	0.0	0.0	1.76	0	5.62	3.87	1.44
As^+	0	0.0	0.0	1.80	0	−2.56	−3.24	1.46

for X = N^+, both the **ttc** and **ptc** are minimum on the PES, the **ptc** being more stable by ∼ 25 kcal mol^{-1} as compared to the **ttc** isomer (Table 3.1).

Replacing the central spiro carbon atom with the valence isoelectronic elements from third period shows interesting features. Geometry optimization of the tetrahedral and planar tetracoordinated structures reveal that all the **ttc** structures are minimum on the PES and lie ∼ 3.5 - 5 kcal mol^{-1} lower in energy than the corresponding **ptc** structures. For X = Al^- and Si, the **ptc** are found to be transition states whereas for X = P^+, the **ptc** is a minimum on the PES.

For X = Ge, and As^+, the **ptc** is stabilized by -0.42 and -2.56 kcal mol^{-1} respectively as compared to the **ttc** isomer and are stable minima on the PES. Whereas for X = Ga^-, the **ptc** is higher in energy by ~ 0.4 kcal mol^{-1} with respect to the **ttc** and is a transition state on the PES.

3.3.2 Isomerization Reaction Pathways

As discussed, the isomerization between the tetrahedral isomers can occur either via a planar tetracoordinated structure or via the bond breaking pathway. To account for the mechanisms followed during isomerization, the potential energy profiles for the stereomutation and ring-opening pathways were mapped. The stationary points were characterized as minima and transition state (TS) and the IRC was followed on either sides of the TS to connect to the respective intermediates. The coordinate ϕ defined as the angle between the two planes formed by the two three-membered rings gives the best description for stereomutation via a **ptc**. ϕ varies from 90° to 0° on going from **ttX** to **ptX** structure (Figure 3.5). On the other hand, θ defined

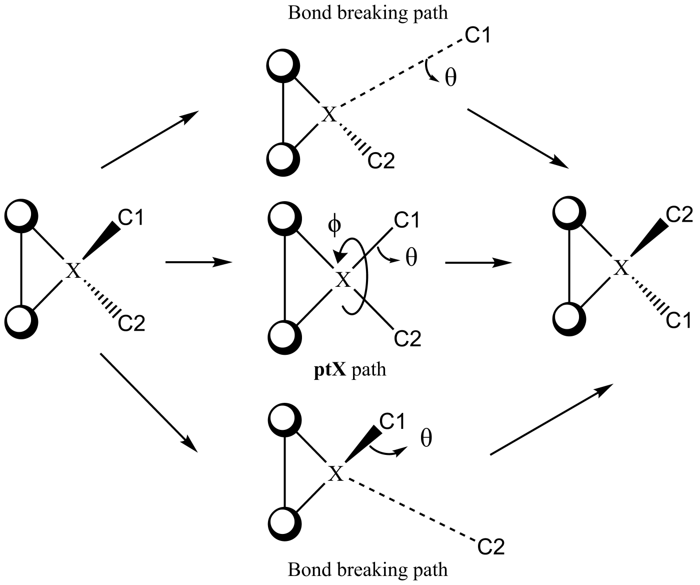

Figure 3.5: Schematic representation of various pathways for the interconversion between two tetrahedral isomers.

as $\angle$XC1C2 describes the bond breaking pathway. θ varies from the equilibrium value, θ_{eq} to θ = 180° or 0° depending on whether X-C2 or X-C1 bond breaking occurs during the reaction respectively.

(i) Valence isoelectronic elements from third period, X = Al$^-$, Si, and P$^+$

The potential energy profile for the interconversion between the two tetrahedral isomers for the spiroconjugated compound $X(C)_2(CH_2)_2$, where X = Al$^-$, Si, and P$^+$ is given in Figure 3.6. The planar tetracoordinated center, **ptX** for X = Al$^-$ and Si are TSs on the PES with a barrier height of 3.7 and 4.8 kcal mol^{-1} respectively. In contrast, for X = P$^+$, the **ptX** is a stable intermediate and is 5.1 kcal mol^{-1} higher in energy with respect to **ttX**. From **ttP**, clockwise variation of ϕ leads to the TS (ϕ = 31.5°) with a barrier of 5.6 kcal mol^{-1}, and further clockwise variation of ϕ yields the planar intermediate **ptP** (ϕ = 0°). The isomer **ttP′** is then formed from **ptP** via further clockwise change in ϕ via a degenerate TS. It should be noted that these systems are not chiral and hence the tetrahedral isomers are differentiated based on the atom indices i.e. **ttX** and **ttX′**. Also, for these systems, the potential energy profile

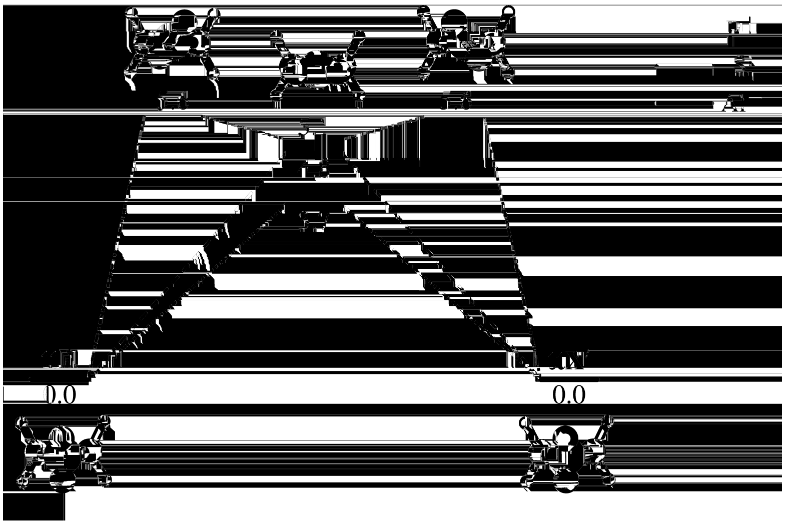

Figure 3.6: Potential energy profile for stereomutation of spiroconjugated compound for $X(C)_2(CH_2)_2$, where X = Al$^-$, Si, and P$^+$.

is invariant to the direction of change in ϕ i.e. both clockwise and anticlockwise variation of ϕ yields isoenergetic PES.

The bond breaking pathways for the interconversion between the isomers **ttX** and **ttX**$'$ were also mapped (Figure 3.7). For X = Al$^-$ and Si, the bond breaking pathways show similar features with barrier heights of 9.0 and 11.3 kcal mol^{-1} respectively. The isomerization occurs via stretching of one of the X-C(*sp*) bond via TS **ts2_X** to form an intermediate **int2_X**. The formation of the X-C(*sp*) bond from **int2_X** via **ts2_X**$'$ leads to the formation of the isomer **ttX**$'$. Figure 3.8 shows the potential energy profile for the bond breaking pathway for X = P$^+$.

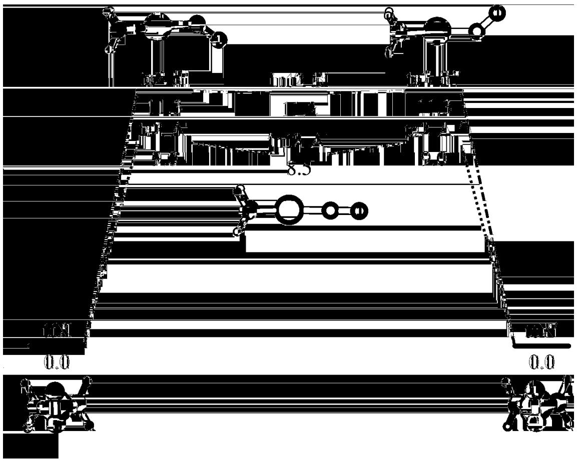

Figure 3.7: Potential energy profile for the ring-opening pathway of spiroconjugated compound X(C)$_2$(CH$_2$)$_2$, where X = Al$^-$ and Si.

The stretching of one of the P-C(*sp*) leads to the formation of an intermediate **int2** via TS **ts2** with a barrier of 5.6 kcal mol^{-1}. Further P-C(*sp*) bond stretching leads to the formation of an isoenergetic intermediate **int2**$'$ via a TS **ts3** with a barrier of 6.1 kcal mol^{-1}. It should be noted that for X = Al$^-$ and Si, the geometry with ∠XC1C2 = 180° was a minima on the PES in contrast to P$^+$ where it is a TS. Formation of the P-C(*sp*) bond again via **ts2**$'$ leads to the isomer **ttP**$'$.

We also performed CASSCF calculations to examine the static correlation effect for X = Si system. The CASSCF energies were found to be in satisfactory agreement with the MP2

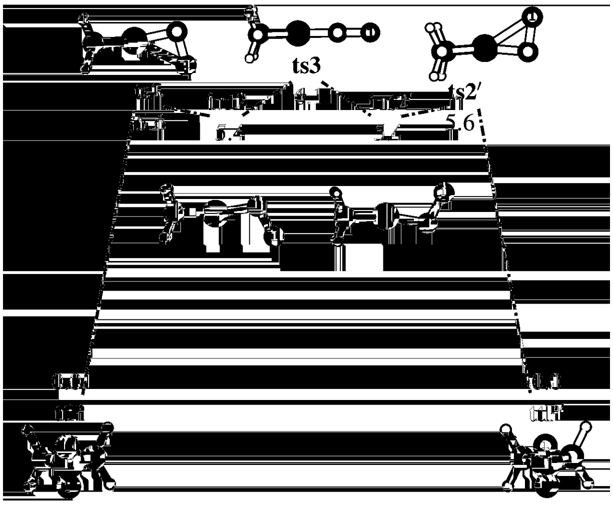

Figure 3.8: Potential energy profile for the ring-opening pathway of spiroconjugated compound $X(C)_2(CH_2)_2$, where $X = P^+$.

Table 3.2: Relative energies of different stationary points for X = Si at MP2, CASSCF(*n*,*m*), and CASPT2 level of theories with cc-pVTZ basis set

Species	MP2	CASSCF(8,8)	CASPT2(8,8)	CASSCF(14,14)
ttX	0.0	0.0	0.0	0.0
ptX	4.8	5.6	6.8	6.1
ts2_X	11.3	8.0	10.7	7.9

values (Table 3.2) and hence, we chose MP2/cc-pVTZ level of theory for further studies. The potential energy surfaces for the three systems were also generated as a function of $\angle XC1C2$, θ and the angle between the planes formed by the two three-membered rings i.e. ϕ by performing a relaxed scan at MP2/cc-pVTZ level of theory (Figure 3.9). The relative barriers for the isomerization at different level of theories and the important geometrical parameters are given in Table 3.3.

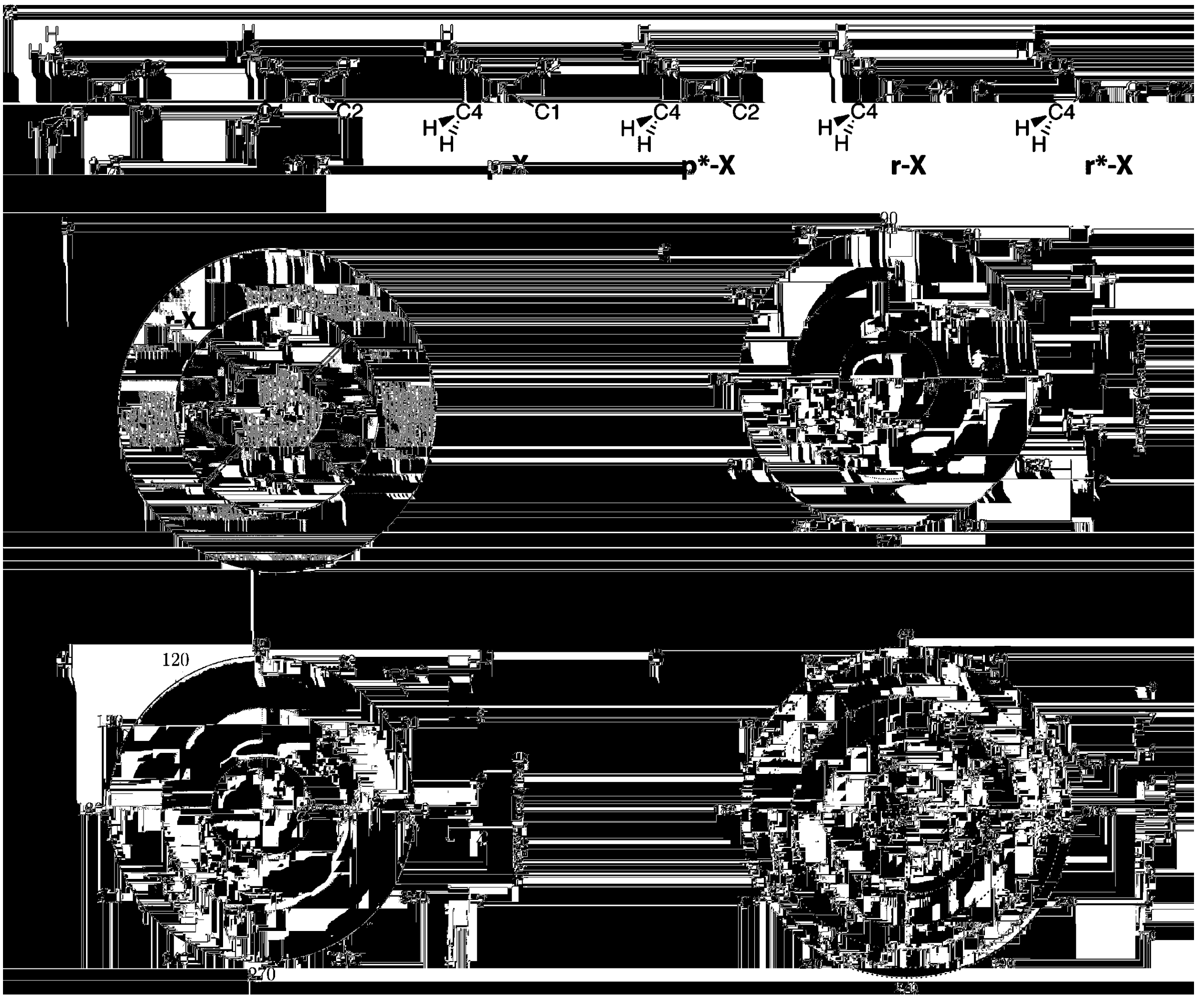

Figure 3.9: (a) Different stationary points obtained, (b) Schematic potential energy surface for $X(C)_2(CH_2)_2$, PES for X = (c) Si, (d) Al^-, and (e) P^+. The radial axis represents the variation of $\angle XC1C2$, θ and the polar axis represents the variation of the angle between the two planes formed by the two three-membered rings i.e. ϕ. A $10(\phi)\times 22(\theta)$ grid was used (for each quadrant) to make the scan surface.

Table 3.3: Relative energies and important geometrical parameters of different stationary points for X = Al^-, Si, and P^+ using MP2 and CCSD(T) methods. The energies, angles and distances are reported in kcal mol^{-1}, °, and Å respectively. **ts**† refers to the transition state leading to the formation of **ptX** from **ttX**

Species	MP2/cc-pVTZ	CCSD(T)/cc-pVTZ^a	ϕ	θ	X-C1	X-C2	C1-C2
X = Al^-							
ttX	0.0	0.0	90.0	71.0	1.96	1.96	1.27
ptX	3.7	3.5	0.0	71.0	1.98	1.98	1.28
ts2_Al	9.0	7.8	90.0	137.6	1.83	2.90	1.27
int2_Al	8.5	7.4	-	180.0	1.83	3.10	1.27
ts2_Al′	9.0	7.8	−90.0	137.6	1.83	2.90	1.27
X = Si							
ttX	0.0	0.0	90.0	69.4	1.82	1.82	1.28
ptX	4.8	4.5	0.0	69.4	1.84	1.84	1.29
ts2_Si	11.3	8.5	90.0	154.3	1.69	2.89	1.28
int2_Si	11.2	8.5	-	180.0	1.69	2.96	1.28
ts2_Si′	11.3	8.5	−90.0	154.3	1.69	2.89	1.28
X = P^+							
ttX	0.0	0.0	90.0	68.1	1.72	1.72	1.28
ptX	5.1	4.5	0.0	67.8	1.76	1.76	1.33
ts†	5.6	4.3	31.5	67.9	1.75	1.75	1.31
ts2	5.6	3.8	90.0	92.9	1.63	2.14	1.31
int2	5.4	1.2	90.0	109.2	1.62	2.40	1.31
ts3	6.1		-	180.0	1.60	2.90	1.31
int2′	5.4	1.2	−90.0	109.2	1.62	2.40	1.31
ts2′	5.6	3.8	−90.0	92.9	1.63	2.14	1.31

^{a} MP2/cc-pVTZ geometries were used in the CCSD(T) calculations.

(ii) Valence isoelectronic elements from fourth period, X = Ga^-, Ge, and As^+

The potential energy profiles for the spiroconjugated model system reveal very low energy barriers for stereomutation for X = Ga^-, Ge, and As^+. For X = As^+ and Ge, both the **ptX** and **ttX** were found to be a minima on the PES. It is interesting to note that the **ptAs** and **ptGe** were 2.6 and 0.4 kcal mol^{-1} stabilized with respect to their **ttAs** and **ttGe** counterparts respectively. However, the **ptGa** was found to be a transition state and was 0.4 kcal mol^{-1} higher in energy than its corresponding **ttX** isomer. For **ptGa**, the IRC lead to the formation

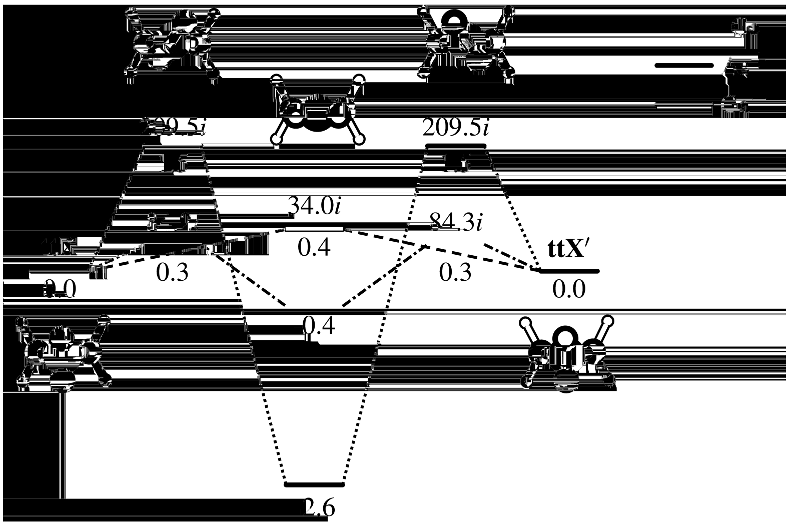

Figure 3.10: Potential energy profile for stereoemutation of model $X(C)_2(CH_2)_2$ systems (X = Ga^-, Ge, and As^+). The relative energies and the imaginary frequencies are given in kcal mol^{-1} and cm^{-1} respectively.

of **ttGa** isomer on either sides. However, for X = As^+ and Ge, as the isomerization occurs via a **ptX** intermediate, the IRC from **ts1** connects the **ttX** and **ptX** isomers (Figure 3.10). It is to be noted that, on going down the group, the energy barriers for stereomutation for the spiroconjugated systems decrease. Hence, the heavier congeners of group 13, 14, and 15 may act as potential candidates for compounds showing isomerization of tetrahedral centres via **ptXs**.

To understand the racemization via X-C(*sp*) bond breaking pathways, the potential energy profiles for the ring-opening pathways were also mapped for the three systems. The ring-opening pathway for X = As^+ shows interesting features. The As-C bond cleavage can occur either directly from **ttAs** or via the **ptAs** isomer, **int1**. The angle between the two planes containing the three membered rings, ϕ is 90° and 0° in **ttAs** and **int1** respectively. The stereomutation of the system from **ttAs** to **int1** occurs via transition state **ts1** ($\phi = -122.4°$) with an energy barrier of 1.5 kcal mol^{-1}. The intermediate **int1** is more stabilized as compared to its tetrahedral isomer **ttAs** by 2.6 kcal mol^{-1}. From **int1**, rotation via ϕ with As-C bond elongation (ring-opening) leads to the formation of **int2** via transition state **ts2** with a barrier of 1.1

kcal mol^{-1}. Further As-C bond stretching from **int2** forms **int2$'$** via transition state **ts4** with a barrier of 1.2 kcal mol^{-1}. The eigen vectors corresponding to the imaginary frequency of **ts4** connects **int2** and **int2$'$** on either sides. **int2$'$** on further As-C bond contraction and rotation via ϕ leads to the formation of **int1$'$** which hence forms the stereoisomer **ttAs$'$** via transition state **ts1$'$** (Figure 3.11).

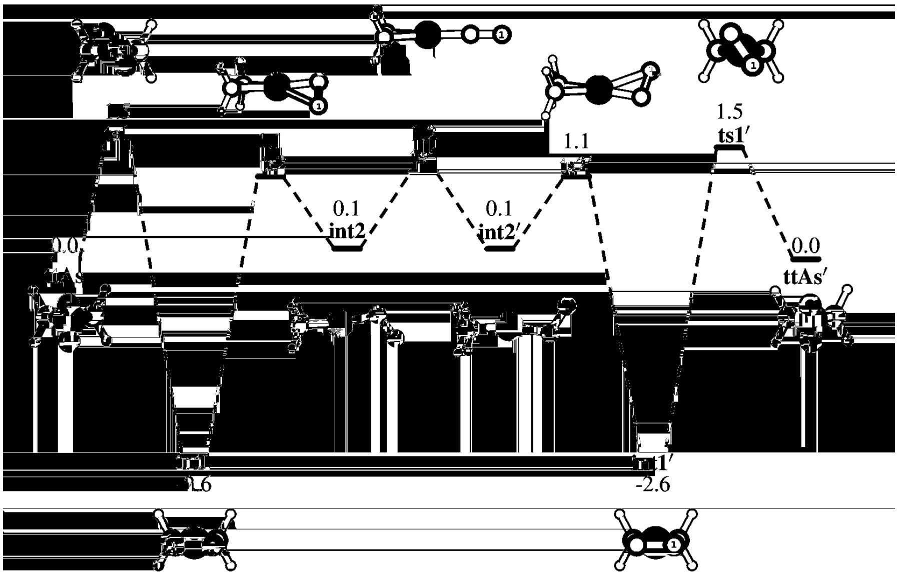

Figure 3.11: Ring-opening pathway for the interconversion between **ttAs** and **ttAs$'$** via the planar intermediate, **int1**. The relative energies for different stationary points are given in kcal mol^{-1}.

It should be noted that, the isomerization can also occur directly from the **ttAs^{+}** isomer via the ring-opening pathway. The As-C bond elongation from **ttAs** leads to the formation of intermediate **int2** via transition state **ts3** with a barrier of 1.8 kcal mol^{-1}. It is interesting to note that **ttAs** and **int2** are nearly degenerate. Further stretching of As-C bond leads to the formation **int2$'$** via **ts4**. **ts4** was found to have $\angle$AsC1C2 $\sim$180°. The formation of the **ttAs$'$** occurs from **int2$'$** via **ts3$'$** by overcoming a barrier of 1.8 kcal mol^{-1} (Figure 3.12). The barriers for the ring-opening pathways via **ttAs** and **ptAs** were $\sim$ 1-2 kcal mol^{-1} and hence comparable to the stereomutation pathway ($\sim$ 1.5 kcal mol^{-1}). This may indicate the possible competition between the two pathways for this system.

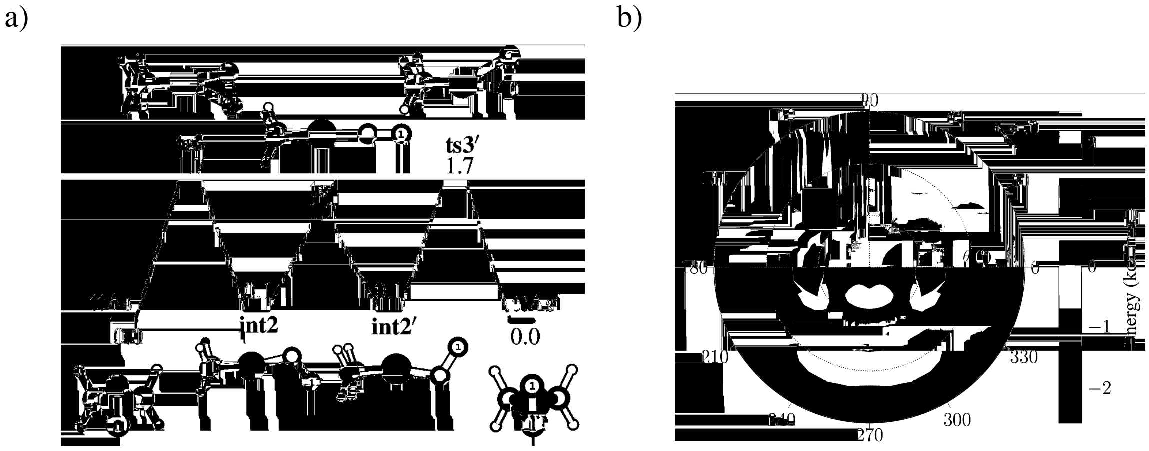
a)
b)
ts3′
1.7
int2
int2′
0.0
90
180
210
240
270
300
330
0
−1
−2
Energy (kcal

Figure 3.12: (a) Ring-opening pathway for the interconversion between **ttAs** and **ttAs**′. The relative energies for different stationary points are given in kcal mol^{-1} and (b) PES scan obtained for X = As^+ by performing a relaxed scan as a function of ϕ and θ.

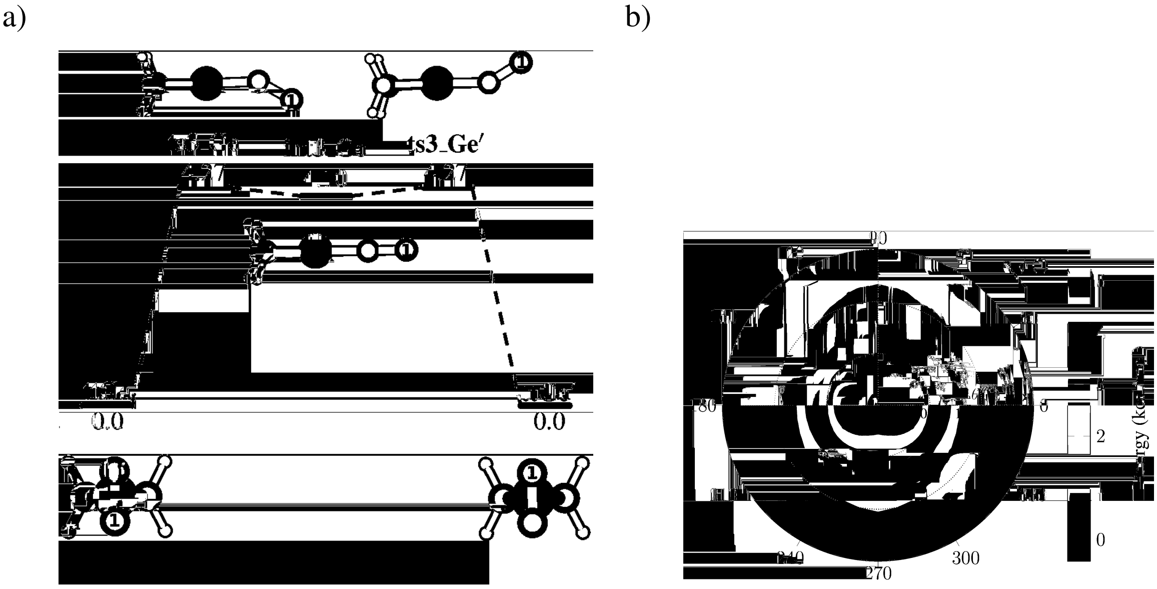
a)
b)
ts3_Ge′
0.0
0.0
90
180
240
270
300
2
0
Energy (kcal

Figure 3.13: (a) Ring-opening pathway for the isomerization of **ttGe** to **ttGe**′ and (b) potential energy surface scan for [GeC_4H_4]. The relative energies for different stationary points are given in kcal mol^{-1}.

The ring-opening pathways for X = Ge and Ga^- systems were found to show similar characteristics. In both the systems, the ring-opening occurs via **ttX**. The X-C bond stretching in **ttX** leads to the formation of an intermediate **int3_X** via **ts3_X** (Figures 3.13-3.14). In contrast to As^+ where the structure with ∠XC1C2 = 180° correspond to a transition state (**ts4**), for Ge

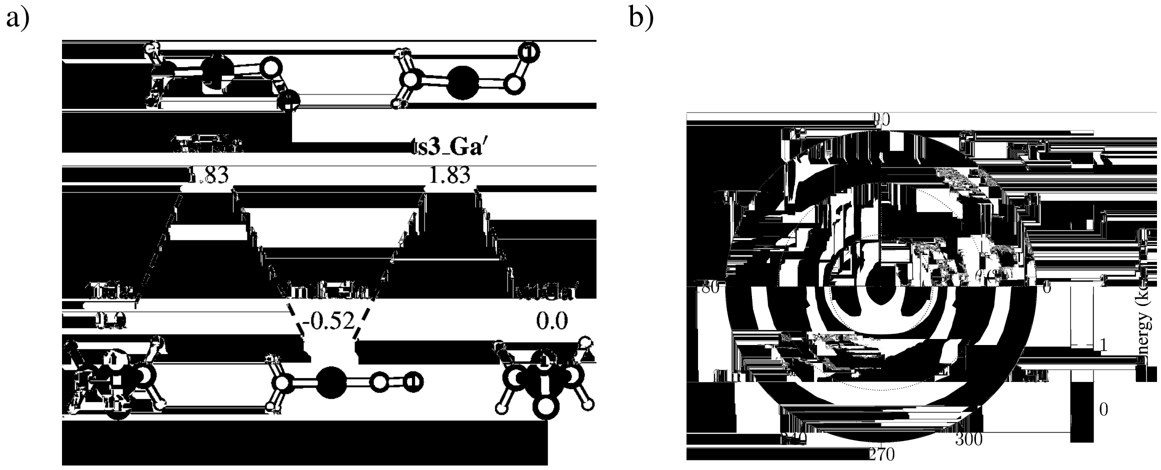

Figure 3.14: (a) Ring-opening pathway for the isomerization of **ttGa** to **ttGa′** and (b) potential energy surface scan for $[GaC_4H_4]^-$. The relative energies for different stationary points are given in kcal mol^{-1}.

and Ga^-, **int_X** was found to be minima on the PES. Moreover, the X-C bond was found to be more elongated in **ts3_Ge** (∠GeC1C2 = 148.6°, r_{GeC1} = 2.92 Å) as compared to **ts3_Ga** (∠GaC1C2 = 113.9°, r_{GaC1} = 2.63 Å). Also, the ring-opening barriers were found to be 1.8 and 4.3 kcal mol^{-1} for X = Ga^- and Ge respectively. The relative energies for the stationary points at different level of theories and the important geometrical parameters are given in Table 3.4.

3.3.3 Dynamics of the Isomerization

To understand the various reaction mechanisms followed during the interconversion of **ttX** and **ttX′**, we studied the time evolution of the systems using *ab initio* classical dynamics simulations. A set of 50 trajectories each were initiated for X = Al^-, Si, and P^+. Out of the total trajectories initiated, 28, 5, and 35 trajectories were found to be reactive for X = Al^-, Si, and P^+ respectively i.e. they exhibited isomerization within the integration time. These trajectories either showed stereomutation via the **ptX** or via the ring-opening pathway. Stereomutation via **ptX** was observed in 27/28, 4/5, and 4/35 reactive trajectories for X = Al^-, Si, and P^+ respectively. The internal coordinates ϕ and θ were followed as a function of time to understand the different pathways followed during the dynamical simulations. In addition, we

Table 3.4: Relative energies and important geometrical parameters of different stationary points for X = Ga^-, Ge, and As^+ using MP2 and CCSD(T) methods. The energies, angles and distances are reported in kcal mol^{-1}, °, and Å respectively. The transition state **ts**† leads to the formation of **ptX** from **ttX**.

Species	MP2/cc-pVTZ	CCSD(T)/cc-pVTZ[a]	ϕ	θ	X-C1	X-C2	C1-C2
X = Ga^-							
ttX	0.0	0.0	90.0	71.4	2.00	2.00	1.28
ptX	0.4	0.5	0.0	71.2	2.01	2.01	1.30
ts3_Ga	1.8	0.8	90.0	113.8	1.84	2.63	1.28
int3_Ga	−0.5	−1.2	-	180.0	1.83	3.10	1.27
ts3_Ga′	1.8	0.8	−90.0	113.8	1.84	2.63	1.28
X = Ge							
ttX	0.0	0.0	90.0	70.4	1.91	1.91	1.28
ptX	−0.4	−0.2	0.0	70.1	1.92	1.92	1.31
ts†	0.3	0.1	−126.2	70.3	1.92	1.92	1.29
ts3_Ge	4.3	2.0	90.0	148.6	1.76	2.92	1.28
int3_Ge	4.1	2.0	-	180.0	1.75	3.03	1.28
ts3_Ge′	4.3	2.0	−90.0	148.6	1.76	2.92	1.28
X = As^+							
ttX	0.0	0.0	90.0	69.7	1.85	1.85	1.28
ptX	−2.6	−2.3	0.0	69.1	1.88	1.88	1.35
ts†	1.5	0.4	−122.4	69.7	1.86	1.86	1.29
ts2	1.1	−0.5	−135.8	92.5	1.75	2.24	1.32
int2	0.1	−3.6	90.0	113.7	1.72	2.55	1.31
ts3	1.7	1.6	90.0	84.7	1.76	2.09	1.30
ts4	1.2	−3.8	-	180.0	1.71	3.01	1.30
int2′	0.1	−3.6	−90.0	113.7	1.72	2.55	1.31
ts2′	1.1	−0.5	−45.8	92.6	1.75	2.24	1.32
ts3′	1.7	1.6	−90.0	84.7	1.76	2.09	1.30

[a] CCSD(T)/cc-pVTZ//MP2/cc-pVTZ level of theory

also found trajectories showing multiple stereomutation, ring-opening, and recrossing events during the total integration time. Sample trajectories for X = Al^-, Si, and P^+ systems showing stereomutation events are shown in Figure 3.15.

It is interesting to note that for X = P^+, although the barriers for stereomutation and ring-opening pathways are similar ($\sim$ 5.6 and 6.1 kcal mol^{-1} respectively), 31 trajectories followed the latter whereas only 4 trajectories followed the former pathway. This clearly indicates the

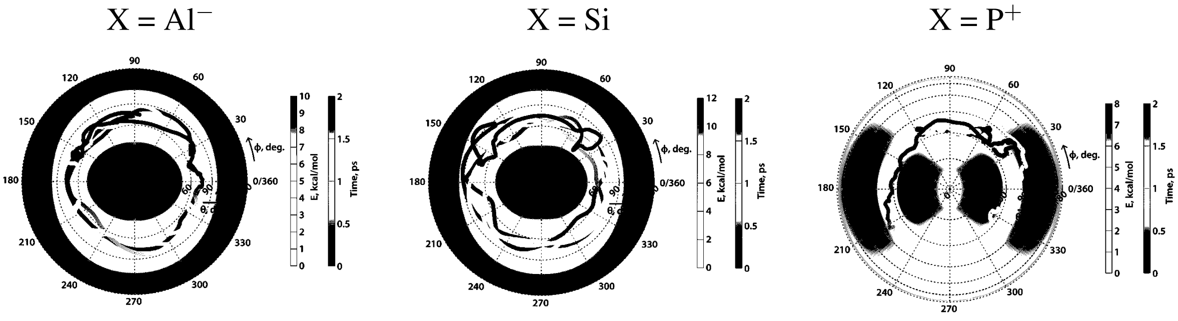

Figure 3.15: Representative trajectories showing stereomutation for systems with X = Al$^-$, Si, and P$^+$ respectively. The trajectories are plotted on the relaxed PES computed at MP2/cc-pVTZ level of theory. The radial axis represents $\angle$XC1C2 (θ) and the polar axis represents the variation of ϕ. The color coding represents the time evolution of the system.

dynamical nature of the system and the role of intramolecular vibrational energy redistribution in the dynamics. We also calculated the Rice-Ramsperger-Kassel-Marcus (RRKM) lifetimes for the stereomutation and ring-opening pathways. The RRKM rate constant and lifetime is given as,

$$k(E) = \frac{G(E - E^\dagger)}{h\rho(E)} \tag{3.1}$$

$$\tau_{\text{RRKM}} = \frac{1}{k(E)} \tag{3.2}$$

where, $G(E - E^\dagger)$ is the sum of states at the transition state, $\rho(E)$ is the density of states at the reactant, E is the total energy available to the system, $E^\dagger$ is the energy barrier for the reaction, and h is the Planck's constant. For X = P$^+$, the lifetimes for the pathways were found to be 0.25 ps and 0.10 ps respectively. For the X = Si and Al$^-$ systems, the ring-opening lifetimes were found to be longer compared to the stereomutation lifetimes due to the higher energy barriers for the ring-opening process. However, it should be noted that the dynamics of the isomerization is non-RRKM with several trajectories exhibiting recrossing events.

Similarly, for X = Ga$^-$, Ge, and As$^+$, set of 30 trajectories each were initiated at the reactant region each using Boltzmann sampling techniques at 300 K. 5/30, 23/30, and 10/30 trajectories each were found to show stereomutation as the first event for X = Ga$^-$, Ge, and As$^+$ systems respectively. However, 5/30 and 11/30 trajectories showed ring-opening during

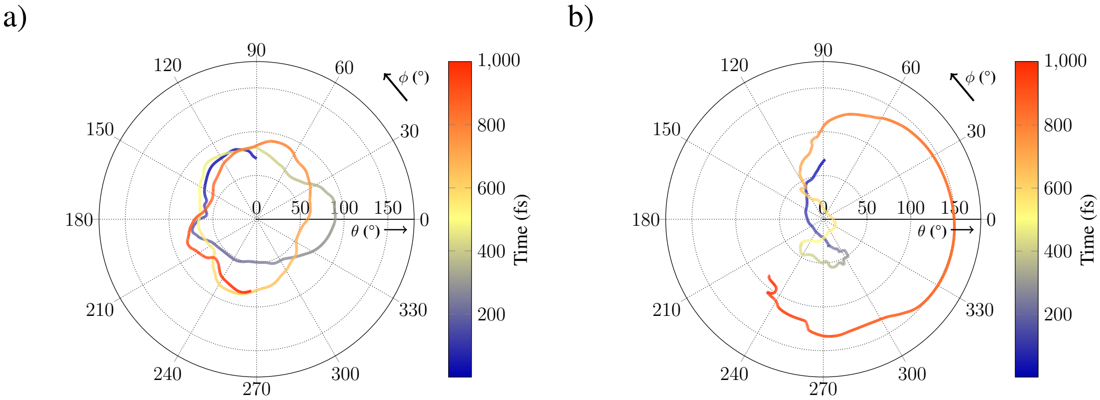

Figure 3.16: Sample trajectories showing (a) stereomutation via **ptGe** and (b) ring-opening pathway for **ttAs**. The colorbar shows the evolution of the trajectory with time.

stereomutation as the first event for X = Ga^- and As^+ respectively. Sample trajectories showing stereomutation and ring-opening pathways are shown in Figure 3.16. It is interesting to note that none of the 30 trajectories followed the ring-opening pathway of stereomutation for X = Ge system within the total integration time of 1 ps. This can be attributed to the high barrier of bond breaking pathway ($\sim$ 4.3 kcal mol^{-1}) as compared to stereomutation pathway ($\sim$ 0.3 kcal mol^{-1}) for this system. However, it should be noted that the ring-opening pathways can be observed on integrating the trajectories for a longer period of time. In contrast, since the barriers for the stereomutation and bond breaking pathways are similar ($\sim$ 1.5 kcal mol^{-1}) for X = As^+, both the pathways were accessed by the trajectories. Here also, for all the three systems, multiple stereomutation and ring-opening events were observed during the 1 ps integration timescale.

The thermal rate constants for the stereomutation and ring-opening pathways were also calculated at 300 K using the Transition state theory (TST). The TST rate constant and lifetime can be given as,

$$k_{\text{TST}} = \frac{k_{\text{B}}T}{h}\frac{Q^{\dagger}}{Q_{\text{A}}Q_{\text{B}}}e^{-E_a/k_{\text{B}}T} \tag{3.3}$$

$$\tau = \frac{1}{k_{\text{TST}}} \tag{3.4}$$

where T and k_{B} are the temperature and Boltzman constant. $Q^{\dagger}$, Q_{A}, and Q_{B} are the total partition functions for the transition state and reactant molecules (A and B) respectively, h is the Planck's constant and τ is the lifetime. The total partition function,

$$Q = Q_{\text{trans}} Q_{\text{rot}} Q_{\text{elec}} Q_{\text{vib}} \tag{3.5}$$

is a product of the translational, rotational, electronic and vibrational partition function of the system. The τ_{TST} was found to be comparable for the stereomutation (1.95 ps) and ring-opening pathway (1.17 ps) for X = As$^+$. However, for X = Ge and Ga$^-$, the τ_{TST} for ring-opening pathway was higher ($\sim$ 262.5 and 15.6 ps respectively) as compared to the stereomutation pathway. This can be attributed to the higher energy barrier for the former pathways ($\sim$ 4.3 and 1.8 kcal mol^{-1} respectively) for the two systems. In order to have a better understanding, the average lifetimes of the stereomutation and ring-opening pathways were also calculated from the trajectories. The lifetime corresponds to the average time spent by a molecule in the reactant region before stereomutation or ring-opening. The internal coordinates ϕ and θ were followed as a function of time to calculate the lifetimes of stereomutation and ring-opening pathways. The average lifetimes for stereomutation were found to be 0.23, 0.18, and 0.083 ps for X = Ga$^-$, Ge, and As$^+$ respectively.

3.3.4 A Chiral System: $SiBNCH_2C(CH_3)_2$

In order to identify a true chiral system in which the **ptc** is either a minima or TS on the PES, various model systems with chiral Al$^-$, Si, and P$^+$ were conceived and geometry optimization and frequency calculations were performed. We identified a true chiral system $SiBNCH_2C(CH_3)_2$, where the **ptc** is a stable minimum on the PES. Since the molecule is asymmetric about Si, the two enantiomers are isoenergetic. However, the planar forms are different (similar to the *E* and *Z* isomers) and hence have different energies. All the calculations were performed at MP2/6-31+G* level of theory. The schematic representation of the different enantiomers, *R* and *S* and the *E* and *Z* isomers are given in Figure 3.17.

Figure 3.17: Schematic representation of the tetrahedral tetracoordinated *R*, *S* and planar tetracoordinated *E* and *Z* isomers.

A clockwise variation of the angle ϕ in the *R*-isomer leads to the formation of the planar *E*-isomer via transition state **TS1**, whereas an anticlockwise rotation leads to the formation of the planar tetracoordinated *Z*-isomer via transition state **TS2**. Further clockwise and anticlockwise rotation from the *E*-isomer and *Z*-isomers respectively leads to the formation of the enantiomer *S* via transition state **TS1′** and **TS1′** (Figure 3.18). It should noted that the barriers

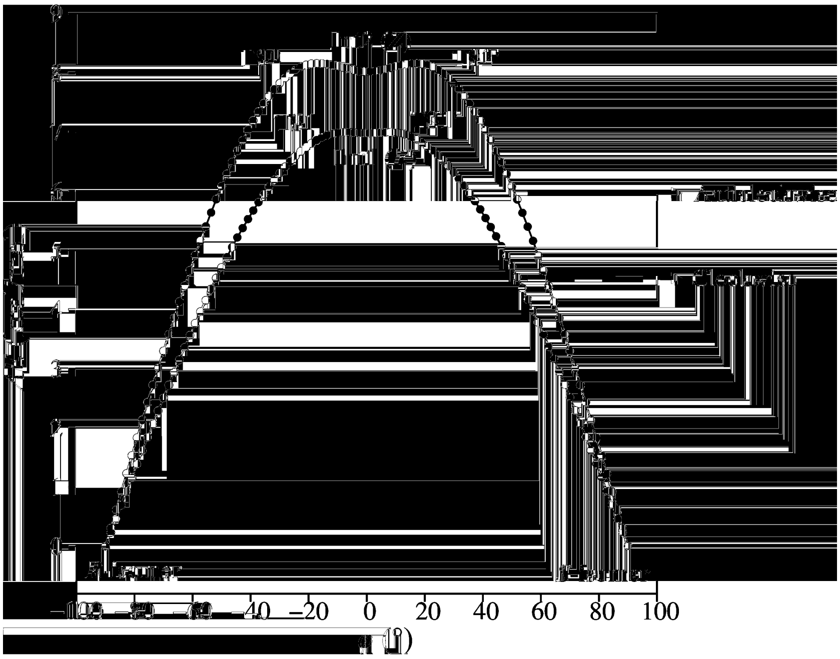

Figure 3.18: Potential energy profile for the *R*-*S* isomerization via clockwise and anticlockwise rotation.

for the clockwise and anticlockwise variation of ϕ were found to be 7.0 and 8.0 kcal mol^{-1} respectively and are lower as compared to the barriers for the ring-opening pathways (22.63 and 12.34 kcal/mol for the Si-N and Si-B bond dissociation respectively).

We then performed *ab initio* classical trajectory simulations on this system at the MP2/6-31+G(d) level. Out of the 45 trajectories initiated at the reactant region (*S* isomer), 5 were reactive, out of which, 4 exhibited isomerization reactions without bond breaking. Two representative trajectories are given in Figure 3.19, which show that the molecule goes from the *S* to *R* isomer via the *E* and *Z* isomers, respectively.

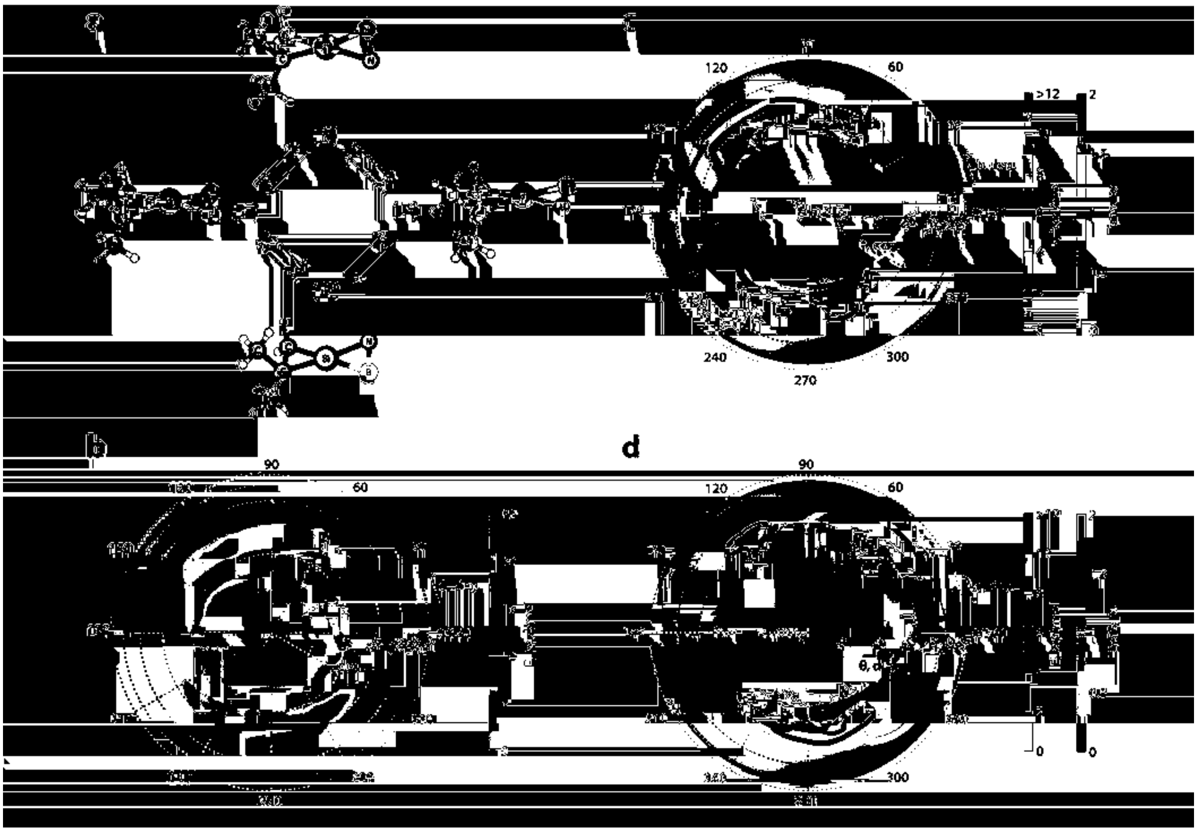

Figure 3.19: (a) Schematic representation of various pathways for the *R*-*S* isomerization, (b) Potential energy surface scan as a function of ∠SiNB versus ϕ. Sample trajectories showing *R*-*S* isomerization via (c) *E*-isomer and (d) *Z*-isomer.

3.4 Summary and Conclusions

We have identified new spiroconjugated systems, $X(C)_2(CH_2)_2$ (X = Al^-, Si, P^+, Ga^-, Ge, and As^+) analogues that exhibits isomerization between the tetrahedral structures via a planar transition state or a planar intermediate, both via rotation of the attached groups about the central atom. Different possible ring-opening pathways during isomerization were also identified for these systems. For X = Si, and Ge, the ring-opening barriers were found to be higher as compared to the stereomutation barrier. Hence, these central atoms can act as potential candidates for the designing systems for viable stereomutation. For X = P^+ and As^+, the ring-opening barriers were found to be comparable to that of the stereomutation barriers, hence the pathways were found to be competitive. A chiral neutral molecule was designed that undergoes transitions between *S* and *R* isomers via proposed *E* or *Z* isomers. The time evolution of these systems studied using quasi-classical trajectory simulations reveal that the isomerization is possible via a tetracoordinated planar center.

CHAPTER 4

INFLUENCE OF SECOND-ORDER SADDLES ON REACTION MECHANISMS

4.1 Introduction

The potential energy surface for a non-linear molecule is a 3N-6 dimensional surface (N being the number of atoms in the molecule) which depicts the variation of potential energy of the system as a function of coordinates. The high dimensionality and presence of different type of stationary points leads to the complex nature of the PES. A minima on the PES is characterized by positive curvatures in all 3N-6 directions whereas an n^{th}- order saddle point is characterized by negative curvatures in n-directions (orthogonal coordinates) and positive curvatures in the remaining 3N-6-n dimensions. Hence, a transition state is a maximum in one direction, and minimum in 3N-7 directions.

The transition state plays an important role in understanding reaction mechanisms. The transition state is an index-one saddle that connects the reactants and products (for a single-step reaction) via the minimum energy path (MEP). The MEP is the steepest descent path followed from the transition state on either directions to connect to the respective minima. For a multi-step reaction, the reactants and products are connected via different transition state(s) and intermediate(s).

Similarly, a second-order saddle (SOS) or an index-2 saddle is a maxima in two directions and minima in the remaining $3N$-8 directions (Figure 4.1). However, such higher-order saddle points have generally been overlooked. In general, SOS can be expected to have much higher energies compared to the traditional transition states, and hence their role in reaction mechanisms have been considered insignificant. However, although in certain reactions where the SOSs and transition states are comparable in energy, their role in the reaction mechanisms and dynamics have been ignored and the reaction mechanisms have been explained via the traditional transition states.[94–99]

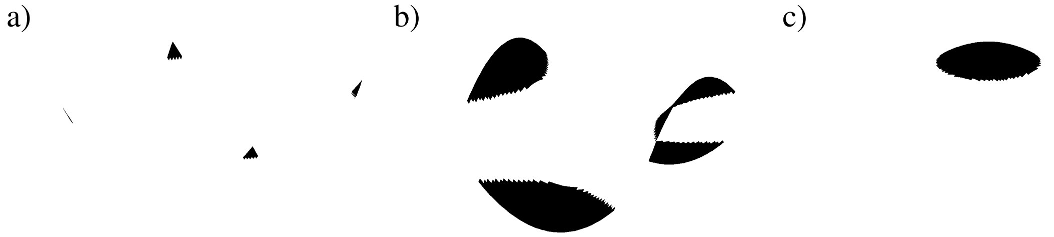

Figure 4.1: Schematic diagrams of a PES showing (a) minima in two-directions, (b) maximum in one-direction, and (c) maxima in two-directions.

The early study of index-2 saddles on the PES and their significance in chemical reactivity was reported by Heidrich and Quapp in 1986.[100] Ezra and Wiggins investigated the role of SOS in reaction dynamics using phase space structures and model Hamiltonian.[101,102] They also studied the influence of index-2 saddle on the dynamics of fragmentation of a Morse chain under tensile stress.[103] SOS were also observed in the ring–opening of cyclobutene, and isomerization of NF_2H_3 and NH_5.[104–107] An unusual trifurcation due to the presence of a second-order saddle was also reported in certain S_N2 type reactions by Gordon and coworkers.[108] The role of SOS was also investigated by Lourderaj and coworkers in the isomerization dynamics of guanidine.[109] The concerted double proton transfer reaction, which involves a SOS is also shown to be possible in addition to the single-step proton transfer reaction.[110] Quantum and classical dynamical simulations were performed on a two-degree-of-freedom potential with a SOS by Keshavamurthy and coworkers.[111]

Recently, Pradhan and Lourderaj studied the thermal denitrogenation of 1-pyrazoline using *ab initio* classical dynamics simulation studies. In 1-pyrazoline, an SOS exists which is ~ 4 kcal mol^{-1} higher in energy as compared to the synchronous transition state.[112] They found that the reaction followed the high-energy SOS path in addition to the synchronous and asynchronous mechanisms and resulted in the product, cyclopropane, with a major single inversion of configuration consistent with the experiments.[113] They also found that the trajectories following the SOS pathway resulted in cyclopropane formation with a major retention of configuration. Moreover, they found that the molecules following the SOS path show distinct characteristic features in the product energy distribution as compared to those following the transition state pathway during the reaction.

If enough energy is available to the system, and the SOS energy is comparable to the transition state, the SOS can play an important role in the dynamics of the system. However, huge computation time is required to notice such events in dynamical simulations which involve high energy barriers. The given limitation has been taken care by using enhanced sampling techniques in molecular dynamics simulations. If the probability distribution as a function of atomic coordinates is very high (usually in the minima) in two regions and these are separated by a low probability region, the system is likely to remain stuck in one of the regions for most of the time. A large amount of computational time is wasted in such a scenario. An entire class of methods have been developed to explore the different regions of the configuration space. One can use a bias potential $B(x)$ such that the effective potential now becomes $U(x) = V(x) + B(x)$. The bias potential $B(x)$ can now be adjusted so that the system samples the regions which were otherwise not accessible due to high energy barriers. In Umbrella Sampling, a number of short simulations are run with different biasing potentials to sample the different wells. In case of metadynamics, the bias potential is written as a sum of gaussian function of the reaction coordinate. In case of metadynamics, the bias potential has the form of gaussian functions. At time $t = t_0$, the potential has the form $U(x) = V(x) + B(x)$, i.e. the system is no longer at the minima and hence moves to the next local minima. More and more gaussian functions are added until the system explores the whole region in one of the potential minima, and ultimately moves to the next minima.

The motivation of this study was to understand the role of second-order saddles in reaction mechanisms with increasing E_{total}. The total energy, E_{total} available to the system is distributed in different modes using the microcanonical normal mode sampling technique. Such a study requires sampling methods that are completely unbiased and hence we chose the normal-mode sampling technique. To this end, we report here the thermal denitrogenation of 1-pyrazoline and the influence of SOS on the reaction dynamics at higher total energies. We have also studied the competition between the SOS and traditional transition state mechanism for the halo substituted, 3,3,5,5-tetrachloro-1-pyrazoline, where the SOS is only ~ 2 kcal mol^{-1} higher in energy as compared to the synchronous transition state.

4.2 Methodology

4.2.1 Stationary Points

Pradhan and Lourderaj[112] extensively investigated the thermal denitrogenation of 1-pyrazoline using *ab initio* and DFT methods. They found that CASSCF(4,4)/6-31+G* level of theory adequately described the different reaction pathways consistent with the CASPT2(12,12)/6-31+G* level of theory. Hence, in this study, the stationary points for 1-pyrazoline and 3,3,5,5-tetrachloro-1-pyrazoline, were calculated at CASSCF(4,4)/6-31+G* and CASPT2(4,4)/6-31+G*//CASSCF(4,4)/6-31+G* level of theories. The four orbitals in the active space consists of the two C-N σ and σ^* orbitals. The stationary points were characterized as minimum, or

n^{th}-order saddle point by computing the normal mode frequencies. The transition states were connected to the respective minimas by following the IRC. The calculations were performed using Gaussian16[70], NWChem[88], and Molpro software.[89]

4.2.2 Trajectories Initiated from the Reactant Region for 1-pyrazoline

In the previous study by Pradhan and Lourderaj[113], for the trajectories initiated from the reactant (**py**) region, the total energy available to the system was calculated as,

$$E_{\text{avail}} = \Delta E_{\mathbf{TS4f}} + E_{\text{ZPE}} + E_{\text{vib}} + E_{\text{rot}} + RT \tag{4.1}$$

where, $\Delta E_{\mathbf{TS4f}}$ is the energy of the highest barrier transition state with respect to the reactant, E_{ZPE} is the zero-point energy of **TS4f**, and E_{rot} and E_{vib} corresponds to the average rotational and vibrational energies of **TS4f** at the experimental temperature of 510.45 K. E_{avail} thus was calculated to be 119 kcal mol^{-1} at 510.45 K. In the current study, we provide energy of 11, 21, and 31 kcal mol^{-1} to the system in excess of 119 kcal mol^{-1}, to understand the reaction dynamics at higher energies. Thus,

$$E_{\text{total}} = E_{\text{avail}} + E_{\text{excess}} \tag{4.2}$$

A set of 500 trajectories each were initiated for E_{total} = 130, 140, and 150 kcal mol^{-1}. A summary of the energy available and the number of trajectories initiated for each system is given in Table 4.1. The *ab initio* classical trajectory simulations were performed using VENUS/NWChem programs[91,92] at the CASSCF(4,4)/6-31+G* level of theory. The initial coordinates and momenta were chosen for a given total energy by using the microcanonical normal mode sampling technique.[14] The trajectories were integrated for a total of 2 ps using the velocity-Verlet algorithm[93] with the necessary forces computed on-the-fly at the CASSCF(4,4)/6-31+G* level of theory.

4.2.3 Trajectories Initiated from the SOS Region for 1-pyrazoline

To understand the post-SOS dynamics, trajectories were initiated from the SOS of 1-pyrazoline. A set of 40 trajectories were initiated from the SOS and integrated in the forward and reverse directions for 600 fs each. The initial coordinates and magnitude of the momenta for the forward and reverse trajectories are the same except that the directions (forward and reverse) are defined by the sign of the momenta. If p_i^f defines the sign of the momenta for i^{th} component in the forward direction, $-p_i^f$ defines the direction of momenta for the i^{th} component in the reverse direction. These trajectories were then stitched together to get a complete trajectory. The total energy available to the system at the SOS was calculated as,

$$E_{\text{avail}} = 140.0 - \Delta E_{\mathbf{sos}} \tag{4.3}$$

where $\Delta E_{\mathbf{sos}}$ is the energy of SOS with respect to 1-pyrazoline, and is equal to 44.12 kcal mol^{-1}. Therefore, the trajectories were integrated with E_{avail} = 95.88 kcal mol^{-1}. Out of the 40 trajectories initiated, 25 resulted in complete trajectories i.e. Reactant → SOS → Product.

4.2.4 Trajectories Initiated from the SOS Region for 3,3,5,5-tetrachloro-1-pyrazoline

The E_{avail} for the system was calculated by assuming a Boltzmann distribution of states at the SOS.

$$E_{\text{avail}} = E_{\text{ZPE}} + E_{\text{vib}} + E_{\text{rot}} + 2RT \tag{4.4}$$

where, E_{ZPE}, E_{rot}, and E_{vib} are the zero-point-energy, average rotational, and average vibrational energy at 510.45 K, and RT is the energy along each of the orthogonal coordinate having negative curvature. The trajectories from the SOS were integrated in the forward and reverse directions and were stitched together to get a complete trajectory, similar to 1-pyrazoline.

Table 4.1: Summary of the total energy and number of trajectories initiated for each system.

Trajectories initiated from	E_{avail}	E_{excess}	E_{total}	Total trajectories initiated
py	119.00	11.00	130.00	500
py	119.00	21.00	140.00	500
py	119.00	31.00	150.00	500
sos	95.88	0.00	95.88	40
Cl_sos	46.69	0.00	46.69	50

4.3 Results and Discussions

4.3.1 Potential Energy Profile

A general chemical structure for 1-pyrazoline (X = H) and 3,3,5,5-tetrachloro-1-pyrazoline (X = Cl) is shown in Figure 4.2. The important geometrical parameters used to understand different mechanisms during the dynamical simulations are labelled. Here, r_1, r_2, and d_s represent the two C-N bond lengths and the mean C-N bond length respectively. The dihedral angle ϕ_s = $(\phi_1 - \phi_2)/2$ is used to represent the out of plane bending motion of CH_2 group of pyrazoline with respect to the four atoms containing the C-N bonds.

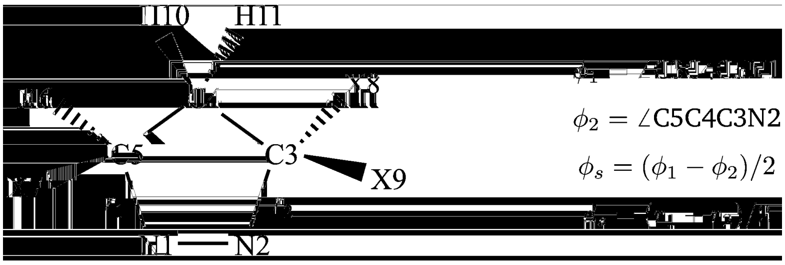

Figure 4.2: General representation of the molecular structures used in the present study. The atom numbers and important geometrical parameters are labelled.

(a) 1-pyrazoline

The thermal denitrogenation of 1-pyrazoline has been studied earlier in detail by Pradhan and Lourderaj using different DFT functionals, MP2, CASSCF, and CASPT2 methods.[112] Here, we summarize the results so as to explain the dynamics of the system in the later sections.

The reactant, 1-pyrazoline can exist in two degenerate isomeric forms (**py** and **py′**) depending upon the position of the -CH_2 group i.e. above or below the plane containing C3, C4, and C5 respectively. The interconversion between these two isomers is possible via a transition state **ts0**, with a barrier of 0.17 kcal mol^{-1}. The denitrogenation of **py** can then occur either via a synchronous or asynchronous pathway.

The synchronous pathway accounts for breaking of both the C-N bonds simultaneously via a transition state **ts1**, with a barrier of 40.04 kcal mol^{-1}, which hence leads to the formation of the trimethylene diradical **tmd** with the liberation of N_2. A similar pathway was mapped from **py′** leading to the formation of **tmd′** via **ts1′**, Figure 4.3(a). Interestingly, the isoenergetic transition states **ts1** and **ts1′** are connected via a second-order saddle. The normal modes corresponding to the two imaginary frequencies represent the synchronous C-N bond stretching and the -CH_2 out-of-plane bending motion. The symmetric C-N stretching motion in the **sos** connects the product cyclopropane (**cyp**) and transition state **ts0** on either sides, whereas the out-of-plane bending motion connects transition states **ts1** and **ts1′**. Figure 4.3(b) shows the PES for the denitrogenation of 1-pyrazoline mapped by performing a relaxed scan along the coordinates ϕ_s and d_s.

On the contrary, the asynchronous denitrogenation pathway happens via a step-wise manner leading to the formation of a diazenyl diradical, which then leads to the formation of the product cyclopropane. The asynchronous denitogenation can occur via a clockwise or anticlockwise rotation about one of the C-N bonds with barriers of 45.5 and 47.0 kcal mol^{-1} respectively. The potential energy profiles for the asynchronous pathway are given in Figure 4.4.

(b) 3,3,5,5-tetrahalo-1-pyrazoline

It is of interest to study the competition between the reaction mechanisms for systems with comparable TS and SOS energies. To this end, we substituted the four H-atoms connected to the sp^3 hybridized C3 and C5 atoms with F and Cl. The potential energy profiles for

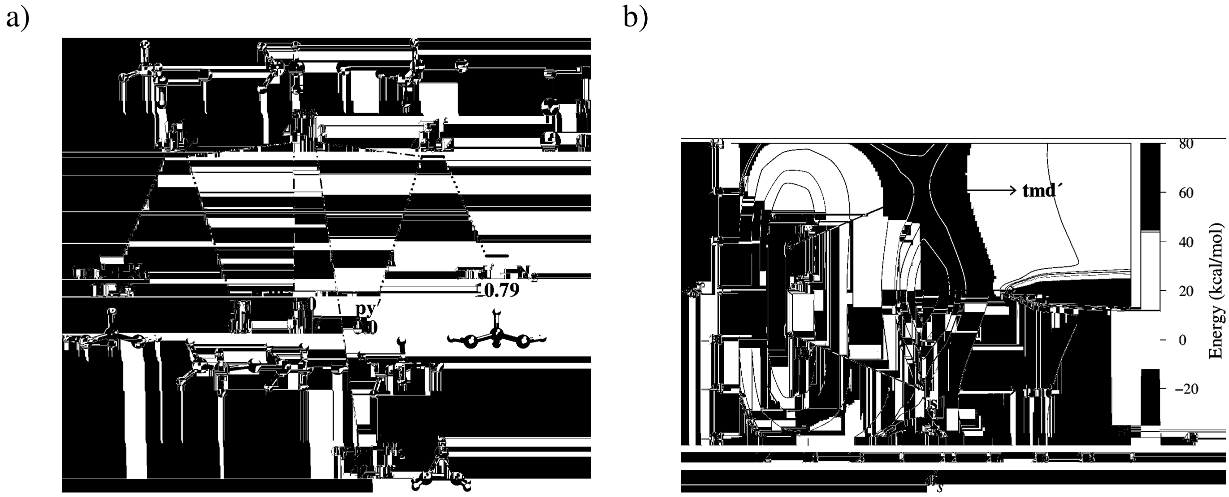

Figure 4.3: (a) Potential energy profile for the synchronous denitrogenation of 1-pyrazoline and (b) PES obtained by performing a relaxed scan along the coordinates d_s and ϕ_s. The MEPs are plotted on the PES with solid black lines. The energies are obtained at the CASSCF(4,4)/6-31+G* level of theory and are reported in kcal mol^{-1}.

3,3,5,5-tetrafluoro-1-pyrazoline and 3,3,5,5-tetrachloro-1-pyrazoline were then mapped at the CASSCF(4,4)/6-31+G* level of theory. We found that, the potential energy profiles for the halo-substituted systems show similar characteristic features as compared to 1-pyrazoline. The relative energies and important geometrical parameters for the two systems are compared with that of 1-pyrazoline in Table 4.2.

The 3,3,5,5-tetrachloro-1-pyrazoline exists in two degenerate isomeric forms, **Cl_py** and **Cl_py′**. Similar to **py**, here also the synchronous denitrogenation occurs via simultaneous cleavage of both the C-N bonds, which leads to the formation of tetrachloro-trimethylene diradical, **Cl_tmd** (Figure 4.5). The reactant isomers **Cl_py** and **Cl_py′** are connected via **Cl_ts0** with a barrier of 0.41 kcal mol^{-1}. The eigen vector for the imaginary frequency of **Cl_ts0** corresponds to the out of plane bending motion of -CH$_2$ group. It is worth pointing out that the **Cl_sos** and **Cl_ts1** barrier is now reduced to $\sim$ 2 kcal mol^{-1} as compared to $\sim$ 4 kcal mol^{-1} for **py**. For **F_py**, this energy difference is even lower, $\sim$ 1.5 kcal mol^{-1} (Figure 4.6). However, the PES for **F_py** $\rightleftharpoons$ **F_ts0** $\rightleftharpoons$ **F_py′** pathway is flat (0.01 kcal mol^{-1} barrier). This needs further investigation of the mechanisms for this system at higher level of theories and is a topic of study in itself and will be investigated in the future. Hence, further studies were performed by considering 3,3,5,5-tetrachloro-1-pyrazoline.

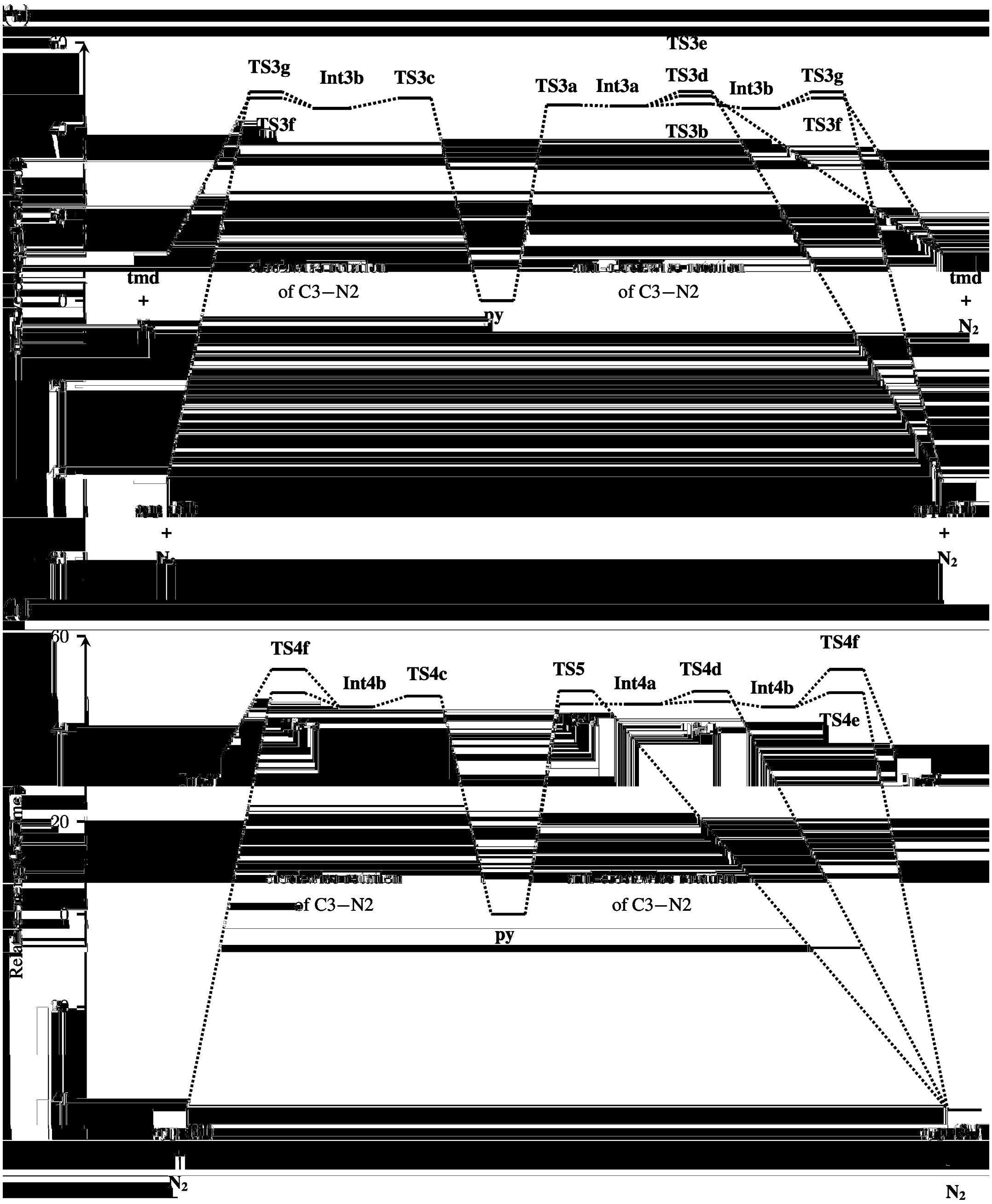

Figure 4.4: The asynchronous denitrogenation pathways for 1-pyrazoline at CASSCF(4,4)/6-31+G* level of theory via (a) planar like and (b) perpendicular like diazenyl diradicals. The **TS5** represents the transition state for a concerted denitrogenation pathway. This figure is adapted from Pradhan and Lourderaj, *Phys. Chem. Chem. Phys.*, **2017**, *19*, 27468-27477.

Table 4.2: Important parameters and normal mode frequencies for the stationary points on the PES for the synchronous denitrogenation of 1-pyrazoline, 3,3,5,5-tetrafluoro-1-pyrazoline, and 3,3,5,5-tetrachloro-1-pyrazoline

Parameter[a]	1-pyrazoline				3,3,5,5-tetrafluoro-1-pyrazoline				3,3,5,5-tetrachloro-1-pyrazoline			
	py	**ts0**	**ts1**	**sos**	**F_py**	**F_ts0**	**F_ts1**	**F_sos**	**Cl_py**	**Cl_ts0**	**Cl_ts1**	**Cl_sos**
r_1 (Å)	1.51	1.51	2.08	2.10	1.51	1.51	2.08	2.10	1.52	1.52	2.02	2.03
r_2 (Å)	1.51	1.51	2.08	2.10	1.51	1.51	2.08	2.10	1.52	1.52	2.02	2.03
ϕ_1 (°)	17.74	0.0	40.79	0.00	7.42	0.00	30.89	0.00	16.89	0.00	31.41	0.00
ϕ_2 (°)	−17.74	0.00	−40.79	0.00	−7.42	0.00	−30.89	0.00	−16.89	0.00	−31.41	0.00
ϕ_s (°)	17.74	0.0	40.79	0.00	7.42	0.00	30.89	0.00	16.89	0.00	31.41	0.00
d_s (Å)	1.51	1.51	2.08	2.10	1.51	1.51	2.08	2.10	1.52	1.52	2.02	2.03
ω_{ss} (cm^{-1})	1016	912	647i	622i	1291	1289	524i	530i	1053	1048	639i	642i
ω_{op} (cm^{-1})	125	90i	243	207i	24	19i	81	63i	52	36i	86	59i
ΔE	0.00	0.17	40.04	44.12	0.00	0.01	42.66	43.98	0.00	0.41	29.44	31.92
ΔE_{ZPE}	0.00	0.08	34.17	37.95	0.00	−0.27	38.37	39.55	0.00	0.38	25.87	28.27
$\Delta E_{\mathrm{CASPT2}}$	0.00	0.45	38.83	45.22	0.00	0.10	37.63	39.46	0.00	0.90	25.53	29.56

[a] ω_{ss} and ω_{op} are harmonic frequencies corresponding to symmetric stretching of C−N bonds and out-of-plane motion of CH_2 group with respect to the plane containing the four atoms of the C−N bonds respectively. The relative energies with respect to the reactant are reported in kcal mol^{-1}. $\Delta E_{\mathrm{CASPT2}}$ is the relative energy obtained at the CASPT2(4,4)/6-31+G* level of theory and ΔE_{ZPE} is the zero-point energy (ZPE) corrected relative energy.

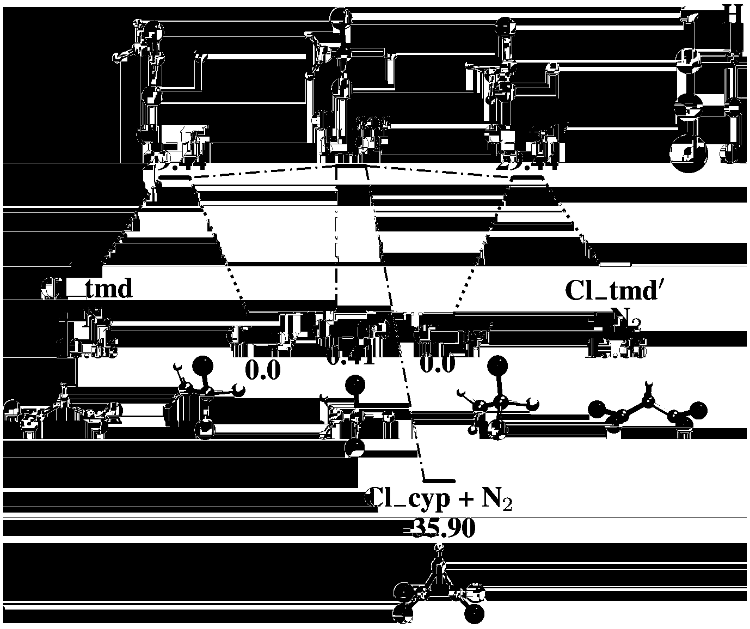
Cl_tmd
Cl_tmd′
0.0
0.0
Cl_cyp + N2
35.90

Figure 4.5: Potential energy profiles for the synchronous denitrogenation of 3,3,5,5-tetrachloro-1-pyrazoline mapped at the CASSCF(4,4)/6-31+G* level of theory. The energies are reported in kcal mol^{-1}.

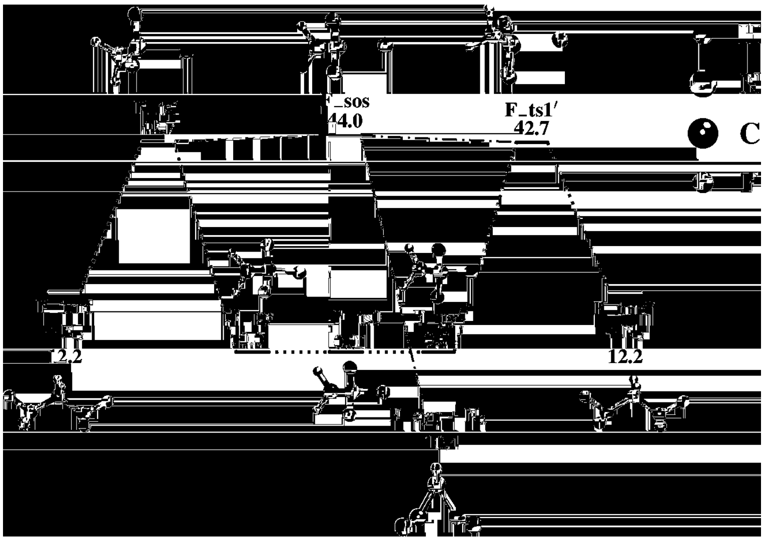
_sos
F_ts1′
42.7
C
2.2
12.2

Figure 4.6: Potential energy profiles for the synchronous denitrogenation of 3,3,5,5-tetrafluoro-1-pyrazoline mapped at the CASSCF(4,4)/6-31+G* level of theory. The energies are reported in kcal mol^{-1}.

4.3.2 *Ab initio* Classical Dynamics Simulations: 1-pyrazoline

The classical dynamical simulations for the thermal denitrogenation of 1-pyrazoline was reported earlier by Pradhan and Lourderaj at E_{total} of 119 kcal mol^{-1}.[113] Here, we report the findings of the study performed with higher total energies i.e. E_{total} of 130, 140, and 150 kcal mol^{-1}.

(a) Reaction Pathways

A total of 500 trajectories each were integrated for E_{total} = 130, 140, and 150 kcal mol^{-1}. The number of reactive trajectories i.e. the trajectories leading to the formation of products were 101, 216, and 304 for E_{total} of 130, 140, and 150 kcal mol^{-1} respectively. As discussed earlier, the denitrogenation of 1-pyrazoline can occur either via the synchronous breaking of both the C-N bonds or via the asynchronous denitrogenation pathway. These pathways were characterized by monitoring the following geometrical parameters. A trajectory is said to follow the synchronous pathway if both the C-N bond distances attain a value of 2.5 Å within 40 fs. The C-N distances larger than 2.5 Å corresponds to a trajectory leaving the transition state region. The transition state region was defined by sampling initial conditions of the trajectories at the synchronous transition state. From the initial conditions of the sampled trajectories, the upper bound of the C-N distance was found to be 2.5 Å. Also, the time interval of 40 fs approximately correspond to the symmetric C-N bonds stretching vibrational period. The trajectory simulations reveal that both the synchronous and asynchronous pathways were followed during the reaction, with the former being the dominant pathway. The two C-N bond distances of the reactive trajectories for the three E_{total} are plotted on a relaxed PES scan of both the C-N bond distances in Figure 4.7. For the trajectories following the synchronous pathway, both the C-N bonds break simultaneously, hence tracing a diagonal pathway as shown in Figure 4.7(a). On the contrary, for the asynchronous pathway, first one of the C-N bond breaks and the other C-N bond oscillates about the equilibrium C-N bond length of $\sim$ 1.5 Å. This is then followed by the dissociation of the second C-N bond, leading to the formation of **tmd**, which

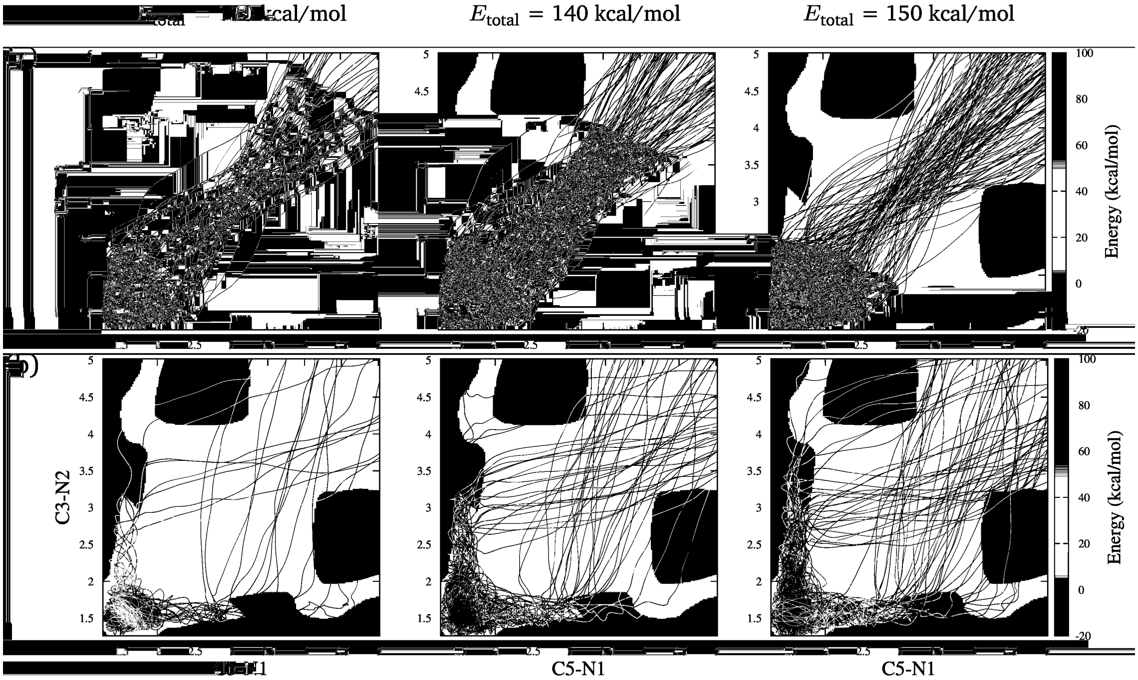

Figure 4.7: Reactive trajectories following (a) synchronous, and (b) asynchronous denitrogenation pathways for E_{total} = 130, 140, and 150 kcal mol^{-1}. The trajectories are plotted on a relaxed PES scan of both the C-N bond distances (Å) calculated at the CASSCF(4,4)/6-31+G* level of theory.

then closes to form the product, **cyp**. The statistics from the trajectory simulations (Table 4.3) reveal that, on increasing the total energy available to the system, the percentage of product formation increased (8%, 20%, 43%, and 61% for E_{total} = 119, 130, 140, and 150 kcal mol^{-1} respectively). With increase in total energy of the system from 119 to 130 kcal mol^{-1}, a small increase in the trajectories following the synchronous path (57.6% to 58.4%) was observed. However, on going to 140 and 150 kcal mol^{-1}, the percentage of trajectories following the synchronous pathway decreased from 57.4% and 54.9% respectively. On the contrary, the fraction of trajectories following the asynchronous path decreased from 37.9% for E_{total} = 119 and to 31.7% for 130 kcal mol^{-1}, which then increased to 33.3% and 34.6% for E_{total} of 140, and 150 kcal mol^{-1} respectively. These results qualitatively indicate the opening of the high barrier asynchronous denitrogenation pathway as the total energy available to the system increases.

Table 4.3: Number of trajectories following synchronous (Sync), asynchronous (Async), and SOS pathways and showing single inversion (SI), retention (Ret), and double inversion (DI) of configuration during the formation of **cyp** for different E_{total}. The number of trajectories remaining as diradical (DR) during the integration time of 2 ps are also tabulated[a]

	119 kcal mol^{-1b}				130 kcal mol^{-1}					140 kcal mol^{-1}					150 kcal mol^{-1}				
Path	SI	Ret	DI	All	SI	Ret	DI	DR	All	SI	Ret	DI	DR	All	SI	Ret	DI	DR	All
Sync	72	40	68	181	25	14	14	6	59	53	27	33	11	124	78	33	44	12	167
				57.6%					58.4%					57.4%					54.9%
Async	52	24	44	119	12	3	14	3	32	39	12	18	3	72	49	21	26	9	105
				37.9%					31.7%					33.3%					34.6%
SOS	4	6	4	14	2	5	3	0	10	7	3	10	0	20	6	13	11	2	32
				4.5%					9.9%					9.3%					10.5%
Total[c]	128	70	116	314	39	22	31	9	101	99	42	61	14	216	133	67	81	23	304
cyp%	41	22	37		42	24	34			49	21	30			47	24	29		

[a] The fraction of trajectories following synchronous, asynchronous, and SOS pathways are also given as percentages under the column 'All'. The row **cyp**% represents the percentage of cyclopropane formed with SI, Ret, and DI of configuration. [b] Data taken from[113]. [c] A total of 4000 trajectories were integrated for E_{total} = 119 kcal mol^{-1} and 500 each for the other three energies.

Table 4.4: The 95% confidence interval (CI) for the trajectories following the synchronous, asynchronous, and **sos** pathways for different E_{total}.

E_{total}	Total Traj	Reactive	Sync	CI_{Sync}	Async	CI_{Async}	**sos**	$\text{CI}_{\textbf{sos}}$
119	4000	314	181	(57.6±5.5)%	119	(37.9±5.4)%	14	(4.5±2.3)%
130	500	101	59	(58.4±9.6)%	32	(31.7±9.1)%	10	(9.9±5.8)%
140	500	216	124	(57.4±6.6)%	72	(33.3±6.3)%	20	(9.3±3.9)%
150	500	304	167	(54.9±5.6)%	105	(34.5±5.3)%	32	(10.5±3.4)%

[a] The confidence interval for a given event can be calculated as, $\text{CI} = p \pm z\sqrt{\frac{p(1-p)}{n}}$.Here, p is the sample proportion, n is the sample size, and z is the Z-value for the desired confidence level (i.e. $z = 1.96$ for 95% confidence level). A 95% confidence interval means we are 95% confident that for a given E_{total}, the particular fraction of trajectories follow the **sos** pathway.

(b) Stereochemistry of Product

We then looked at the stereochemistry of the product, **cyp** obtained during the denitrogenation reaction. It should be noted that a fraction of trajectories for different E_{total} lead to the formation of **tmd** at the end of the total integration time of 2 ps and were not included during the characterization of the stereochemistry of the products. These trajectories if integrated further would result in ring closure and hence, the formation of **cyp**. The product, **cyp** can be formed with a single inversion (SI), double inversion (DI), or retention of configuration (Ret) at the C3 and C5 position of **py**. The SI, DI, and Ret of configuration were monitored by tracking the number of half-rotations (180° rotations) before ring closure about the C3-C4, and C4-C5 bonds. A combination of odd number of half-rotations about the C3-C4 and C4-C5 bonds leads to **cyp** with DI, whereas a combination of zero or even number of half-rotations yields **cyp** with retention of configuration. On the contrary, a combination of odd number of half-rotation about one of the C-N bonds and zero or even number of half-rotation about the other C-N bonds leads to the formation of **cyp** with SI of configuration. Representative trajectories showing SI, DI, and Ret are given in Figure 4.8. It was observed that the **cyp** with a SI of configuration is the major product whereas **cyp** with retention is the minor product for all the total energies used (Table 4.3). It should be noted that, experimentally a major SI of configuration was observed for the **cyp** products obtained during the thermal denitrogenation of *trans*-3,5-dimethyl-1-pyrazoline.[114,115]

(c) Second-order Saddle Dynamics

The trajectory analysis for all the three total energies show that a fraction of trajectories access the higher energy second-order saddle avoiding the transition states **ts1** and **ts1′**. The boundary conditions used for defining the transition state **ts1/ts1′** and **sos** regions are given is Table 4.5. It was observed that, the number of trajectories accessing the **sos** region increased with E_{total}. The percentage of trajectories increased on going from 119 to 130 kcal mol^{-1} and then remained $\sim$ 10% for 130, 140, and 150 kcal mol^{-1}. Also, from the distribution of trajectories following

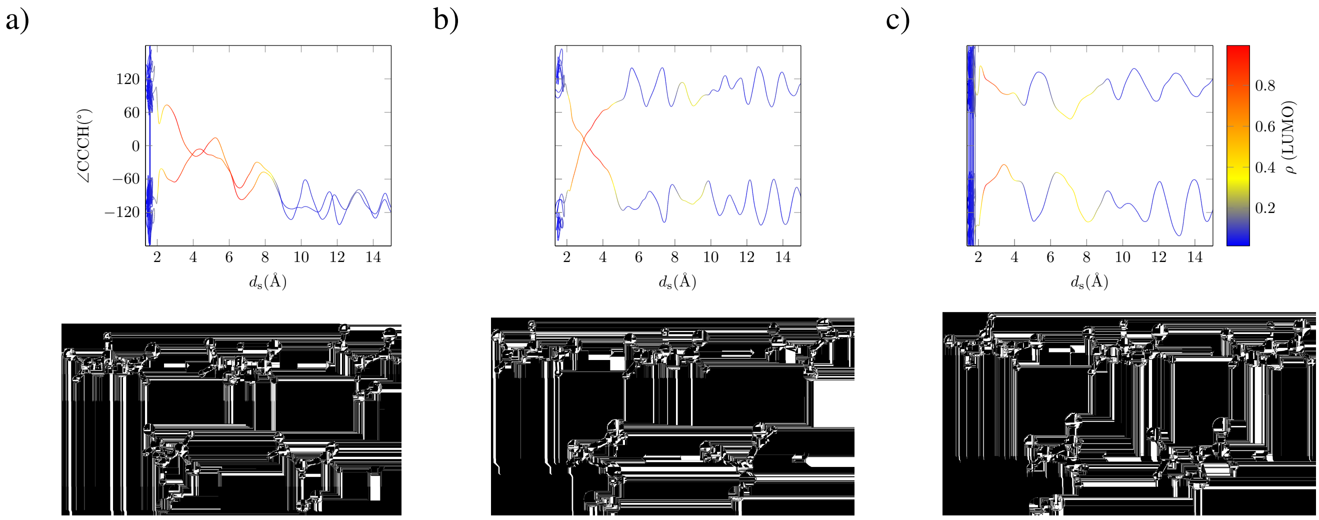

Figure 4.8: Variation of ∠C5C4C3H8 and ∠C3C4C5H6 as a function of d_s showing (a) SI, (b) DI, and (c) Retention of configuration. The colorbar represents the electron density in the LUMO. The molecule is said to have a diradical character when the electron density in the LUMO is > 0.45. The snapshots of the representative trajectories are shown below the plots. The two H-atoms are shown in different colors (yellow and green) to show the inversion/retention of configuration taking place during the product formation.

different reaction pathway it is seen that, although the **sos** has a lower barrier (44.12 kcal mol^{-1}) than the asynchronous transition states (48-53 kcal mol^{-1}), the fraction of trajectories following the asynchronous pathway is higher than the SOS. This clearly indicates the non-statistical nature of the system. Moreover, the change in the fraction of trajectories following the Async and SOS pathway indicates the change in the nature of bottlenecks in the phase space with total energy. The trajectories following the SOS pathway for the three total energies, plotted on a relaxed PES scan as a function of ϕ_s versus d_s is given in Figure 4.9. Here, the ϕ_s and d_s are defined as $(\phi_1 - \phi_2)/2$ and $(r_1 + r_2)/2$ respectively.

Table 4.5: Boundary conditions used for d_s and ϕ_s to define the transition state (**ts1**/**ts1′**) and the second-order saddle region.

Region	d_s	ϕ_s
ts1′	2.00 to 2.16	30.9 to 50.9
sos	2.02 to 2.18	−18.0 to 18.0
ts1	2.00 to 2.16	−30.9 to −50.9

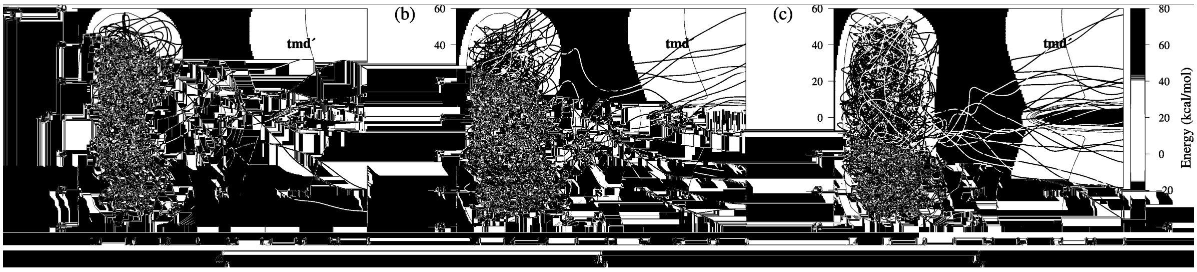

Figure 4.9: Trajectories traversing the SOS pathway for E_{total} = (a) 130, (b) 140, and (c) 150 kcal mol^{-1}.

The different dynamical pathways followed are associated with the intramolecular vibrational energy redistribution (IVR) that occurs during the reaction. From Figure 4.9, it can be seen that the trajectories show multiple isomerization events between the reactant isomers **py** and **py**′ before dissociating via the SOS pathway. This can be explained by the fact that the out-of-plane bending motion of the CH_2 group that leads to **py** $\rightleftharpoons$ **py**′ is a low frequency oscillation, hence sufficient energy is available along this mode to facilitate several isomerization events. On the contrary, the C-N bond-breaking occurs when enough energy is available along the C-N stretching mode, the critical oscillator for Sync and SOS pathways. The different dynamical pathways followed by the trajectories traversing the SOS region is given in Table 4.6.

It can be seen that the majority of the trajectories deviate from the MEP during the reaction. Interestingly, 3/500 and 6/500 trajectories exhibited recrossing from the SOS region before formation of the product **cyp** i.e. these trajectories first access the SOS region and then traverse back to form the reactant, and then form the product via the transition state. Sample trajectories showing such recrossing events are shown in Figure 4.10.

To improve the statistics, we also initiated 40 trajectories with E_{avail} = 95.88 kcal mol^{-1}, from the **sos** region and integrated them in the forward and reverse directions. Out of the 40 trajectories initiated, 25 gave complete trajectories i.e. **py**/**py**′ $\rightarrow$ **sos** $\rightarrow$ **cyp**. These trajectories followed different dynamical pathways as shown in Figure 4.11. We can see that the majority of the trajectories directly access the **sos** region from **py**/**py**′, consistent with the trajectories

Table 4.6: Pathways followed by various trajectories dissociating via the **sos** region for an E_{total} of 130, 140, and 150 kcal mol^{-1}

		No. of trajectories for E_{total}		
	Dynamical pathway	130	140	150
1.	**py** $\rightarrow$ **sos** $\rightarrow$ **cyp**	4	4	10
2.	**py** $\rightarrow$ **sos** $\rightarrow$ **tmd′**	0	2	4
3.	**py** $\rightarrow$ **sos**$\rightarrow$ **tmd**	0	1	5
4.	**py** $\rightarrow$ **ts0** $\rightarrow$ **sos** $\rightarrow$ **cyp**	0	1	1
5.	**py** $\rightarrow$ **ts0** $\rightarrow$ **sos** $\rightarrow$ **tmd**	0	2	1
6.	**py** $\rightarrow$ **ts0** $\rightarrow$ **sos** $\rightarrow$ **tmd′**	1	2	1
7.	**py** $\rightarrow$ **ts1**$\rightarrow$ **sos** $\rightarrow$ **cyp**	0	0	1
8.	**py** $\rightarrow$ **ts1** $\rightarrow$ **sos** $\rightarrow$ **tmd′**	0	1	0
9.	**py′** $\rightarrow$ **sos** $\rightarrow$ **cyp**	1	0	3
10.	**py′** $\rightarrow$ **sos** $\rightarrow$ **tmd**	2	2	1
11.	**py′** $\rightarrow$ **sos** $\rightarrow$ **tmd′**	0	1	1
12.	**py′** $\rightarrow$ **ts0** $\rightarrow$ **sos** $\rightarrow$ **cyp**	2	0	1
13.	**py′** $\rightarrow$ **ts0** $\rightarrow$ **sos** $\rightarrow$ **tmd**	0	1	1
14.	**py′** $\rightarrow$ **ts0** $\rightarrow$ **sos** $\rightarrow$ **tmd′**	0	0	1
15.	**py′** $\rightarrow$ **ts1′** $\rightarrow$ **sos** $\rightarrow$ **cyp**	0	1	0
16.	**py′** $\rightarrow$ **ts1′** $\rightarrow$ **sos** $\rightarrow$ **tmd′**	0	1	1
17.	**py′** $\rightarrow$ **ts0** $\rightarrow$ **sos** $\rightarrow$ **ts1** $\rightarrow$ **tmd**	0	1	0

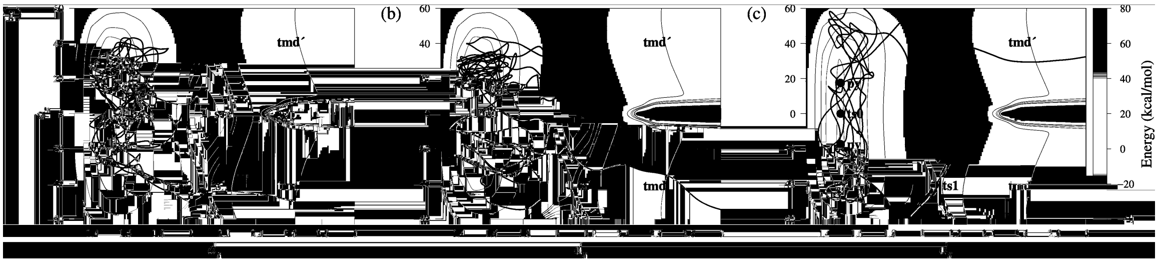

Figure 4.10: Sample trajectories showing recrossing events via the **sos** for E_{total} = 150 kcal mol^{-1}.

initiated from the **py** region which follow the SOS pathway. The remaining 15 trajectories lead to the formation of product, when integrated both in forward and backward directions.

An interesting thing to note is the stereochemistry of the products obtained via the SOS pathway. It can be seen that the majority of the trajectories traversing the **sos** region lead to the formation of **cyp** with retention of configuration (except for E_{total} = 140 kcal mol^{-1}).

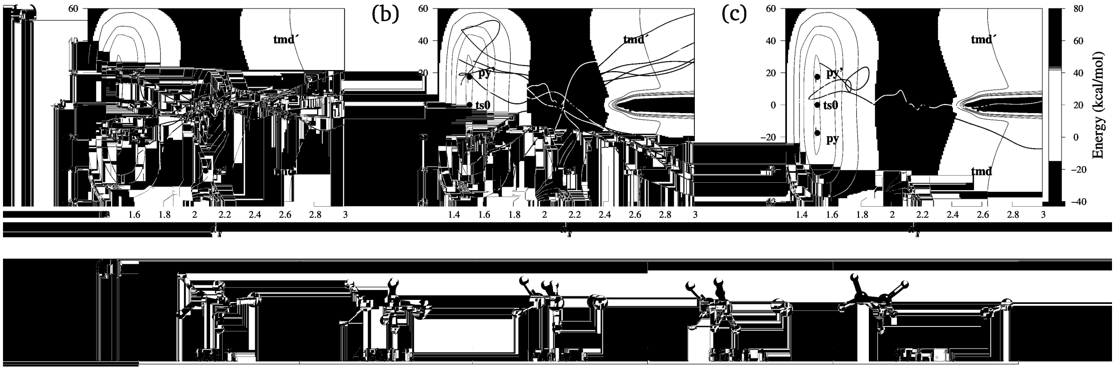

Figure 4.11: Trajectories initiated from **sos** region following different reaction pathways during the thermal denitrogenation of 1-pyrazoline: (a) **py/py′**$\rightarrow$ **sos** $\rightarrow$ **cyp**, (b) **py/py′** $\rightarrow$ **sos** $\rightarrow$ **tmd/tmd′**, and (c) **py′**$\rightarrow$ **ts0** $\rightarrow$ **sos** $\rightarrow$ **cyp** (d) Representative trajectory showing the denitrogenation via the **sos** pathway.

This is observed for both, trajectories initiated from the **py** and those initiated from the **sos** regions. This preference can be explained by considering the pathway taken by the trajectories dissociating via the **sos** region. A direct ring closure from the **sos** following the MEP, leads to the formation of **cyp** with retention, since the molecule does not have enough time for rotation about the C-C bonds. On the other hand, the trajectories not following the MEP, have enough time for rotation about the C-C bonds to result in **cyp** with Si or DI of configuration.

(d) RRKM and Trajectory Lifetimes

We investigated the (non-)statistical nature of the dynamics of thermal dissociation of 1-pyrazoline studied at different energies. The RRKM lifetimes, τ_{RRKM} for the reaction via **ts1** were found to be 0.64, 0.33, and 0.19 ps for E_{total} = 130, 140, and 150 kcal mol^{-1}, respectively. As the energy available to the system increases, the products are formed readily, and hence the τ_{RRKM} decreases. To have an insight, the lifetimes of the trajectories following the synchronous denitrogenation pathway were also calculated. The lifetime of a trajectory was calculated as the total time taken for both the C-N bonds to attain a value of 5 Å i.e. the time taken by the trajectory for the formation of the products. The average lifetime for the synchronous trajectories, $\overline{\tau}_{\mathrm{sync}}$ were 1.10, 0.97, and 0.87 ps for E_{total} = 130, 140, and 150 kcal mol^{-1} respectively. These lifetimes are clearly far greater than those calculated from the RRKM theory.

Similarly, we also calculated the RRKM rate constant at the **sos**. It should be noted that, the RRKM rate constant is not defined at the **sos**. However, we can define a formal (N-2)-dimensional dividing surface for a N-dimensional phase space. Hence, the $k_{\mathbf{sos}}$ here was approximately calculated by considering the absolute value for the frequency of the out-of-plane bending motion of the -CH_2 group and taking the C-N symmetric stretching motion as the critical oscillator. Here, E_0 was taken as the energy of **sos** with respect to **py**. The τ_{sos} calculated thus were 2.99, 1.41, and 0.75 ps for E_{total} = 130, 140, and 150 kcal mol^{-1} respectively. The RRKM lifetimes for the **sos** are higher as compared to the **ts1**. This is expected because, as the energy barrier (E_0) increases, the less readily the products are formed. Since the number of trajectories traversing the **sos** region were less, we did not calculate the average lifetimes. However, the deviation of the trajectory lifetimes from that calculated using the RRKM theory for synchronous pathway, indicates the non-statistical nature of the denitrogenation reaction. This is further evident from the recrossing trajectories via **ts1** and **sos**, observed for the system.

(e) Product Energies

The kinetic energy available to the system is distributed among the rotational, vibrational and translational modes of the system during product formation. To this end, we have calculated the average translational ($\overline{E}_{\mathrm{trans}}$) and rotational energy ($\overline{E}_{\mathrm{rot}}$) of the fragments **cyp** and N_2 when they are 12 Å apart, for all the reactive trajectories. The distribution of the relative translational energy (E_{trans}) for trajectories following different pathways is given in Figure 4.12. The average relative translational energy, $\overline{E}_{\mathrm{trans}}$ was calculated to be 41.20, 41.69, and 44.31 for the trajectories following synchronous denitrogenation pathway for E_{total} = 130, 140, and 150 kcal mol^{-1} respectively. The $\overline{E}_{\mathrm{trans}}$ for the fragments **cyp** and N_2 increased with the total energy available to the system. This can be explained by the fact that, the kinetic energy release along the reaction coordinate increases as E_{total} increases. In addition, the $\overline{E}_{\mathrm{trans}}$ for

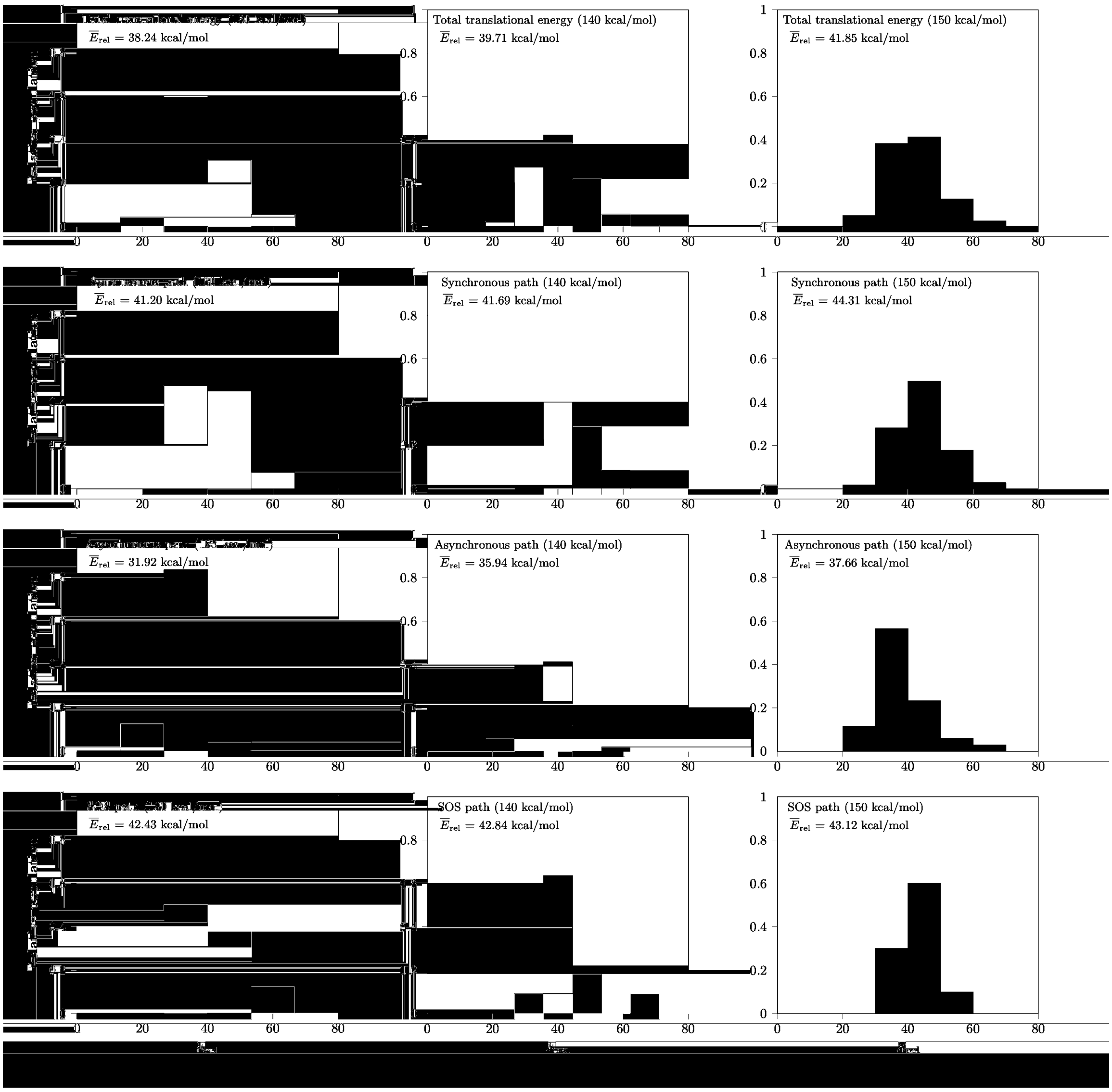

Figure 4.12: Distribution of relative translational energy between the **cyp** and N_2 fragments for trajectories following synchronous, asynchronous, and SOS pathways for the three total energies.

the trajectories following the **sos** pathway were found to be 42.43, 42.84, and 43.12 kcal mol^{-1} for E_{total} = 130, 140, and 150 kcal mol^{-1} respectively. We can see that the $\overline{E}_{trans}$ for SOS trajectories is larger than that for synchronous and asynchronous trajectories, similar to that observed for E_{total} = 119 kcal mol^{-1}.[113] However, for 150 kcal mol^{-1}, the $\overline{E}_{trans}$ for synchronous trajectories is more than that for SOS. This may be due to a large number of trajectories deviating the MEP, and hence leading to the formation of diradicals before the formation of products. It should be noted that, if a trajectory directly skirts through the MEP from the **sos** to form **cyp**, then excess kinectic energy is expected to get transferred along the translational modes of the fragments. Similarly, for the trajectories following asynchronous pathway, the $\overline{E}_{\text{trans}}$ was found to be 31.92, 35.94, and 37.66 for E_{total} = 130, 140, and 150 kcal mol^{-1} respectively. It can be seen that the $\overline{E}_{\text{trans}}$ for synchronous trajectories is greater than that for the asynchronous trajectories. This is because the asynchronous pathway involves rotation about the C-N bond, leading to build-up of angular momentum. This increases the $\overline{E}_{\text{rot}}$ energy for the asynchronous trajectories, hence leading to lower $\overline{E}_{\text{trans}}$.

4.3.3 *Ab initio* Classical Dynamics: 3,3,5,5-tetrachloro-1-pyrazoline

The MEPs for 3,3,5,5-tetrachloro-1-pyrazoline are plotted on a relaxed PES scan of ϕ_s versus d_s in Figure 4.13. To understand the effect of substitution on dynamical pathways, we initiated 50 trajectories from **sos_Cl** in the forward and reverse directions with an E_{total} of 78.62 kcal mol^{-1}. 35/50 trajectories were found to be reactive i.e. they resulted in the formation of products, **Cl_cyp**. The different dynamical pathways followed during the trajectory simulations are

Figure 4.13: PES obtained by performing a relaxed scan of ϕ_s and d_s at the CASSCF(4,4)/6-31+G* level of theory. The MEPs are plotted on the PES with solid black lines.

given in Table 4.7. It can be seen that the majority of the trajectories, (11+16) follow the MEP **Cl_ts0** → **Cl_sos** → **Cl_cyp** (Figure 4.14). (5+2)/35 trajectories lead to the formation of **Cl_py** from **Cl_sos**, directly from **Cl_py/Cl_py′** and hence did not follow the MEP. Interestingly, one trajectory first reached **Cl_sos** from **Cl_py′**, and then lead to the formation of **Cl_cyp** via **Cl_ts1**. These observations point to contrasting dynamics followed in the chloro-substituted pyrazoline compared to 1-pyrazoline. Unlike the case of 1-pyrazoline, here the majority of the trajectories follow the MEP during the formation of product. In addition, we also find that all

Table 4.7: Pathways followed by the trajectories initiated from the **Cl_sos** region for 3,3,5,5-tetrachloro-1-pyrazoline

	Pathways	No. of trajectories
1.	**Cl_py → Cl_sos → Cl_cyp**	5
2.	**Cl_py′→ Cl_sos → Cl_cyp**	2
3.	**Cl_py→ Cl_ts0 → Cl_sos → Cl_cyp**	11
4.	**Cl_py′→ Cl_ts0 → Cl_sos → Cl_cyp**	16
5.	**Cl_py′→ Cl_sos → Cl_ts1 → Cl_cyp**	1

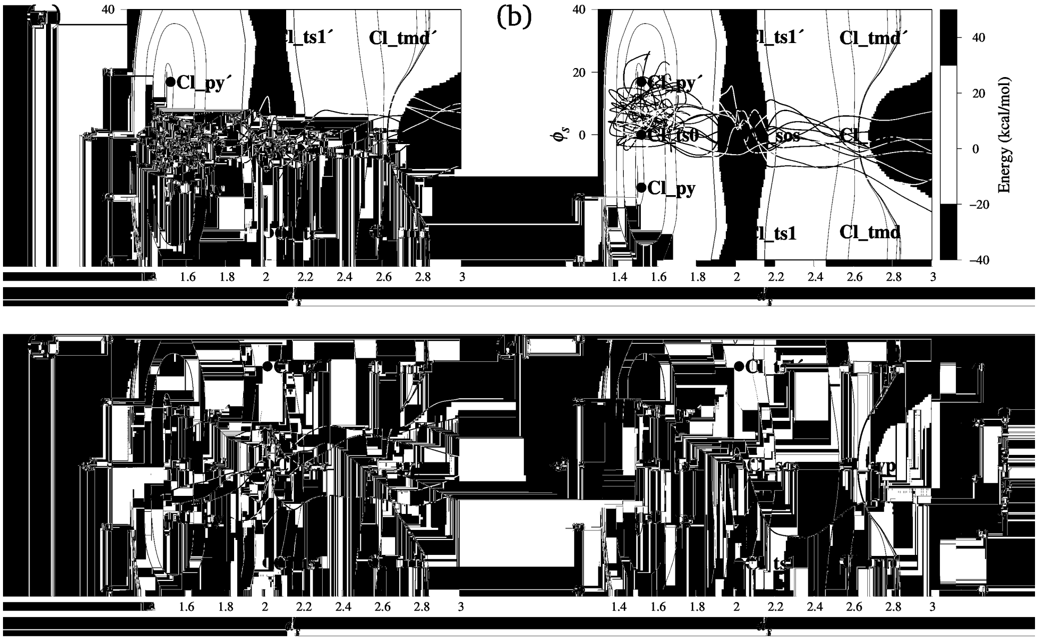

Figure 4.14: Different mechanistic pathways followed by the trajectories initiated from **Cl_sos**. The trajectories are plotted on a relaxed PES scan of ϕ_s versus d_s of 3,3,5,5-tetrachloro-1-pyrazoline.

35 trajectories lead to the formation of **Cl_cyp** with a retention of configuration, similar to the observations from 1-pyrazoline where the SOS served as a alternative pathway for the formation of products with retention of configuration. The non-statistical dynamics of the system can be understood from the negligible presence of other reactive pathways via **Cl_py/Cl_py′** from **Cl_sos**. However, a large number of trajectories need to be evaluated to obtain a clear picture.

4.4 Summary and Conclusions

The thermal denitrogenation of 1-pyrazoline and 3,3,5,5-tetrahalo-1-pyrazoline was studied using *ab initio* classical dynamics simulations. The denitrogenation of 1-pyrazoline was studied at higher energies available to the system (E_{total} = 130, 140, 150 kcal mol^{-1}) to understand the influence of second-order saddle on the reaction mechanisms. It was observed that the number of reactive trajectories increased with increase in E_{total} available to the system. The reaction followed both the synchronous and asynchronous mechanisms, with the former being the major pathway. In addition, with increase in E_{total}, the higher energy asynchronous pathway opened up although the **sos** energy is lower as compared to the asynchronous transition state and more number of trajectories followed the asynchronous path, hence indicating the non-statistical nature of the system. The SOS was also found to serve as an alternate pathway for the formation of **cyp** products with retention of configuration. Also, the majority of the trajectories did not follow the MEP and a major SI of configuration was observed for **cyp** products consistent with the experimental observations.

In case of 3,3,5,5-tetrachloro-1-pyrazoline, the **Cl_sos** was found to be only 2.5 kcal mol^{-1} above the transition state. The *ab initio* classical dynamics simulations revel that majority of the trajectories follow the MEP and directly close to give **Cl_cyp** with retention of configuration.

CHAPTER 5

MECHANISMS AND DYNAMICS OF THE THERMAL DENITROGENATION OF 2,3-DIAZABICYCLO[2.2.1]HEPT-2-ENE

5.1 Introduction

Thermal[116–124] and photochemical[125–131] denitrogenation of 2,3-diazabicyclo[2.2.1] hept-2-ene (**dbh**) resulting in bicyclopentane (**bcp**) has been well studied both experimentally and theoretically. Carpenter and coworkers[124] observed that the pyrolysis of 2,3-diazabicyclo[2.2.1]hept-2-ene-*exo*,*exo*-5,6-d2 produces bicyclo[2.1.0]pentane-*exo*,*exo*-2,3-d2 and bicyclo[2.1.0]pentane-*endo*, *endo*-2,3-d2, of which the *exo*-isomer is the major product and cyclopentene (**cpn**) is formed in traces, with the liberation of nitrogen gas (Scheme 5.1). The *exo*-**bcp** is formed as a result of inversion of configuration at both the carbon centers (the carbon bonded to nitrogen in **dbh**), leading to a double inversion of configuration. On the other hand, the *endo*-**bcp** is formed as a result of retention of configuration at both the carbon centers. They found that the ratio of the rate constants for the formation of *exo* and *endo* products (k_{exo}/k_{endo}) is ∼ 4.5 and does not show significant temperature dependence. Also, a decrease in this ratio was observed on going from gas phase to solution phase. Mishra and co-workers in 1966 studied the pyrolysis of various 3,5 substituted pyrazolines at a range of temperatures and estimated the activation energy for deazetization of **dbh** to be 36.9 ± 0.3 kcal mol^{-1}.[116] Kinetic studies showed that the thermal deazetization of **dbh** was a first order reaction and was found to be about 430 times faster than its acyclic analogue ($Me_2CHN{=}NCHMe_2$) at 250°C.[123]

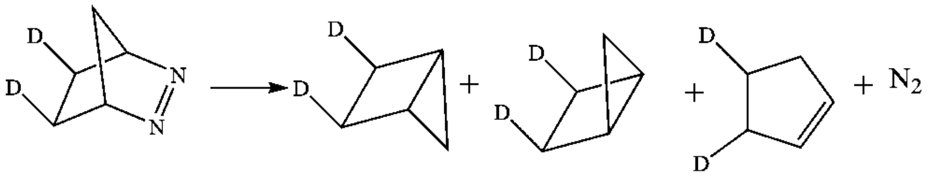

2,3-diazabicyclo[2.2.1]hept-2-ene-*exo,exo*-5,6-d2

bicyclo[2.1.0]pentane-*exo,exo*-2,3-d2

bicyclo[2.1.0]pentane-*endo,endo*-2,3-d2

cyclopentene-3,4-d2

Scheme 5.1: Schematic representation for the thermal denitrogenation reaction of **dbh**.

Various explanations have been proposed in the literature to explain the major double inversion of configuration observed.[132–134] Studies suggested that the reaction mechanism can either involve breaking of both the C-N bonds simultaneously (synchronous pathway) or one of the C-N bonds can break first followed by the other (asynchronous pathway). Bauer suggested that the synchronous denitrogenation would lead to the formation of vibrationally excited N_2.[135] This is because there is a large change in the N-N bond distance on going from **dbh** to N_2. However, experiments by Adams and coworkers showed that N_2 was formed with very less vibrational energy indicating that the denitrogenation followed an asynchronous pathway, involving the formation of a diazenyl biradical which can then form **bcp** or undergo H-atom shift to form **cpn**.[120] Computational studies by Robb and coworkers in 1998 using multireference wave function methods proposed that the deazetization of **dbh** can occur via both synchronous and asynchronous pathways.[125] Carpenter and coworkers studied the different reaction mechanisms for the denitrogenation of **dbh** using CASSCF and CASPT2 methods and proposed that the synchronous mechanism is more favourable as compared to the asynchronous pathway.[117] Houk and co-workers worked on a range of bicyclic azo compounds including **dbh** and investigated the one-bond, two-bond, and three-bond cleavage mechanisms possible during the pyrolysis of such compounds using various density functionals and multiconfigurational methods.[119] They suggested that, the synchronous pathway is lower in barrier and hence more favourable. It should be noted that, none of the studies reported thus far were able to identify the crucial transition state corresponding to the first C-N bond cleavage for the asynchronous denitrogenation pathway.

Substituents on the bridge head position of **dbh** were also found to play a key role in the mechanisms followed during deazetization reaction. Masuyama and coworkers[121] in 2005 studied the effect of the presence of electron donating and electron withdrawing substituents on the bridge head position using density functional theory. They found that the synchronous mechanism is more favoured when an electron donating group is present on the bridge head position whereas the asynchronous mechanism was favoured for reactions in which an electron withdrawing group was present on the bridge head position of **dbh**. However, within the computational methodology used, they were not able to locate many stationary points and hence were unable to map the complete potential energy profile for the reaction. Andres and coworkers in 2015 also studied the different mechanistic pathways for the deazetization of **dbh** and substituted **dbh** systems under the domain of quantum chemical topology and proposed that the denitrogenation of **dbh** via a synchronous mechanism is more feasible as compared to the asynchronous pathway.[122]

The studies reported this far on the mechanism of the deazetization of **dbh**, point to the formation of a cyclopentane-1,3-diyl diradical (**cpdr**), in the course of the reaction. The generation of a five-membered cyclic ring during the reaction introduces interesting features in the reaction mechanism. While a planar cyclopentane ring (D_{5h} symmetry) introduces negligible angle strain (the internal angles of a pentagon is 108°, which is quite close to the tetrahedral an-

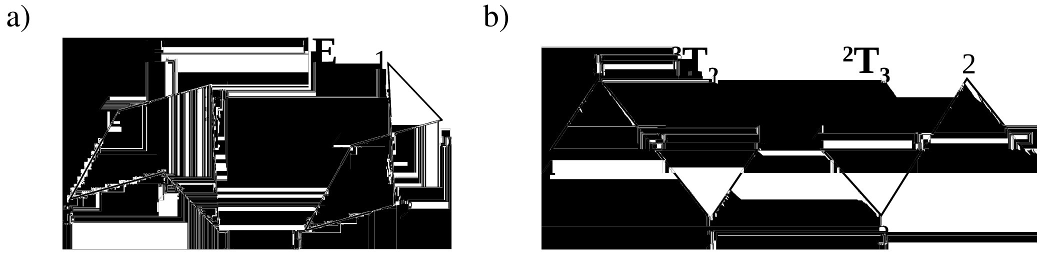

Figure 5.1: Different conformers of cyclopentane obtained due to the ring-puckering motion (a) envelope conformers (E_1 and ^1E isomer), (b) twisted conformers ($^3T_2$ and $^2T_3$ isomer).

gle of 109.45°), the presence of the H-atoms in an eclipsed conformation leads to considerable torsional strain in the planar molecule. This torsional strain can be minimized by ring puckering, hence leading to the formation of stable envelope and twisted conformations.[136–138] In the envelope isomer (C_s symmetry), four sp^3 hybridized C-atoms lie on a plane and the fifth C-atom lies either above or below the plane. On the other hand, in the twisted conformation (C_2 symmetry), three sp^3 hybridized C-atoms are present on a plane and the other two C-atoms are placed with one above and the other below the plane (Figure 5.1). Hence, a total of 20 different isomers of cyclopentane can be obtained. This makes up a complete pseudorotation cycle comprising of 20 isomers in case of a 5-membered cyclic ring.[139] To the best of our knowledge, a complete mechanistic pathway for the thermal deazetization of **dbh** is still not clear. In this work, we explore the various reaction pathways possible for the thermal deazetization of **dbh** using CASSCF and CASPT2 methods. The dynamics of the system was also studied using *ab initio* classical dynamics simulations to understand the atomic-level mechanism and product distribution.

5.2 Methodology

The different reaction pathways were mapped at the CASSCF(n,m)/6-31+G* level of theory where n and m represents the number of active electrons and active orbitals respectively. The active spaces used in this study are given in Table 5.1. The pictorial representation of the

Table 5.1: Active space used for CASSCF (*n*,*m*) calculations

(*n*,*m*)	**Active Orbitals**
(4,4)	$\sigma1$(C-N), $\sigma2$(C-N), $\sigma1^*$(C-N), $\sigma2^*$(C-N)
(12,12)	$\sigma1$(C-N), $\sigma2$(C-N), $\sigma3$(C-C), $\sigma4$(C-C) $\sigma5$(C-C),$\sigma6$(C-C) $\sigma1^*$(C-N), $\sigma2^*$(C-N), $\sigma3^*$(C-C), $\sigma4^*$(C-C) $\sigma5^*$(C-C),$\sigma6^*$(C-C)

active orbitals are given in Figure 5.2. The potential energy profile for the reaction was also investigated at the DFT level using different density functionals such as UB3LYP, M06-2X, and at the UMP2 level. The calculations were performed using Gaussian16[70], MOLPRO[89], and NWChem[88] software packages. The stationary points on the PES were characterized by computing the normal mode eigen values. The IRC[68] was followed on either sides of the transition state to connect to the respective intermediates. The effect of basis sets was investigated by using various 6-31+G*, 6-311+G(2d,p), cc-pVDZ, and cc-pVTZ at the CASSCF(4,4) level of theory.[140–143] To account for the dynamic correlation, single-

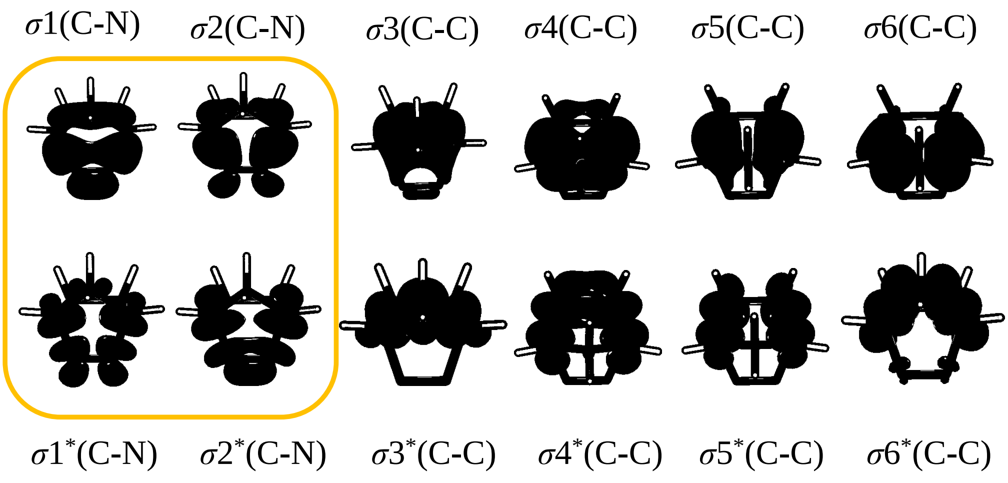

Figure 5.2: Active orbitals used in the CASSCF calculations. The box indicates the orbitals used in the (4,4) active space.

point CASPT2(4,4)//CASSCF(4,4) and CASPT2(12,12)//CASSCF(12,12) calculations were also performed.

To understand the dynamics, the time evolution of the system was studied using *ab initio* classical trajectory simulations. A total of 500 trajectories were initiated from the reactant **dbh** molecule with the initial coordinates and momenta sampled using the microcanonical normal mode sampling technique.[14] The total energy available to the reactant **dbh** was calculated by assuming a Boltzmann distribution of states at the asynchronous transition state (**ts1a**) as,

$$\Delta E_{\text{total}} = \Delta E_{\text{a}} + \Delta E_{\text{vib}} + \Delta E_{\text{rot}} + RT \tag{5.1}$$

where, ΔE_{a} is the energy of **ts1a** relative to the reactant, ΔE_{vib} and ΔE_{vib} correspond to the average vibrational and rotational energy available for **ts1a** at 453.15 K (experimental temperature), and RT corresponds the energy along the reaction coordinate. The E_{total} at 453.15 K was calculated to be 127.38 kcal mol^{-1}. The forces on the system were computed on-the-fly at the CASSCF(4,4)/6-31+G* level of theory.[91] The equations of motion were integrated by using the velocity-Verlet algorithm.[144] In addition, a set of 50 trajectories each were also integrated from the synchronous (**ts1**) and asynchronous (**ts1a**) transition states for the denitrogenation of **dbh** with an E_{excess} of 91.28 and 90.18 kcal mol^{-1} respectively (Table 5.2). Here,

$$\Delta E_{\text{excess}} = \Delta E_{\text{total}} - \Delta E_{\textbf{ts1/ts1a}} \tag{5.2}$$

Table 5.2: Summary of the initial conditions for the trajectory simulations from different regions.

Trajectories initiated from	ΔE_{total}	ΔE_{excess}	Total trajectories initiated
dbh	127.38	-	500
ts1	127.38	91.28	50
ts1a	127.38	90.18	50

The trajectories were integrated in the forward and reverse directions for a given set of initial conditions chosen using the microcanonical normal mode sampling technique. The forward and backward trajectories were stitched together to get a complete trajectory i.e. **dbh** → **ts1/ts1a** → **P**. The initial coordinates and the magnitude of conjugate momenta for the forward and reverse trajectories were same. However, if p_i^f defined the sign of the momenta for i^{th} component in the forward direction, $-p_i^f$ defined the direction of momenta for the i^{th} component in the reverse direction. The important geometrical parameters were followed as a function of time to characterize the different reaction pathways followed and product distribution obtained during the reaction.

5.3 Results and Discussions

5.3.1 Potential Energy Profile

The molecular structure of **dbh** is shown in Figure 5.3. The **dbh** molecule has a C_s symmetry with a sigma plane passing through the methylene (-CH$_2$) bridge. The five C-atoms in **dbh** form an envelope isomer of the cyclopentane ring. The N$_2$ group is attached to this envelope isomer at the 2,4 positions, hence forming the bicyclic moiety. The atom labels used in the analysis and important geometrical parameters are also given in Figure 5.3. As discussed above, the thermal deazetization of **dbh** can occur either via simultaneous breaking of both the C-N bonds or one of the C-N bonds can break leading to the formation of a diazenyl diradical, **dadr** which further leads to the second C-N bond dissociation. The different stationary points along

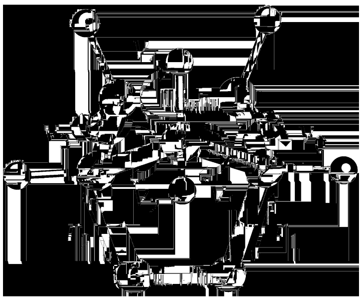

Figure 5.3: Atom labels and important geometrical parameters of **dbh** used in further analysis.

the synchronous and asynchronous pathways were calculated at the CASSCF(4,4)/6-31+G* and CASSCF(12,12)/6-31+G* levels of theory. The dynamical correlation was included by considering the CASPT2(4,4) and CASPT2(12,12) methods (Table 5.3). In addition, the effect of basis sets were investigated using the 6-31+G*, 6-311+G(2d,p), cc-pVDZ, and cc-pVTZ basis sets and CASSCF(4,4) method (Table 5.4). We can see that CASSCF(4,4)/6-31+G* level of theory represents the PES reasonably well capturing the overall features consistent with the high-level CASPT2(12,12)/6-31+G* method. The CASSCF(4,4)/6-31+G* energies deviate less that 5 kcal mol^{-1} from the CASPT2(12,12)/6-31+G* level except for **cpdr**. A similar deviation in the diradical energies was seen in 1-pyrazoline.[112] Here, we describe the different pathways mapped at the CASSCF(4,4)/6-31+G* level of theory.

Table 5.3: Energetics of the reaction at CASSCF(4,4)/6-31+G* and CASSCF(12,12)/6-31+G* level of theory. The CASPT2(*n*,*m*) calculations were performed by doing a single point calculation on the CASSCF(*n*,*m*) optimized geometries. The energies are reported with respect to **dbh** in kcal mol^{-1}

Stationary Points	CASSCF(4,4)	CASPT2(4,4)	CASSCF(12,12)	CASPT2(12,12)
dbh	0.0	0.0	0.0	0.0
ts1	36.1	36.3	37.8	38.2
cpdr	-1.0	27.1	6.5	26.02
ts1a	37.2	38.3	40.8	39.2
int2a	36.0	37.9	39.9	38.7
ts2a	37.1	40.5	41.3	41.6
ts1b	36.2	38.2	40.2	39.0
int2b	34.5	37.1	38.4	37.8
ts2b	36.5	41.0	40.8	42.1
ts1c	36.3	38.3	40.1	39.0
ts2c	37.0	40.4	41.2	41.6
inteq2	36.0	39.0	39.6	39.8
ts1e	36.9	38.9	40.3	39.8
inteq1	35.2	36.9	38.4	37.2
ts2e	36.5	38.4	-	-
ts1f	36.2	38.8	41.5	41.0
inteq3	34.3	37.2	38.0	37.9
ts2f	36.4	40.0	39.3	40.2

(i) Synchronous Denitrogenation Pathway

Table 5.4: Effect of basis sets on the energetics of stationary points at the CASSCF(4,4) level

Stationary Points	6-31+G*	6-311+G(2d,p)	cc-pVDZ	cc-pVTZ
ts1	36.1	35.2	34.0	35.2
cpdr	-1.0	-3.6	-2.8	-
ts1a	37.2	36.9	36.3	37.0
int2a	36.0	35.9	35.3	36.0
ts2a	37.1	36.5	36.1	36.6
ts1b	36.2	36.2	37.9	36.3
int2b	34.5	34.4	34.0	34.6
ts2b	36.5	35.9	35.5	36.0
ts1c	36.3	36.2	35.6	36.3
ts2c	37.0	36.4	36.0	36.5
inteq2	36.0	35.9	35.6	36.0
ts1e	36.9	36.8	36.4	36.8
inteq1	35.2	35.0	34.7	35.2
ts2e	36.5	35.9	35.8	36.0
ts1f	36.2	36.1	35.8	36.2
inteq3	34.3	34.4	34.1	34.5
ts2f	36.4	35.9	36.0	36.0

The simultaneous dissociation of the two C-N bonds in **dbh** leads to the formation of **cpdr** via transition state **ts1**. The two C-N bonds stretch simultaneously on going from **dbh** (r_{CN} = 1.52 Å) to **ts1** (r_{CN} = 2.08 Å) with a barrier of $\sim$ 36 kcal mol^{-1} (Figure 5.4). The barrier is in close agreement with the experimental activation barrier obtained from the kinetic studies.[116] The normal mode eigenvector for **ts1** along the reaction coordinate correspond to the symmetric C-N stretching vibration with ν = 695.2i cm^{-1}. The IRC from **ts1** connects to **dbh** on one side and **cpdr** on the other side. The diradical, **cpdr** formed during the reaction is stabilized by 1 kcal mol^{-1} with respect to **dbh**. A partial geometry optimization was performed for **cpdr** (**cpdr** and N_2 were kept at a distance of 10 Å) to maintain the size consistency of the system. In this case, the two p orbitals present on the two C-atoms (C4 and C2) of **cpdr** and π and π* orbitals of N_2 were accounted in the active space. Inclusion of the dynamic correlation at the CASPT2(4,4)//CASSCF(4,4) has a minor effect as the barrier increases only by 0.2 kcal mol^{-1} (i.e. 36.1 to 36.3 kcal mol^{-1}). At the CASSCF(12,12) level, the synchronous denitrogenation barrier was found to be 37.8 kcal mol^{-1}. From **cpdr**, a ring-closure by C-

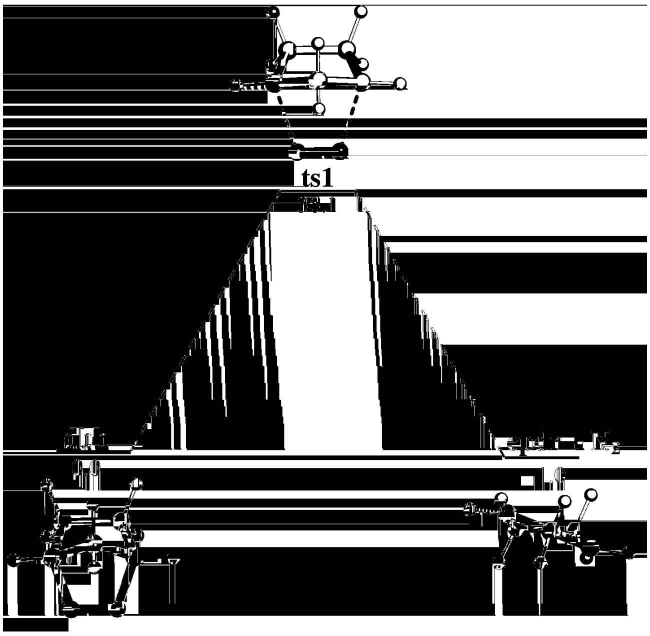

Figure 5.4: Potential energy profile for the synchronous denitrogenation of **dbh** at the CASSCF(4,4)/6-31+G* level of theory

C bond formation between the bridged C-atoms results in bicyclopentane **bcp** product. The C-C bond formation in **cpdr** takes place via transition state **ts1_ret** to give the product **bcp** with retention of configuration, **bcp_ret**, and the C-C bond formation via **ts1_di** forms **bcp_di** i.e. **bcp** with a double inversion of configuration (Figure 5.5). The barrier for the C-C bond formation for the formation of both **bcp_di** and **bcp_ret** was found to be 2.2 kcal mol^{-1}. The **bcp** products were stabilized by $\sim$ 27 kcal mol^{-1} with respect to **dbh**.

(ii) Asynchronous Denitrogenation Pathway

In contrast to the synchronous pathway, the asynchronous denitrogenation of **dbh** leads to the formation of diazenyl diradical **int2a** via the transition state **ts1a**. The energy of **ts1a** was found to be 37.2 kcal mol^{-1} at the CASSCF(4,4)/6-31+G* level of theory. The IRC plot leading to the formation of **dbh** and **int2a** on either sides from **ts1a** is given in Figure 5.6. It should be noted that none of the earlier reports were able to determine a transition state corresponding to the stepwise C-N bond cleavage of **dbh**. From **int2a** the dissociation of

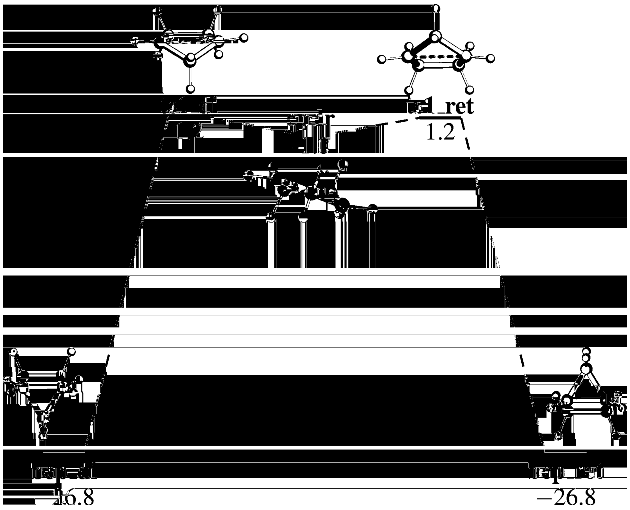

Figure 5.5: Potential energy profile for the formation of **bcp_di** and **bcp_ret** from **cpdr** mapped at the CASSCF(4,4)/6-31+G* level of theory. The energies are reported with respect to **dbh**.

the second C-N bond results in **cpdr** via **ts2a** with a barrier of ~1 kcal mol^{-1}. However, an

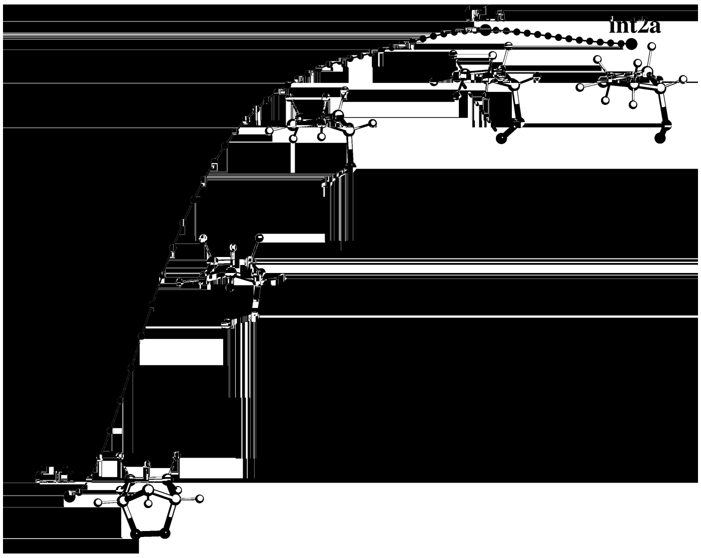

Figure 5.6: IRC plot connecting **dbh** and **int2a** via transition state **ts1a**.

anti-clockwise rotation of the N_2 group about the C-N bond in **int2a** leads to the formation of another conformational isomer of **dadr**, **int2b** via the transition state **ts1b**. Dissociation of the second C-N bond from **int2b** via transition state **ts2b** leads to the formation of **cpdr**.

The barrier for the C-N bond dissociation from intermediate **int2b** is $\sim$ 2 kcal mol^{-1}. A similar anti-clockwise torsional motion of the C-N bond in **int2b** leads to the formation of the intermediate **int2c** via **ts1c**. However, **int2c** could not be optimized and was obtained by doing a single-point calculation on the last point of the IRC performed from **ts1c**. The C-N bond dissociation from **int2c** yields **cpdr** via **ts2c** with a barrier of $\sim$1 kcal mol^{-1}. The potential energy profile for the asynchronous pathway discussed above is given in Figure 5.7. It should be noted that, the barriers for the C-N bond torsion is very less $\sim$1 kcal mol^{-1} and

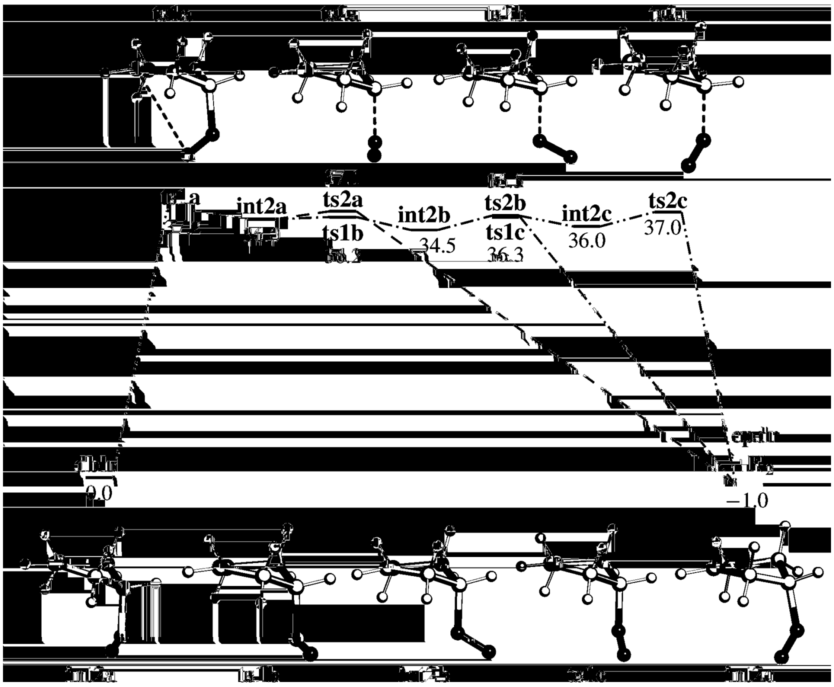

Figure 5.7: Potential energy profile for the asynchronous denitrogenation of **dbh** at the CASSCF(4,4)/6-31+G* level of theory. The structure **int2c** was obtained from the last point of the IRC performed from **ts1c**.

hence different conformational isomers of **dadr** can be obtained.

The five-membered cyclic **dadr** formed during the denitrogenation of **dbh** can undergo pseudorotation and exist in different twisted and envelope isomeric forms. Pseudorotation can be described by two parameters - the maximum puckering amplitude ν_{max} and the phase angle

P, given by[139]

$$\tan P = \frac{\nu_4 - \nu_3 + \nu_1 - \nu_0}{2\nu_2(\sin 36^\circ + \sin 72^\circ)} \tag{5.3}$$

$$\nu_{max} = \frac{\nu_2}{\cos P} \tag{5.4}$$

A plot of the maximum puckering amplitude and the phase angle of the five-membered ring gives rise to the pseudorotation cycle. Hence, depending upon the position of the C-atoms, a total of 20 different isomers can be obtained due to pseudorotation of the cyclopentane ring (Figure 5.8). The different stationary points obtained can be plotted on the pseudorotation cycle to characterize various twisted and envelope isomers (Figure 5.9). Calculation of the P and ν_{max} reveal that the **dadr** intermediates **int2a** and **int2b** exist as $\mathbf{^1E}$ isomers with distinct ∠C3C2N7N6 torsions. In addition, conformational isomers corresponding to the twisted forms $\mathbf{^1T_2}$ were also located (Figure 5.9). The energy difference between the $\mathbf{^1T_2}$ and $\mathbf{^1E}$ isomers was found to be very less (< 0.5 kcal mol^{-1}). A relaxed scan by fixing ∠HC3C4H for **int2a** at the CASSCF(12,12) level of theory (Figure 5.10), revealed the barrierless interconversion between the $\mathbf{^1T_2}$ and $\mathbf{^1E}$ isomers, in accordance with the previously reported studies by Houk and co-workers.[119] The potential energy profile for the asynchronous path including

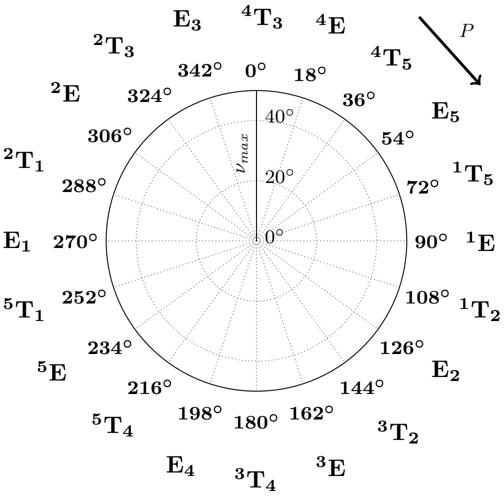

Figure 5.8: Schematic representation of the pseudorotation cycle for characterization of different envelope and twisted isomers formed due to the ring-puckering motion of a five-membered cyclic ring.

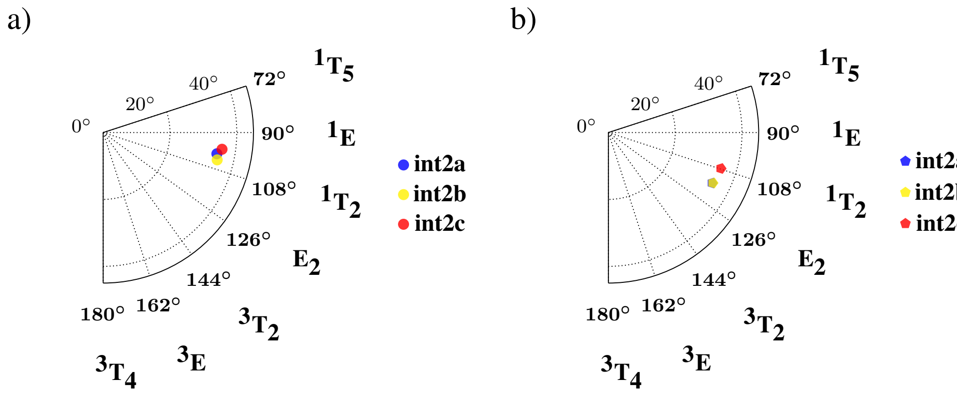

Figure 5.9: Two classes of diradicals obtained for the asynchronous denitrogenation of **dbh**, plotted on the pseudorotation cycle (a) the envelope $\mathbf{^1E}$ isomers and (b) the twisted $\mathbf{^1T_2}$ isomers.

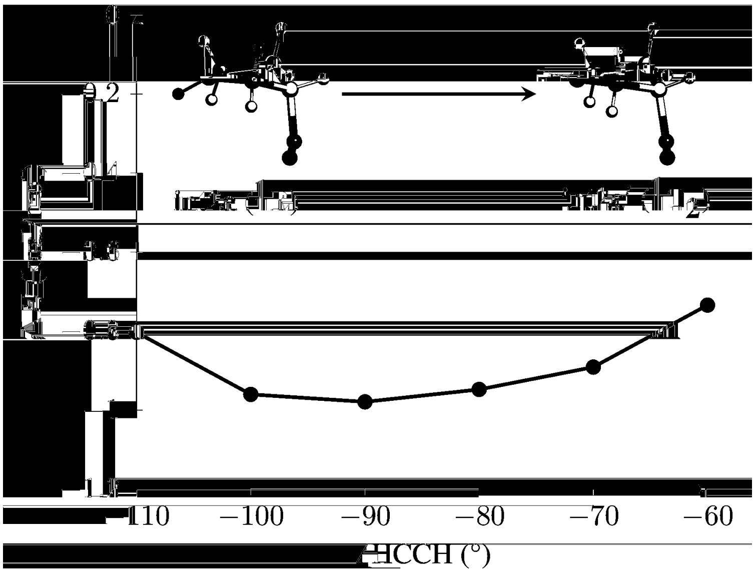

Figure 5.10: Variation of energy as a function of ∠HC3C4H (color coded as blue) by performing a relaxed scan at the CASSCF(12,12)/6-31+G* level of theory. The ∠HC3C4H was fixed and the energy was minimized by relaxing the 3N-7 degrees of freedom.

the intermediates **int2a′** and **int2b′** that correspond to the twisted $\mathbf{^1T_2}$ form was also mapped at the CASSCF(4,4) level of theory (Figure 5.11).

It should be noted that multiple envelope and twisted forms of **dadr** are possible. For example, the isomers **int2a**, **int2b**, **int2c**, **int2a′**, **int2b′**, and **int2c′**, all span the $\mathbf{^1E}$ and $\mathbf{^1T_2}$ region of the pseudorotation cycle having N_2 group in the axial positions. In addition, isomers having N_2 group in the equatorial position are also possible. The energy profile corresponding to such isomer is given in Figure 5.12. It is worth pointing out that some of the **dadr** isomers allow the formation of bicyclopentane with double inversion of configuration, **bcp_di** by a simultaneous C-N bond breaking and C-C bond formation between the bridged C-atoms as illustrated in Figure 5.12, i.e. **inteq3** → **ts2f** → **bcp_di** and **inteq1** → **ts2e** → **bcp_di**.

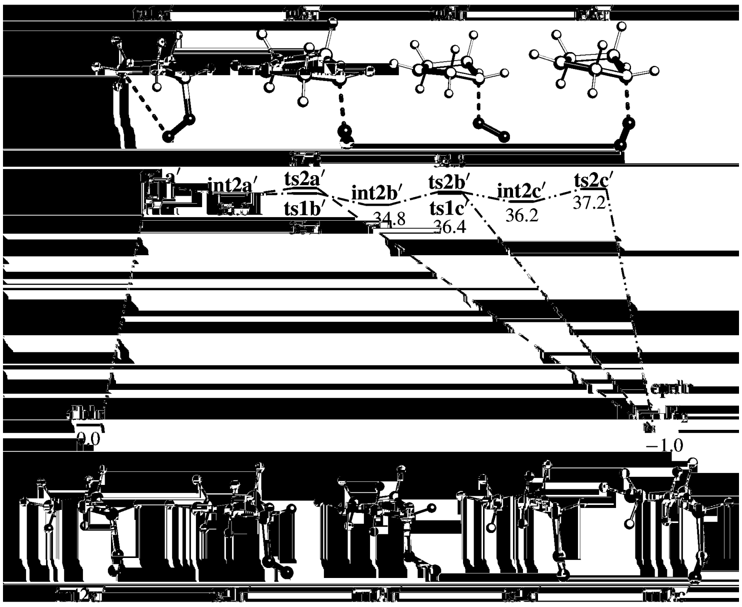

Figure 5.11: Potential energy profile for the asynchronous denitrogenation of **dbh** for $^{\mathbf{1}}\mathbf{T_2}$ isomers at the CASSCF(4,4)/6-31+G* level of theory.

(iii) DFT and UMP2 Methods

It is interesting to see how the energetics would change if DFT and UMP2 methods are used to investigate the synchronous and asynchronous pathways for the denitrogenation of **dbh**. The potential energy profiles for the two pathways were mapped at UB3LYP, M06-2X, and UMP2 methods and 6-31+G* basis set. In contrast to the PES obtained at the CASSCF(4,4)/6-31+G* level of theory, the UB3LYP and M06-2X methods show that the synchronous denitrogenation pathway is concerted with simultaneous C-N bond breaking and [3,2] H-atom shift to form **cpn** and N_2 via transition state **tsa** (Figure 5.13). The barrier for this concerted synchronous

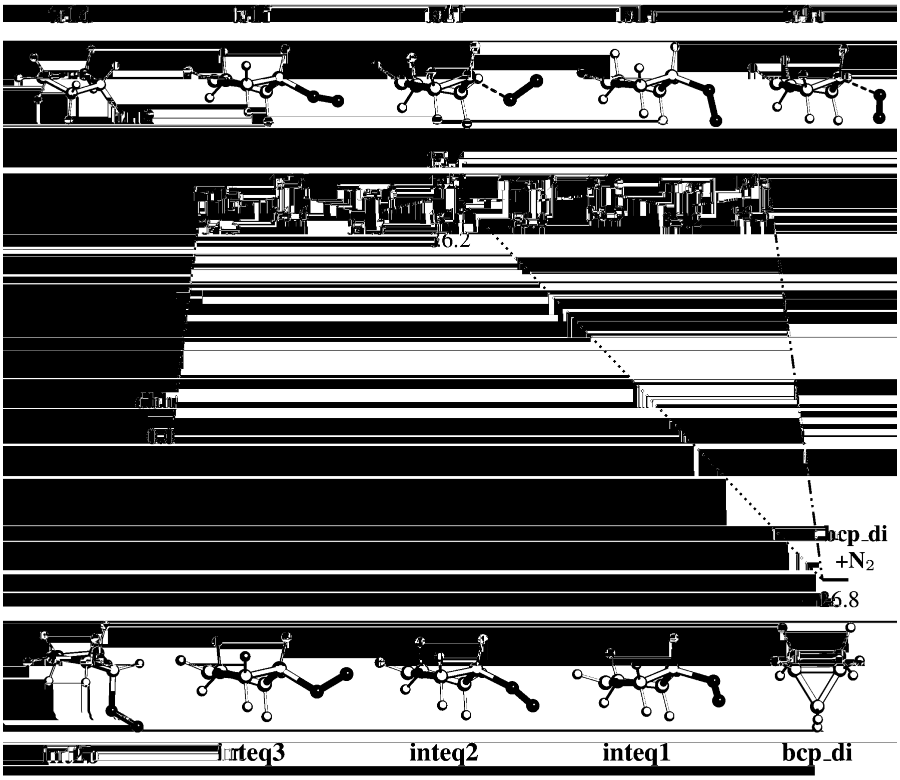

Figure 5.12: Potential energy profile for the formation of **bcp_di** at the CASSCF(4,4)/6-31+G* level of theory

denitrogenation was found to be 48.12 and 55.59 kcal mol^{-1} at the UB3LYP/6-31+G* and M06-2X/6-31+G* level of theories respectively. Also, the asynchronous pathway (both using UB3LYP and M06-2X methods) involves the formation of an intermediate, **intb** due to the dissociation of one of the C-N bonds in **dbh** via **tsb** with a barrier of 63.34 and 78.29 kcal mol^{-1} using the UB3LYP and M06-2X methods respectively. Simultaneous dissociation of both the C-N bonds in **intb** leads to the formation of **cpn** and N_2 via transition state **tsc**. The barrier for the second C-N bond cleavage was found to be lower as compared to the first C-N bond dissociation, calculated at the respective level of theories (Table 5.5). In contrast, the synchronous pathway lead to the formation of **cpdr** at UMP2/6-31+G* level of theory similar to the CASSCF method. However, in this case, the diradical **cpdr** was found to be less stable as compared to **dbh** ($\sim$ 39 kcal mol^{-1} higher in energy relative to **dbh**). Also, we could not locate

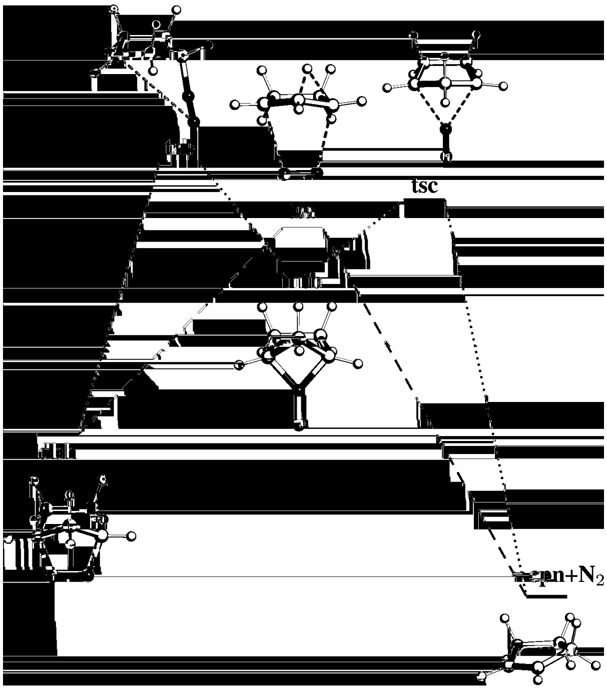

Figure 5.13: Schematic representation of potential energy profile for the denitrogenation of **dbh** using UB3LYP and M06-2X methods and 6-31+G* basis set. The relative energies at the two level of theories are given in Table 5.5.

Table 5.5: Energetics at the UB3LYP, M06-2X and UMP2 level of theory for different denitrogenation pathways of **dbh**

Stationary Point	UB3LYP	M06-2X	UMP2
tsa	48.12	55.59	39.90
tsb	63.34	78.29	-
intb	40.08	42.75	46.62
tsc	54.81	65.03	50.77
cpn+N$_2$	-37.81	-33.28	-
cpdr+N$_2$	-	-	39.51

any transition state corresponding to the first C-N bond breaking at the UMP2/6-31+G* level of theory. It was also found that DFT functionals and UMP2 methods tend to overestimate the reaction barrier.

(iv) Formation of Cyclopentene

Experimentally, the denitrogenation of **dbh** also yielded **cpn** (in traces) as one of the products.

Here, we mapped the pathways for the formation of **cpn** at the CASSCF(4,4)/6-31+G* level of theory. Cyclopentene can be formed either from **cpdr** or **bcp**. To maintain the size consistency of the system, N_2 molecule was fixed at a distance of 10 Å from **cpn** and **bcp**. The potential energy profiles for both the pathways are presented in Figure 5.14. An [3,4] H-atom shift in **cpdr** leads to the formation of **cpn** via transition state **ts1i**. The barrier for this H-atom rearrangement was found to be 27.7 kcal mol^{-1} with respect to **cpdr**. In contrast, the formation of **cpn** from **bcp** was found to be a two step process. An [2,4] H-atom rearrangement in **bcp** leads to the formation of a carbene intermediate **int1h** via the transition state **ts1h**. Further, [3,2] H-atom shift from **int1h** forms **cpn** via **ts2h**. The barriers for the [2,4] and [3,2] H-atom shift were found to be 67.6 and 17.6 kcal mol^{-1} respectively.

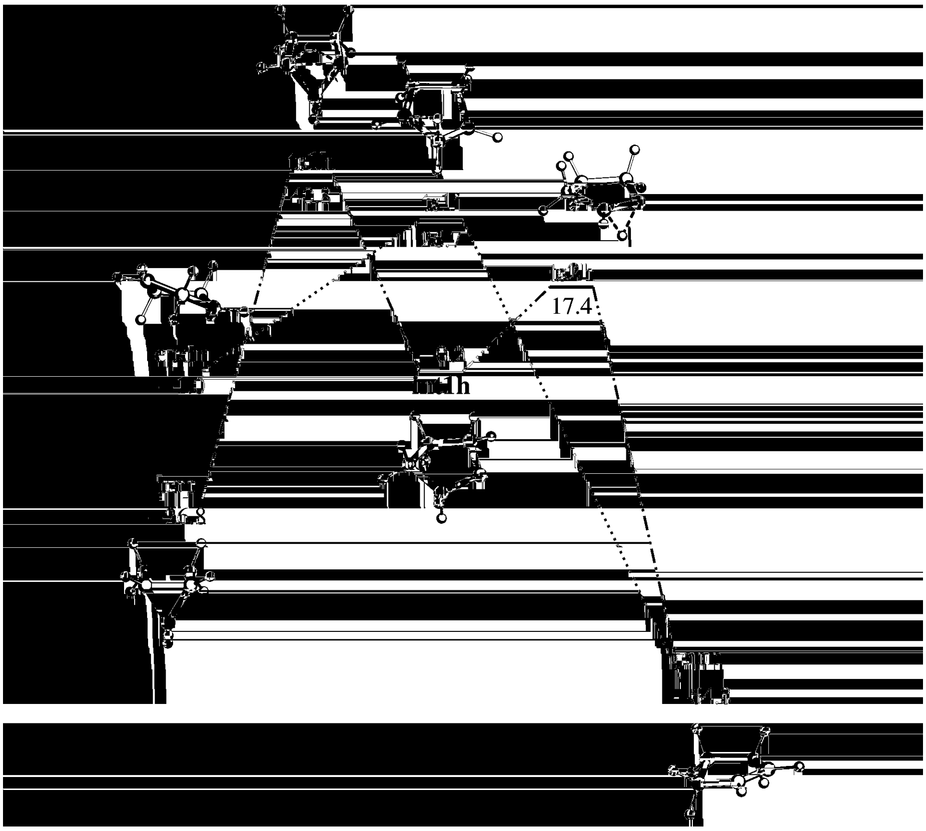

Figure 5.14: Potential energy profile for the formation of cyclopentene, **cpn** from **cpdr** and **bcp** via H-atom shift. The energies (kcal mol^{-1}) are reported with respect to **dbh**.

5.3.2 *Ab initio* Classical Dynamics Simulations

A. Trajectories Initiated from dbh

To understand the dynamics of the reaction, 500 trajectories were initiated from the reactant **dbh** region with a total energy of 127.38 kcal mol^{-1}. The trajectories were integrated for a total of 3 ps each. Out of the 500 trajectories initiated, 30 were found to be reactive i.e. 30 lead to the formation of **bcp** with a retention or double inversion of configuration or formed **cpdr**. Different internal coordinates of **dbh** were followed as a function of time to understand the pathways followed and the stereochemistry of the products obtained during the reaction.

(i) Synchronous vs Asynchronous Pathway

As stated earlier, the denitrogenation of **dbh** can either follow the synchronous or asynchronous denitrogenation pathway. To characterize these reactive trajectories based on the pathways followed during the reaction, the two C-N bond distances were followed as a function of time. A synchronous denitrogenation pathway was characterized if both the C-N bonds dissociation occurs within one vibrational period of the symmetric C-N stretch of **dbh** i.e. the two C-N bond distances cross the value of 2.7 Å within 42 fs with respect to each other. The value of 2.7 Å corresponds to the upper limit of the transition state region (**ts1** region). Else, the trajectory was said to follow an asynchronous denitrogenation pathway. To identify the transition state region, 50 trajectories were sampled at **ts1** with fixed E_{excess} calculated at 453.15 K. The C2-N7 (r_1) and C4-N6 (r_2) distances of the initial coordinates of the sampled trajectories were then plotted to identify the **ts1** region (Figure 5.15). The C-N bond dissociation criteria of 2.7 Å was chosen such that it corresponds to the trajectory leaving the transition state region.

Of the 30 reactive trajectories, 16 followed the synchronous pathway whereas 14 followed the asynchronous denitrogenation pathway. Three sample trajectories, labelled **TrajA**, **TrajB**, and **TrajC** showing the variation of r_1 and r_2, ν_d, and ring-puckering parameters during the course of the trajectory are given in Figure 5.16. In **TrajA**, we can see that at t = 0, both r_1

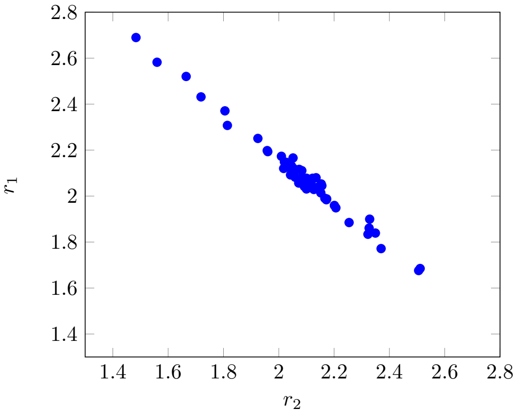

Figure 5.15: The initial coordinates r_1 and r_2 (in Å) for the 50 trajectories sampled at **ts1** for E_{total} calculated at 453.15 K.

and r_2 are around the equilibrium C-N bond distances. As time progresses, the two C-N bond distances oscillate around 1.5 Å, and increase $\sim$ 600 fs ultimately leading to the dissociation of the two C-N bonds. The time interval between the dissociation of the two C-N bonds was found to be $<$ 42 fs, hence this trajectory is said to follow the synchronous denitrogenation pathway. On the contrary, in **TrajB** both the C-N bonds initially oscillate about the equilibrium C-N bond distances. Then, one of the C-N bonds dissociate at $\sim$ 1800 fs followed by the dissociation of the second C-N bond after a time interval of more than 42 fs. Hence, **TrajB** is considered as following the asynchronous denitrogenation path. In **TrajC**, both the C-N bonds dissociate $\sim$ 2500 fs, within a time interval of 42 fs. Hence, **TrajC** is also said to follow the synchronous pathway.

The plot for all the trajectories following synchronous and asynchronous paths are shown with r_1 vs r_2 in Figure 5.17. For the trajectories following the synchronous pathway, it can be seen that both the C-N bonds dissociate simultaneously, hence taking a diagonal path. On the contrary, for the trajectories following the asynchronous pathway, first one of the C-N bonds break and the other oscillates about the mean C-N bond length. Later, the other C-N bond breaks leading to the formation of the product.

(ii) Product Distribution and Formation of Diradicals

To account for the product distribution i.e. **bcp_ret** or **bcp_di** formed during the reaction, we monitored $\nu_d = (\nu_1\text{-}\nu_2)/2$ as a function of time. The reactant **dbh** has a positive ν_d value (57.9°) with the methylene (-CH_2) group above the plane containing the four C atoms. Hence

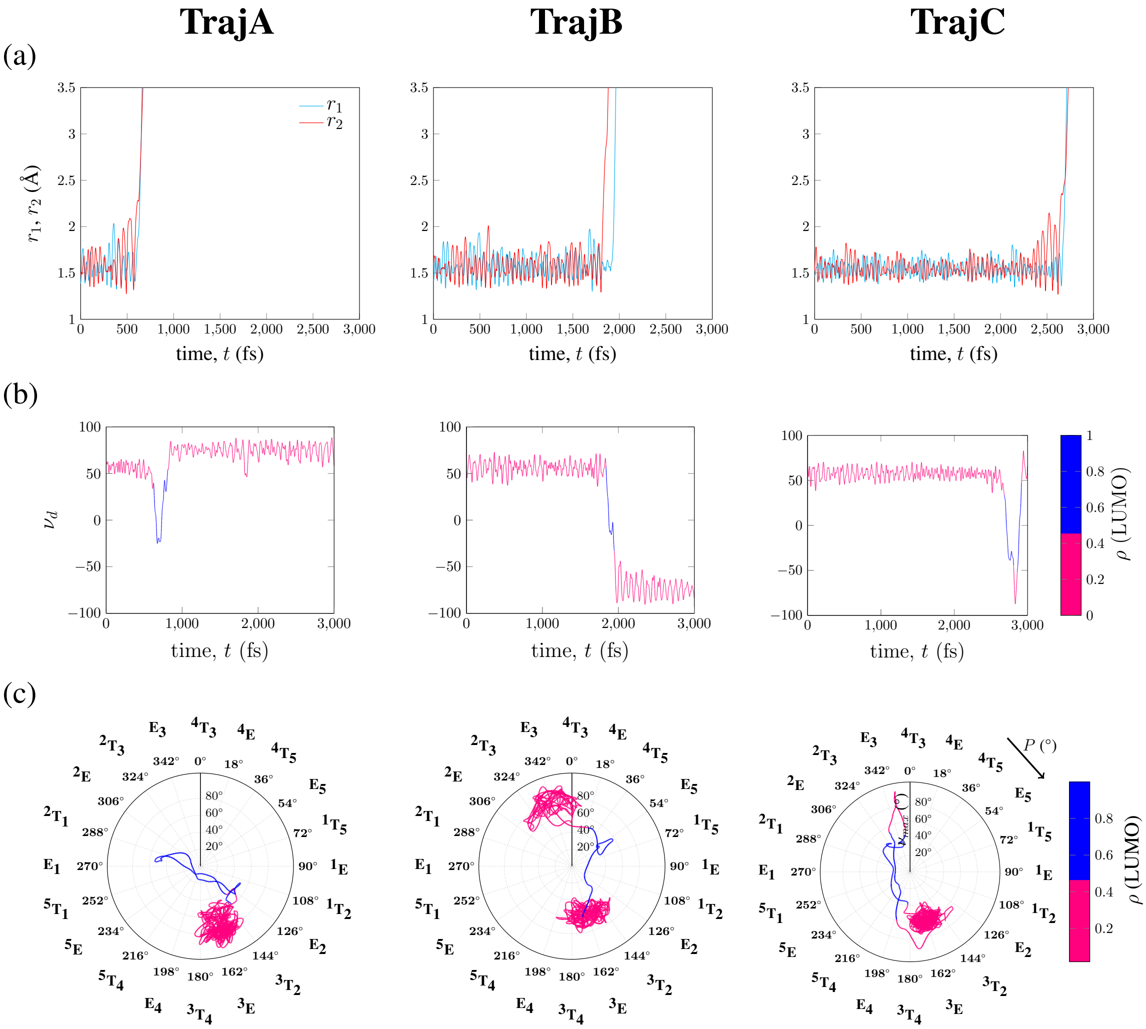

Figure 5.16: Representative trajectories: **TrajA**, **TrajB**, and **TrajC**, showing (a) the evolution of the two C-N bond distances r_1 and r_2 with time. **TrajA** and **TrajC** follow the synchronous denitrogenation pathway, whereas **TrajB** follows the asynchronous pathway, (b) the evolution of $\nu_d = (\nu_1\text{-}\nu_2)/2$ with time. The color bar represents the electron density (ρ) of LUMO. As the trajectory progresses with time, a diradical ($\rho > 0.45$, depicted by blue color) is formed and then C-C bond formation between the bridged C-atoms leads to the formation of **bcp**. **TrajA** and **TrajB** show the formation of **bcp** with retention and double inversion of configuration respectively. **TrajC** shows isomerization between **bcp_di** and **bcp_ret**, (c) the formation of different envelope and twisted isomers during the reactions.

during the formation of **bcp_ret**, the positive sign of v_d will be retained whereas formation of **bcp_di** will lead to an inversion in the sign of v_d. To investigate the diradical formed during the reaction, the LUMO electron densities (ρ) were monitored as a function of time. A ρ value > 0.45 represents the diradical. When the product is said to be formed, the HOMO and LUMO electron densities oscillate around ~ 2 and ~ 0 respectively. Sample trajectories showing formation of diradical during the integration time of 3 ps are shown in Figure 5.18.

Sample trajectories showing retention and double inversion of configuration during the formation of **bcp** products are shown in Figure 5.16(b). The colorbar shows the electron density in the LUMO, ρ(LUMO). The blue color indicates the formation of a diradical during the reaction. We can see that, in **TrajA** the v_d starts at a positive value of $\sim 58°$, and ρ(LUMO) is ~ 0. As time progresses, ρ(LUMO) increases, leading to the formation of a diradical. This diradical then undergoes ring-closure to form **bcp_ret** (since the v_d is still positive). On the contrary, in **TrajB** the v_d starts at a positive value and oscillates at the equilibrium value till $\sim$ 1.9 ps. These oscillations are then followed by the formation of a diradical, which then forms the product **bcp**. The trajectory leads to the formation of **bcp_di** since the v_d changes

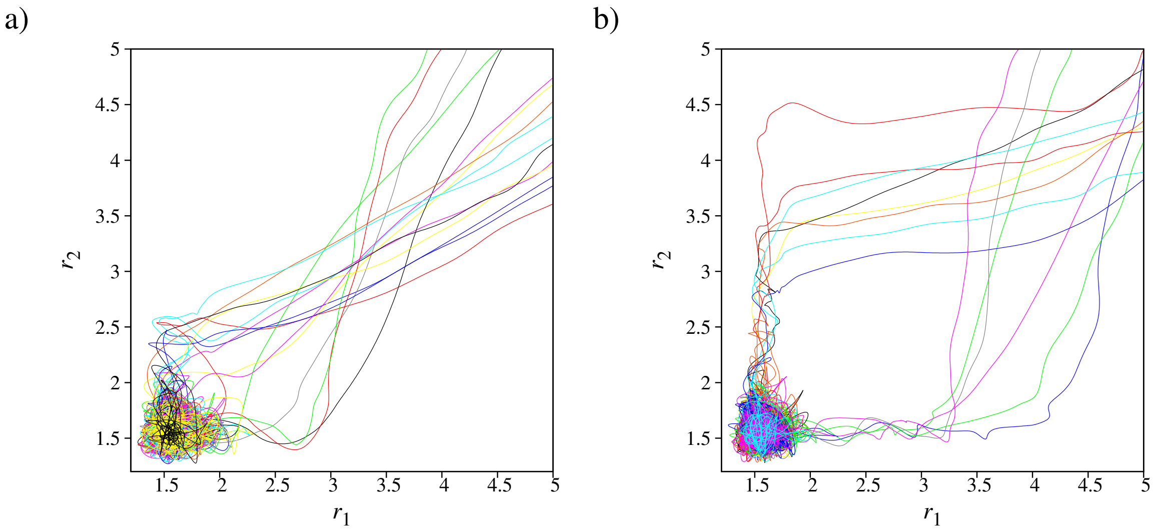

Figure 5.17: Plot of coordinates r_1 versus r_2 for trajectories following (a) synchronous, and (b) asynchronous denitrogenation pathways. The distances r_1 and r_2 are in Å.

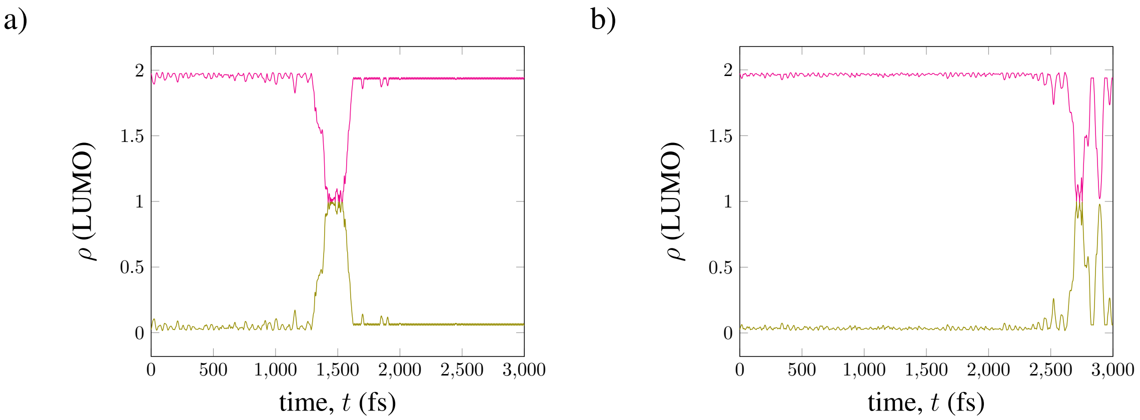

Figure 5.18: Two sample trajectories (a) and (b) showing formation of diradicals during the integration time of 3 ps. The olive and pink colors represent the variation of electron densities in the LUMO and HOMO respectively as a function of time.

from positive to a negative value during the formation of product. In addition, we also observed isomerization between **bcp_di** and **bcp_ret** in the trajectory simulations. A sample trajectory showing such isomerization event is given in Figure **TrajC** of 5.16(b). This trajectory first leads to the formation of product **bcp_di**. The bicylopentane product then undergoes ring-opening via C-C bond dissociation, leading to the formation of **cpdr**. Further C-C bond formation in **cpdr** results in **bcp_ret**.

Twenty-two out of the thirty reactive trajectories lead to the formation of **bcp_di**, whereas three trajectories formed **bcp_ret**. This is in accordance with the experimental results which shows a major double inversion of configuration during the formation of **bcp** product.[124] Interestingly, five trajectories remained as diradical during the integration time of 3 ps. It should be noted that these trajectories if integrated further will lead to the formation of **bcp** with either retention or double inversion of configurations.

(iii) Ring-puckering and Formation of Different Isomers

The five-membered ring formed during the denitrogenation of **dbh** can undergo ring puckering, hence forming different envelope and twisted isomers. To follow the different isomers formed, the trajectories were plotted on the pseudorotation cycle.

Sample trajectories showing formation of different twisted and envelope isomers due to the ring-puckering motion of the five-membered cyclic ring are shown in Figure 5.16(c). The blue color coding in the plots represent the formation of a diradical. It should be noted that the trajectories start from $\mathbf{^3E}$ isomer. This is because, in the reactant the five-membered ring of **dbh** forms an envelope isomer with the third carbon atom being above the plane containing the other four carbon atoms. In addition, depending upon whether $\mathbf{^3E}$ or $\mathbf{E_3}$ isomer is formed during the formation of products, the products can be classified as **bcp** with retention of configuration or **bcp** with double inversion of configuration respectively. Hence, **TrajA** in Figure 5.16(c) represents the formation of the product **bcp_ret**. We can see that different envelope and twisted isomers are formed due to the ring-puckering motion before formation of the product **bcp_ret**. Similar ring-puckering leading to the formation of different envelope and twisted isomers of the five-membered cyclic ring is observed for **TrajB**, which then forms **bcp_di**. It is interesting to note that **TrajC** starts from the reactant isomer, forms a diradical hence leading to ring-puckering motions, and then forms the product $\mathbf{E_3}$. A C-C bond breaking of the bridged carbon atoms, again leads to the formation of the diradical **cpdr**, which then closes to form **bcp_ret** ($\mathbf{^3E}$ isomer).

B. Trajectories Initiated from ts1 Region

To understand the post-transition state dynamics, a set of 50 trajectories were initiated from **ts1** and integrated in the forward and reverse directions for 600 fs each with a E_{excess} of 91.28 kcal mol^{-1}. The initial geometries sampled for these trajectories are given in Figure 5.19. 34/50 trajectories gave complete trajectories i.e. **dbh** → **ts1** → **cpdr/bcp**. 15/50 trajectories formed **bcp** and 1 trajectory formed **dbh** on integrating in the forward and reverse directions. 27/33 reactive trajectories lead to the formation of product, **bcp**, whereas 7/33 trajectories formed **cpdr** during the integration time. It should be noted that these 7 trajectories will form **bcp** on integration for a longer period of time. Interestingly, 2/34 trajectories lead to the formation of **bcp_di** and then isomerized to **bcp_ret**. The stereochemistry of the product **bcp** formed is

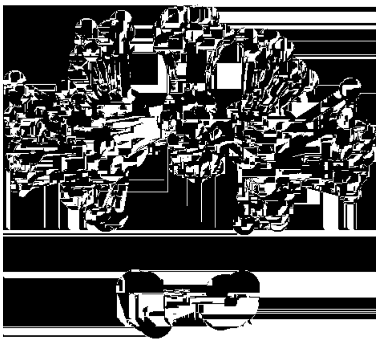

Figure 5.19: Initial geometries of 50 trajectories initiated from the **ts1** region.

given in Table 5.6. As observed in the trajectories initiated in the **dbh** region, here too major double inversion is seen in the products formed.

Table 5.6: Statistics of the products (with stereochemistry) and diradicals obtained during the integration time for trajectories initiated from **ts1**

	Number of trajectories
bcp_ret	2
bcp_di	25
cpdr	7
Total	34

C. Trajectories Initiated from ts1a Region

A set of 50 trajectories were also initiated from **ts1a** and integrated in the forward and reverse directions for 600 fs each with a E_{excess} of 90.18 kcal mol^{-1}. The initial geometries sampled for these trajectories sampled at **ts1a** are given in Figure 5.20. 3/50 trajectories formed **bcp** i.e. **dbh** $\rightarrow$ **ts1a** $\rightarrow$ **bcp**, whereas 47 trajectories lead to the formation of **bcp** on integrating in both forward and reverse directions. Interestingly, all the three reactive trajectories show a double inversion of configuration during the formation of product i.e. **bcp_di**, consistent with a major double inversion seen during the formation of products for trajectories initiated from the **dbh** region.

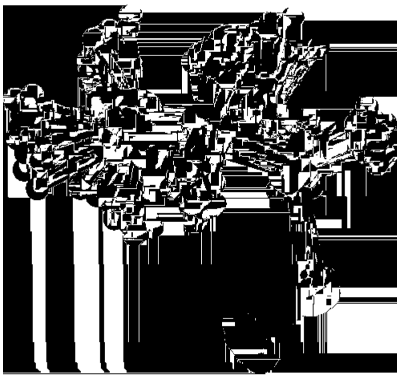

Figure 5.20: Initial geometries of 50 trajectories initiated from the **ts1a** region.

5.4 Summary and Conclusions

The different mechanistic pathways for the formation of products obtained during the thermal deazetization of **dbh** were mapped at the CASSCF(4,4)/6-31+G* and CASSCF(12,12)/6-31+G* and CASPT2 level of theories. The simultaneous breaking of the two C-N bonds in **dbh** corresponds to the synchronous denitrogenation pathway. On the other hand, the asynchronous mechanism involves the cleavage of one of the C-N bonds first followed by the other. Dissociation of the first C-N bond in **dbh** leads to the formation of a **dadr** which is followed by the second C-N bond cleavage to form **cpdr**. The low barrier torsional motion ($\sim$ 1-1.5 kcal mol^{-1}) about the C-N bonds in **dadr** leads to the formation of different isomers of **dadr**. The diradicals **cpdr** and **dadr** formed during the denitrogenation pathways can undergo pseudorotation to form different envelope and twisted conformers. The **dadr** having N_2 group in the equatorial position are expected to give exclusive double inverted product. It was found that DFT methods and UMP2 tend to overestimate the barrier for the reaction as compared to the CASSCF method and were not able to explain the reaction mechanism via synchronous and asynchronous pathways as observed in the CASSCF level. The different pathways for the formation of **cpn** were also mapped. To understand different reaction mechanisms, *ab initio* classical dynamics simulation was performed at the CASSCF(4,4)/6-31+G*. Trajectories were initiated from **dbh**, **ts1**, and **ts1a** using a microcanonical normal mode sampling technique. The trajectory simulations show that the reaction proceeds via both the synchronous and asynchronous denitrogenation pathways. The formation of a five-membered **cpdr** ring during the denitrogenation yields different envelope and twisted isomers before forming the products. Moreover, a major double inversion of configuration was observed consistent with the experiments.

BIBLIOGRAPHY

1. Szabo, A.; Ostlund, N. S. *Modern quantum chemistry: Introduction to advanced electronic structure theory*; Dover Books on Chemistry; Dover Publications, 1996.
2. Levine, I. N. *Quantum chemistry*; Pearson advanced chemistry series; Pearson, 2014.
3. Jensen, F. *Introduction to computational chemistry*; Wiley, 2007.
4. Hohenberg, P.; Kohn, W. Inhomogeneous electron gas. *Phys. Rev.* **1964**, *136*, B864–B871.
5. Kohn, W.; Sham, L. J. Self-consistent equations including exchange and correlation effects. *Phys. Rev.* **1965**, *140*, A1133.
6. Sun, L.; Hase, W. L. *Reviews in computational chemistry*; John Wiley and Sons, Ltd, 2003; Chapter 3, pp 79–146.
7. Mikosch, J.; Trippel, S.; Eichhorn, C.; Otto, R.; Lourderaj, U.; Zhang, J. X.; Hase, W. L.; Weidemüller, M.; Wester, R. Imaging nucleophilic substitution dynamics. *Science* **2008**, *319*, 183–186.
8. Sun, L.; Song, K.; Hase, W. L. A S_N2 reaction that avoids its deep potential energy minimum. *Science* **2002**, *296*, 875–878.
9. Hase, W.; Song, K.; Gordon, M. Direct dynamics simulations. *Comput. Sci. Eng.* **2003**, *5*, 36–44.
10. Xie, J.; Otto, R.; Mikosch, J.; Zhang, J.; Wester, R.; Hase, W. L. Identification of atomic-level mechanisms for gas-phase $X^- + CH_3Y$ S_N2 reactions by combined experiments and simulations. *Acc. Chem. Res.* **2014**, *47*, 2960–2969.
11. Lourderaj, U.; Park, K.; Hase, W. L. Classical trajectory simulations of post-transition state dynamics. *Int. Rev. Phys. Chem.* **2008**, *27*, 361–403.

12. Chen, W.; Hase, W. L.; Schlegel, H. B. *Ab initio* classical trajectory study of $H_2CO \rightarrow H_2 + CO$ dissociation. *Chem. Phys. Lett.* **1994**, *228*, 436–442.

13. Lourderaj, U.; Hase, W. L. Theoretical and computational studies of non-RRKM unimolecular dynamics. *J. Phys. Chem. A* **2009**, *113*, 2236–2253.

14. Schleyer, P. *Encyclopedia of computational chemistry*; Wiley, 1998.

15. Steinfeld, J.; Francisco, J.; Hase, W.; Hase, W. *Chemical Kinetics and Dynamics*; Prentice Hall, 1999.

16. Wigner, E. The transition state method. *Trans. Faraday Soc.* **1938**, *34*, 29–41.

17. van't Hoff, J. H. On the structure formulas in three-dimensional space. *Arch. Neerl. Sci. Exactes Nat.* **1874**, *445–454*.

18. Le Bel, J. A. On the relations which exist between the atomic formulas of organic compounds and the rotatory power of their solutions. *Bull. Soc. Chim.* **1874**, *22*, 337–347.

19. Hoffmann, R.; Alder, R. W.; Wilcox Jr, C. F. Planar tetracoordinate carbon. *J. Am. Chem. Soc.* **1970**, *92*, 4992–4993.

20. Keese, R. Carbon flatland: Planar tetracoordinate carbon and fenestranes. *Chem. Rev.* **2006**, *106*, 4787–4808.

21. Röttger, D.; Erker, G. Compounds containing planar-tetracoordinate carbon. *Angew. Chem. Int. Ed.* **1997**, *36*, 812–827.

22. Siebert, W.; Gunale, A. Compounds containing a planar-tetracoordinate carbon atom as analogues of planar methane. *Chem. Soc. Rev* **1999**, *28*, 367–371.

23. Yang, L.-M.; Ganz, E.; Chen, Z.; Wang, Z.-X.; Schleyer, P. v. R. Four decades of the chemistry of planar hypercoordinate compounds. *Angew. Chem. Int. Ed.* **2015**, *54*, 9468–9501.

24. Pancharatna, P. D.; Méndez-Rojas, M. A.; Merino, G.; Vela, A.; Hoffmann, R. Planar tetracoordinate carbon in extended systems. *J. Am. Chem. Soc.* **2004**, *126*, 15309–15315.

25. Merino, G.; Mendez-Rojas, M. A.; Vela, A.; Heine, T. Recent advances in planar tetracoordinate carbon chemistry. *J. Comput. Chem.* **2007**, *28*, 362–372.

26. Zheng, H.-f.; Xu, J.; Ding, Y.-h. A sixteen-valence-electron carbon-group 13 family with global penta-atomic planar tetracoordinate carbon: An ionic strategy. *Phys. Chem. Chem. Phys.* **2020**, *22*, 3975–3982.

27. Thirumoorthy, K.; Thimmakondu, V. S. Flat crown ethers with planar tetracoordinate carbon atoms. *Int. J. Quantum Chem.* **2021**, *121*, e26479.

28. Wang, Z.-X.; Schleyer, P. v. R. A new strategy to achieve perfectly planar carbon tetracoordination. *J. Am. Chem. Soc.* **2001**, *123*, 994–995.

29. Thirumoorthy, K.; Chandrasekaran, V.; Cooksy, A. L.; Thimmakondu, V. S. Kinetic stability of $Si_2C_5H_2$ isomer with a planar tetracoordinate carbon atom. *Chemistry* **2021**, *3*, 13–27.

30. von Ragué Schleyer, P.; Boldyrev, A. I. A new, general strategy for achieving planar tetracoordinate geometries for carbon and other second row periodic elements. *J. Chem. Soc., Chem. Commun.* **1991**, 1536–1538.

31. Li, Y.; Liao, Y.; Chen, Z. Be_2C monolayer with quasi-planar hexacoordinate carbons: A global minimum structure. *Angew. Chem. Int. Ed.* **2014**, *53*, 7248–7252.

32. Yañez, O.; Vásquez-Espinal, A.; Báez-Grez, R.; Rabanal-León, W. A.; Osorio, E.; Ruiz, L.; Tiznado, W. Carbon rings decorated with group 14 elements: New aromatic clusters containing planar tetracoordinate carbon. *New J. Chem.* **2019**, *43*, 6781–6785.

33. Collins, J. B.; Dill, J. D.; Jemmis, E. D.; Apeloig, Y.; Schleyer, P. v. R.; Seeger, R.; Pople, J. A. Stabilization of planar tetracoordinate carbon. *J. Am. Chem. Soc.* **1976**, *98*, 5419–5427.

34. Cotton, F. A.; Millar, M. The probable existence of a triple bond between two vanadium atoms. *J. Am. Chem. Soc.* **1977**, *99*, 7886–7891.

35. Erker, G. Planar-tetracoordinate carbon: Making stable Anti-van't Hoff/LeBel compounds. *Comment Inorg. Chem.* **1992**, *13*, 111–131.

36. Xu, J.; Zhang, X.; Yu, S.; Ding, Y.-h.; Bowen, K. H. Identifying the hydrogenated planar tetracoordinate carbon: A combined experimental and theoretical study of CAl_4H and CAl_4H^-. *J. Phys. Chem. Lett.* **2017**, *8*, 2263–2267.

37. Ebner, F.; Greb, L. Calix[4]pyrrole hydridosilicate: The elusive planar tetracoordinate silicon imparts striking stability to its anionic silicon hydride. *J. Am. Chem. Soc.* **2018**, *140*, 17409–17412.

38. Li, X.; Zhang, H.-F.; Wang, L.-S.; Geske, G.; Boldyrev, A. Pentaatomic tetracoordinate planar carbon, $[CAl_4]^{2-}$: A new structural unit and its salt complexes. *Angew. Chem. Int. Ed.* **2000**, *39*, 3630–3632.

39. Li, X.; Wang, L.-S.; Boldyrev, A. I.; Simons, J. Tetracoordinated planar carbon in the Al_4C^- anion. A combined photoelectron spectroscopy and *ab initio* study. *J. Am. Chem. Soc.* **1999**, *121*, 6033–6038.

40. Ghana, P.; Rump, J.; Schnakenburg, G.; Arz, M. I.; Filippou, A. C. Planar tetracoordinated silicon (ptSi): Room-temperature stable compounds containing anti-van't Hoff/Le Bel silicon. *J. Am. Chem. Soc.* **2020**, *143*, 420–432.

41. Driess, M.; Aust, J.; Merz, K.; van Wüllen, C. van't Hoff-Le Bel stranger: Formation of a phosphonium cation with a planar tetracoordinate phosphorus atom. *Angew. Chem. Int. Ed.* **1999**, *38*, 3677–3680.

42. Li, S.-D.; Ren, G.-M.; Miao, C.-Q.; Jin, Z.-H. M_4H_4X: hydrometals (M = Cu, Ni) containing tetracoordinate planar nonmetals (X = B, C, N, O). *Angew. Chem. Int. Ed.* **2004**, *43*, 1371–1373.

43. Li, Y.; Li, F.; Zhou, Z.; Chen, Z. SiC_2 silagraphene and its one-dimensional derivatives: Where planar tetracoordinate silicon happens. *J. Am. Chem. Soc.* **2011**, *133*, 900–908.

44. Sui, J.-j.; Xu, J.; Ding, Y.-h. A template for a planar tetracoordinate heavier group 14 atom: A global study of $C_2Si_2X^q$ (X = C, Si, Ge, Sn, Pb; q = +1, 0, -1). *Dalton Trans.* **2016**, *45*, 56–60.

45. Xu, J.; Ding, Y.-h. Pentaatomic planar tetracoordinate silicon with 14 valence electrons: A large-scale global search of $SiX_nY_m^q$ (n+m = 4; q = 0, ±1, -2; X, Y = main group elements from H to Br). *J. Comput. Chem.* **2015**, *36*, 355–360.

46. Job, N.; Khatun, M.; Thirumoorthy, K.; C H, S. S. R.; Chandrasekaran, V.; Anoop, A.; Thimmakondu, V. S. $CAl_4Mg^{0/-}$: Global minima with a planar tetracoordinate carbon atom. *Atoms* **2021**, *9*, 24.

47. Boldyrev, A. I.; Simons, J. Tetracoordinated planar carbon in pentaatomic molecules. *J. Am. Chem. Soc.* **1998**, *120*, 7967–7972.

48. Suresh, C. H.; Frenking, G. Direct 1-3 metal-carbon bonding and planar tetracoordinated carbon in group 6 metallacyclobutadienes. *Organometallics* **2010**, *29*, 4766–4769.

49. Thirumoorthy, K.; Karton, A.; Thimmakondu, V. S. From high-energy C_7H_2 isomers with a planar tetracoordinate carbon atom to an experimentally known carbene. *J. Phys. Chem. A* **2018**, *122*, 9054–9064.

50. Sateesh, B.; Srinivas Reddy, A.; Narahari Sastry, G. Towards design of the smallest planar tetracoordinate carbon and boron systems. *J. Comput. Chem.* **2007**, *28*, 335–343.

51. Priyakumar, U. D.; Sastry, G. N. A system with three contiguous planar tetracoordinate carbons is viable: A computational study on a $C_6H_6^{2+}$ isomer. *Tetrahedron Lett.* **2004**, *45*, 1515–1517.

52. Cui, Z.-h.; Contreras, M.; Ding, Y.-h.; Merino, G. Planar tetracoordinate carbon versus planar tetracoordinate boron: The case of CB_4 and its cation. *J. Am. Chem. Soc.* **2011**, *133*, 13228–13231.

53. Cui, Z.-h.; Ding, Y.-h.; Cabellos, J. L.; Osorio, E.; Islas, R.; Restrepo, A.; Merino, G. Planar tetracoordinate carbons with a double bond in CAl_3E clusters. *Phys. Chem. Chem. Phys.* **2015**, *17*, 8769–8775.

54. Nandula, A.; Trinh, Q. T.; Saeys, M.; Alexandrova, A. N. Origin of extraordinary stability of square-planar carbon atoms in surface carbides of cobalt and nickel. *Angew. Chem. Int. Ed.* **2015**, *54*, 5312–5316.

55. Guo, J.-C.; Feng, L.-Y.; Dong, C.; Zhai, H.-J. Ternary 12-electron $CBe_3X_3^+$(X = H, Li, Na, Cu, Ag) clusters: Planar tetracoordinate carbons and superalkali cations. *Phys. Chem. Chem. Phys.* **2019**, *21*, 22048–22056.

56. Guo, J.-C.; Feng, L.-Y.; Dong, C.; Zhai, H.-J. Planar pentacoordinate versus tetracoordinate carbons in ternary CBe_4Li_4 and $CBe_4Li_4^{2-}$ clusters. *J. Phys. Chem. A* **2018**, *122*, 8370–8376.

57. Priyakumar, U. D.; Reddy, A. S.; Sastry, G. N. The design of molecules containing planar tetracoordinate carbon. *Tetrahedron Lett.* **2004**, *45*, 2495–2498.

58. Xie, H.-b.; Ding, Y.-h. CAl_4X (X = Si, Ge): Molecules with simultaneous planar tetracoordinate carbon, aluminum, and silicon/germanium. *J. Chem. Phys.* **2007**, *126*, 184302.

59. Karton, A.; Thimmakondu, V. S. From molecules with a planar tetracoordinate carbon to an astronomically known C_5H_2 carbene. *J. Phys. Chem. A* . **2022**, *126*, 2561–2568.

60. Tipker, R. M.; Muldoon, J. A.; Pham, D. H.; Varga, B. R.; Hughes, R. P.; Glueck, D. S.; Balaich, G. J.; Rheingold, A. L. Configurational lability at tetrahedral phosphorus: Syn/anti-isomerization of a P-stereogenic phosphiranium cation by intramolecular epimerization at phosphorus. *Angew. Chem. Int. Ed.* **2022**, *61*, e202110753.

61. Khatun, M.; Roy, S.; Giri, S.; CH, S. S. R.; Anoop, A.; Thimmakondu, V. S. $BAl_4Mg^{-/0/+}$: Global minima with a planar tetracoordinate or hypercoordinate boron atom. *Atoms* **2021**, *9*.

62. Sigmund, L. M.; Ehlert, C.; Grynova, G.; Greb, L. Stereoinversion of tetrahedral p-block element hydrides. *J. Chem. Phys.* **2022**, *156*, 194113.

63. Guo, J.-C.; Miao, C.-Q.; Ren, G.-M. Planar tetracoordinate Si and Ge in π-aromatic $X_3Cu_3^+$ (X= Si, Ge) cations. *Comput. Theor. Chem.* **2014**, *1032*, 7–11.

64. Guo, J.-C.; Wu, H.-X.; Ren, G.-M.; Miao, C.-Q.; Li, Y.-X. D_{3h} $X_3Li_3^+$ (X= C, Si and Ge): Superalkali cations containing three planar tetracoordinate X atoms. *Comput. Theor. Chem.* **2016**, *1083*, 1–6.

65. Lammertsma, K.; Schleyer, P. v. R. Structures and energies of isomeric carbodications ($C_5H_4^{2+}$ and $C_6H_4^{2+}$). *J. Phys. Chem.* **1988**, *92*, 881–886.

66. Frisch, M. J.; Head-Gordon, M.; Pople, J. A. A direct MP2 gradient method. *Chem. Phys. Lett.* **1990**, *166*, 275–280.

67. Kendall, R. A.; Dunning Jr, T. H.; Harrison, R. J. Electron affinities of the first-row atoms revisited. Systematic basis sets and wave functions. *J. Chem. Phys.* **1992**, *96*, 6796–6806.

68. Fukui, K. The path of chemical reactions-the IRC approach. *Acc. Chem. Res.* **1981**, *14*, 363–368.

69. Schleyer, P. v. R.; Maerker, C.; Dransfeld, A.; Jiao, H.; van Eikema Hommes, N. J. Nucleus-independent chemical shifts: A simple and efficient aromaticity probe. *J. Am. Chem. Soc.* **1996**, *118*, 6317–6318.

70. Frisch, M. J. et al. Gaussian16 Revision C.01. 2016; Gaussian Inc. Wallingford CT.

71. Monkhorst, H. J. Activation energy for interconversion of enantiomers containing an asymmetric carbon atom without breaking bonds. *Chem. Commun. (London)* **1968**, 1111–1112.

72. Rabrenović, M.; Brenton, A.; Beynon, J. Metastable doubly-charged ions of methane studied by means of a triple-sector mass spectrometer. *Int. J. Mass. Spectrom.* **1983**, *52*, 175–182.

73. McGrath, M. P.; Radom, L. Alkaplanes: A class of neutral hydrocarbons containing a potentially planar tetracoordinate carbon. *J. Am. Chem. Soc.* **1993**, *115*, 3320–3321.

74. Rasmussen, D. R.; Radom, L. Planar-tetracoordinate carbon in a neutral saturated hydrocarbon: Theoretical design and characterization. *Angew. Chem. Int. Ed.* **1999**, *38*, 2875–2878.

75. Zhang, C.; Sun, W.; Cao, Z. Zigzag boron-carbon nanotubes with quasi-planar tetracoordinate carbons. *J. Am. Chem. Soc.* **2008**, *130*, 5638–5639.

76. Yañez, O.; Vásquez-Espinal, A.; Pino-Rios, R.; Ferraro, F.; Pan, S.; Osorio, E.; Merino, G.; Tiznado, W. Exploiting electronic strategies to stabilize a planar tetracoordinate carbon in cyclic aromatic hydrocarbons. *Chem. Comm.* **2017**, *53*, 12112–12115.

77. Thimmakondu, V. S.; Thirumoorthy, K. $Si_3C_2H_2$ isomers with a planar tetracoordinate carbon or silicon atom(s). *Comput. Theor. Chem.* **2019**, *1157*, 40–46.

78. Cahn, R. S.; Ingold, C.; Prelog, V. Specification of molecular chirality. *Angew. Chem. Int. Ed.* **1966**, *5*, 385–415.

79. Smith, M.; March, J. *March's advanced organic chemistry: Reactions, mechanisms, and structure*; Wiley, 2007.

80. Wynberg, H.; Hekkert, G.; Houbiers, J.; Bosch, H. The optical activity of butylethylhexylpropylmethane1. *J. Am. Chem. Soc.* **1965**, *87*, 2635–2639.

81. Chandrasekhar, V. A rebel in the ranks: A phosphonium cation with a planar tetracoordinate phosphorus atom-An anti van't Hoff-Le Bel structure. *Resonance* **2001**, *6*, 84–90.

82. Wang, L.-S.; Boldyrev, A. I.; Li, X.; Simons, J. Experimental observation of pentaatomic tetracoordinate planar carbon-containing molecules. *J. Am. Chem. Soc.* **2000**, *122*, 7681–7687.

83. Boldyrev, A. I.; Wang, L.-S. Beyond classical stoichiometry: Experiment and theory. *J. Phys. Chem. A* **2001**, *105*, 10759–10775.

84. Jemmis, E. D.; Parameswaran, P. Structure and bonding in cyclic isomers of $BAl_2H_n^m$ (n = 3-6, m = -2 to +1): Preference for planar tetracoordination, pyramidal tricoordination, and divalency. *Chem. Eur. J.* **2007**, *13*, 2622–2631.

85. Li, Y.; Li, F.; Zhou, Z.; Chen, Z. SiC_2 silagraphene and its one-dimensional derivatives: Where planar tetracoordinate silicon happens. *J. Am. Chem. Soc.* **2011**, *133*, 900–908.

86. Zhang, Y.; Zhang, C.; Mo, Y.; Cao, Z. Planar tetracoordinate silicon in organic molecules as carbenoid-type amphoteric centers: A computational study. *Chem. Eur. J.* **2021**, *27*, 1402–1409.

87. Cremer, D. *Encyclopedia of computational chemistry*; John Wiley & Sons, Ltd, 2002.

88. Valiev, M.; Bylaska, E. J.; Govind, N.; Kowalski, K.; Straatsma, T. P.; Van Dam, H. J.; Wang, D.; Nieplocha, J.; Apra, E.; Windus, T. L., et al. NWChem: A comprehensive and scalable open-source solution for large scale molecular simulations. *Comput. Phys. Commun.* **2010**, *181*, 1477–1489.

89. Werner, H.-J.; Knowles, P. J.; Knizia, G.; Manby, F. R.; Schütz, M., et al. MOLPRO, version 2012.1, A package of *ab initio* programs. 2012; see http://www.molpro.net.

90. Stanton, J. F. Why CCSD(T) works: A different perspective. *Chem. Phys. Lett.* **1997**, *281*, 130–134.

91. Lourderaj, U.; Sun, R.; Kohale, S. C.; Barnes, G. L.; de Jong, W. A.; Windus, T. L.; Hase, W. L. The VENUS/NWChem software package. Tight coupling between chemical dynamics simulations and electronic structure theory. *Comput. Phys. Commun.* **2014**, *185*, 1074–1080.

92. Valiev, M.; Bylaska, E. J.; Govind, N.; Kowalski, K.; Straatsma, T. P.; Van Dam, H. J.; Wang, D.; Nieplocha, J.; Apra, E.; Windus, T. L., et al. NWChem: A comprehensive and scalable open-source solution for large scale molecular simulations. *Comput. Phys. Commun.* **2010**, *181*, 1477–1489.

93. Swope, W. C.; Andersen, H. C.; Berens, P. H.; Wilson, K. R. A computer simulation method for the calculation of equilibrium constants for the formation of physical clusters of molecules: Application to small water clusters. *J. Chem. Phys.* **1982**, *76*, 637–649.

94. Inadomi, Y.; Morihashi, K.; Kikuchi, O. Theoretical study of the thermal interconversion mechanism between the norbornadiene and quadricyclane radical cations. *J. Mol. Struct.: THEOCHEM* **1998**, *434*, 59–66.

95. Chen, J. S.; Houk, K.; Foote, C. S. Theoretical study of the concerted and stepwise mechanisms of triazolinedione Diels-Alder reactions. *J. Am. Chem. Soc.* **1998**, *120*, 12303–12309.

96. Huang, Y.; Ma, S. Mechanism of the inner hydrogen atom transfer in free base porphyrazine: A direct *ab initio* dynamics study. *J. Mol. Struct.: THEOCHEM* **2004**, *684*, 217–222.

97. Dmitrenko, O.; Bach, R. D. Reassessment of the level of theory required for the epoxidation of ethylene with dioxiranes. *J. Phys. Chem. A* **2004**, *108*, 6886–6892.

98. de Visser, S. P.; Ogliaro, F.; Shaik, S. Stereospecific oxidation by compound I of cytochrome P450 does not proceed in a concerted synchronous manner. *Chem. Commun.* **2001**, 2322–2323.

99. Pradhan, R.; Harshan, A. K.; Krishnavilasam Chandrika, G. S.; Srinivasan, A.; Lourderaj, U. Time-dependent density functional theoretical investigation of photoinduced excited-state intramolecular dual proton transfer in diformyl dipyrromethanes. *J. Phys. Chem. A* **2016**, *120*, 9894–9906.

100. Heidrich, D.; Quapp, W. Saddle points of index 2 on potential energy surfaces and their role in theoretical reactivity investigations. *Theor. Chim. Acta* **1986**, *70*, 89–98.

101. Ezra, G. S.; Wiggins, S. Phase-space geometry and reaction dynamics near index 2 saddles. *J. Phys. A: Math. Theor.* **2009**, *42*, 205101.

102. Collins, P.; Ezra, G. S.; Wiggins, S. Index k saddles and dividing surfaces in phase space with applications to isomerization dynamics. *J. Chem. Phys.* **2011**, *134*, 244105.

103. Mauguière, F. A.; Collins, P.; Ezra, G.; Wiggins, S. Bond breaking in a Morse chain under tension: Fragmentation patterns, higher index saddles, and bond healing. *J. Chem. Phys.* **2013**, *138*, 134118.

104. Minyaev, R.; Getmanskii, I.; Quapp, W. A second-order saddle point in the reaction coordinate for the isomerization of the NH_5 complex: *Ab initio* calculations. *Russ. J. Phys. Chem.* **2004**, *78*, 1494–1498.

105. Getmanskii, I.; Minyaev, R. Study of the structural and thermodynamic stability of pentacoordinated nitrogen compounds NF_2X_3 (X= H, Cl, Br): *Ab initio* calculations. *J. Struct. Chem.* **2008**, *49*, 973–978.

106. Quapp, W.; Maria Bofill, J. Embedding of the saddle point of index two on the PES of the ring opening of cyclobutene. *Int. J. Quantum Chem.* **2015**, *115*, 1635–1649.

107. Breulet, J.; Schaefer III, H. F. Conrotatory and disrotatory stationary points for the electrocyclic isomerization of cyclobutene to cis-butadiene. *J. Am. Chem. Soc.* **1984**, *106*, 1221–1226.

108. Harabuchi, Y.; Ono, Y.; Maeda, S.; Taketsugu, T.; Keipert, K.; Gordon, M. S. Nontotally symmetric trifurcation of an S_N2 reaction pathway. *J. Comput. Chem.* **2016**, *37*, 487–493.

109. Rashmi, R.; Yadav, K.; Lourderaj, U.; Paranjothy, M. Second-order saddle dynamics in isomerization reaction. *Regul. Chaotic Dyn.* **2021**, *26*, 119–130.

110. Smedarchina, Z.; Siebrand, W.; Fernández-Ramos, A.; Meana-Paneda, R. Mechanisms of double proton transfer. Theory and applications. *Zeitschrift für Physikalische Chemie* **2008**, *222*, 1291–1309.

111. Pandey, P.; Naik, S.; Keshavamurthy, S. Classical and quantum dynamical manifestations of index-2 saddles: Concerted versus sequential reaction mechanisms. *Regul. Chaotic Dyn.* **2021**, *26*, 165–182.

112. Pradhan, R.; Lourderaj, U. Quantum chemical investigation of the thermal denitrogenation of 1-pyrazoline. *Phys. Chem. Chem. Phys.* **2017**, *19*, 27468–27477.

113. Pradhan, R.; Lourderaj, U. Can reactions follow non-traditional second-order saddle pathways avoiding transition states? *Phys. Chem. Chem. Phys.* **2019**, *21*, 12837–12842.

114. Crawford, R. J.; Mishra, A. The Mechanism of the thermal decomposition of 1-pyrazolines and its relationship to cyclopropane isomerizations. *J. Am. Chem. Soc.* **1966**, *88*, 3963–3969.

115. Clarke, T. C.; Wendling, L. A.; Bergman, R. G. Complete determination of the stereochemistry of a 3,5-dialkylpyrazoline thermal decomposition. Synthesis, absolute configuration, and pyrolysis of (+)-(3*R*,5*R*)- and (+)-(3*R*,5*S*)-3-ethyl-5-methyl-1-pyrazolines. *J. Am. Chem. Soc.* **1977**, *99*, 2740–2750.

116. Crawford, R. J.; Dummel, R.; Mishra, A. Kinetic evidence for 1,3-diradicals from the thermal decomposition of 1-pyrazolines. *J. Am. Chem. Soc.* **1965**, *87*, 3023–3025.

117. Reyes, M. B.; Carpenter, B. K. Mechanism of thermal deazetization of 2,3-diazabicyclo[2.2.1]hept-2-ene and its reaction dynamics in supercritical fluids. *J. Am. Chem. Soc.* **2000**, *122*, 10163–10176.

118. Engel, P. S.; Melaugh, R. A.; Månsson, M.; Timberlake, J. W.; Garner, A. W.; Rossini, F. D. Thermochemistry of nine diazenes (azo compounds). *J. Chem. Thermodyn.* **1976**, *8*, 607–621.

119. Khuong, K. S.; Houk, K. N. One-bond, two-bond, and three-bond mechanisms in thermal deazetizations of 2,3-diazabicyclo[2.2.2]oct-2-enes, trans-azomethane, and 2,3-diazabicyclo[2.2.1]hept-2-ene. *J. Am. Chem. Soc.* **2003**, *125*, 14867–14883.

120. Simpson, C. J. S. M.; Wilson, G. J.; Adam, W. Dynamics of the thermal decomposition of 2,3-diazabicyclo[2.2.1]hept-2-ene. *J. Am. Chem. Soc.* **1991**, *113*, 4728–4732.

121. Abe, M.; Ishihara, C.; Kawanami, S.; Masuyama, A. Novel substituent effects on the mechanism of the thermal denitrogenation of 2,3-diazabicyclo[2.2.1]hept-2-ene derivatives, stepwise versus concerted. *J. Am. Chem. Soc.* **2005**, *127*, 10–11.

122. Safont, V. S.; González-Navarrete, P.; Oliva, M.; Andrés, J. Inquiry of the electron density transfers in chemical reactions: A complete reaction path for the denitrogenation process of 2,3-diazabicyclo[2.2.1]hept-2-ene derivatives. *Phys. Chem. Chem. Phys.* **2015**, *17*, 32358–32374.

123. Cohen, S. G.; Zand, R.; Steel, C. Preparation and kinetics of decomposition of a bicyclic azo compound. A novel reduction1. *J. Am. Chem. Soc.* **1961**, *83*, 2895–2900.

124. Lyons, B. A.; Pfeifer, J.; Peterson, T. H.; Carpenter, B. K. Dynamic models for the thermal deazetization of 2,3-diazabicyclo[2.2.1]hept-2-ene. *J. Am. Chem. Soc.* **1993**, *115*, 2427–2437.

125. Yamamoto, N.; Olivucci, M.; Celani, P.; Bernardi, F.; Robb, M. A. An MC-SCF/MP2 study of the photochemistry of 2,3-diazabicyclo[2.2.1]hept-2-ene: Production and fate of diazenyl and hydrazonyl biradicals. *J. Am. Chem. Soc.* **1998**, *120*, 2391–2407.

126. Clark, W. D. K.; Steel, C. Photochemistry of 2,3-diazabicyclo[2.2.2]oct-2-ene. *J. Am. Chem. Soc.* **1971**, *93*, 6347–6355.

127. Adam, W.; Grüne, M.; Diedering, M.; Trofimov, A. V. Temperature and viscosity dependence in the stereoselective formation of the inverted housane for the photochemical nitrogen loss from the deuterium-stereolabeled parent diazabicyclo[2.2.1]hept-2-ene. *J. Am. Chem. Soc.* **2001**, *123*, 7109–7112.

128. Solomon, B. S.; Thomas, T.; Steel, C. Primary processes in the photochemistry of diazabicyclic compounds. *J. Am. Chem. Soc.* **1968**, *90*, 2249–2258.

129. Adam, W.; Martí, V.; Sahin, C.; Trofimov, A. V. Viscosity-controlled stereoselective inversion in the photochemical denitrogenation of a stereolabeled diazabicyclo[2.2.1]heptene (DBH)-type azoalkane. *J. Am. Chem. Soc.* **2000**, *122*, 5002–5003.

130. Adam, W.; Diedering, M.; Trofimov, A. V. Photochemical versus thermal skeletal inversion: Viscosity-controlled photodenitrogenation of a bridgehead-substituted DBH-type azoalkane and thermal syn-to-anti housane isomerization. *J. Am. Chem. Soc.* **2002**, *124*, 5427–5430.

131. Sinicropi, A.; Page, C. S.; Adam, W.; Olivucci, M. Computational study on the origin of the stereoselectivity for the photochemical denitrogenation of diazabicycloheptene. *J. Am. Chem. Soc.* **2003**, *125*, 10947–10959.

132. Roth, W. R.; Martin, M. Stereochemistry of the thermal and photochemical decomposition of 2,3-diazabicyclo[2.2.1]hept-2-ene. *Liebigs Ann. Chem.* **1967**, *702*, 1–5.

133. Roth, W. H.; Martin, M. Zur stereochemie der 1,2-cycloaddition an das bicyclo[2.1.0] system. *Tetrahedron Lett.* **1967**, *8*, 4695–4698.

134. Allred, E. L.; Smith, R. L. Thermolysis of exo- and endo-5-methoxy-2,3-diazabicyclo[2.2.1]-2-heptene. *J. Am. Chem. Soc.* **1967**, *89*, 7133–7134.

135. Bauer, S. H. Operational criteria for concerted bond breaking in gas-phase molecular elimination reactions. *J. Am. Chem. Soc.* **1969**, *91*, 3688–3689.

136. Kilpatrick, J. E.; Pitzer, K. S.; Spitzer, R. The thermodynamics and molecular structure of cyclopentane. *J. Am. Chem. Soc.* **1947**, *69*, 2483–2488.

137. Harris, D. O.; Engerholm, G. G.; Tolman, C. A.; Luntz, A. C.; Keller, R. A.; Kim, H.; Gwinn, W. Ring puckering in five-membered rings. I. General theory. *J. Chem. Phys.* **1969**, *50*, 2438–2445.

138. Pitzer, K. *Molecular structure and statistical thermodynamics: Selected papers of Kenneth S. Pitzer*; Series on 20th Century Chemistry Series; World Scientific, 1993.

139. Altona, C.; Sundaralingam, M. Conformational analysis of the sugar ring in nucleosides and nucleotides. New description using the concept of pseudorotation. *J. Am. Chem. Soc.* **1972**, *94*, 8205–8212.

140. Hehre, W.; Hehre, W.; Radom, L.; von R. Schleyer, P.; Pople, J. *Ab initio molecular orbital theory*; A Wiley-Interscience publication; Wiley, 1986.

141. Dunning Jr, T. H. Gaussian basis sets for use in correlated molecular calculations. I. The atoms boron through neon and hydrogen. *J. Chem. Phys.* **1989**, *90*, 1007–1023.

142. Kendall, R. A.; Dunning Jr, T. H.; Harrison, R. J. Electron affinities of the first-row atoms revisited. Systematic basis sets and wave functions. *J. Chem. Phys.* **1992**, *96*, 6796–6806.

143. Ren, P.; Wu, C.; Ponder, J. W. Polarizable atomic multipole-based molecular mechanics for organic molecules. *J. Chem. Theory Comput.* **2011**, *7*, 3143–3161.

144. Swope, W. C.; Andersen, H. C.; Berens, P. H.; Wilson, K. R. A computer simulation method for the calculation of equilibrium constants for the formation of physical clusters of molecules: Application to small water clusters. *J. Chem. Phys.* **1982**, *76*, 637–649.